Characterization of Glow Plug and HCCI Combustion Processes in a Small Volume at High Engine Speed - Load Range, Emission Characteristics and Optical Diagnostics

Manente, Vittorio

2007

Characterization of Glow Plug and HCCI Combustion Processes in a Small Volume at High Engine Speed

Load Range, Emission Characteristics and Optical Diagnostics

Vittorio Manente

Thesis for the Degree of Licentiate in Engineering

Division of Combustion Engines
Department of Energy Sciences
Faculty of Engineering, LTH
Lund University
P.O. Box 118
SE-221 00 Lund
Sweden

To Asnate

Acknowledgements

speaking with anybody and looking at the sky. When I saw her, my Italian mind thought: "c***o, che f**a! Lei sarà mia". Well, after three years, many ups and downs and on/off periods, we are still together… Baby, thanks for your constant presence during this time and for the wonderful moments we share and have shared!

P.S. Thanks mom, dad and Stefano for sponsoring my education and for handling a son/brother like me… It is tough, I can imagine…

Table of Contents

1. Abstract

The objective of this research that has taken me halfway to my PhD degree was to understand how HCCI combustion behaves in a small volume at high rotational speed. The investigation has been carried out using a modified model airplane engine. The whole study can be divided into two main parts; in the first, the nature of the glow plug combustion was investigated through experiments on a metal engine and by use of optical diagnostics. Once the glow plug combustion process was fully understood, the engine was modified in order to achieve pure HCCI operations. Initially, a basic investigation was carried out using a metal and optical engine. Later, further research was performed on the main parameters affecting HCCI operations in such a small volume, i.e. the quenching distance, wall temperature and combustion chamber geometry.

In addition to these studies, a model for calculating the amount of retained gas in a 2-stroke engine was developed and a miniature HCCI free piston engine was designed from scratch.

2. Introduction and background

Nowadays, power supply systems play fundamental roles in everyday life applications. For low power generation, electrochemical batteries are the most commonly used devices for storing and delivering energy when needed. The standard lithium-ion batteries have an energy density of 1 MJ/kg and this value seems to be asymptotic. A conventional hydrocarbon fuel has an energy density between 41 and 45 MJ/kg. Consequently, if an internal combustion engine, ICE, is used for producing electrical power with a minimum overall efficiency of 3%, this kind of device should be able to surpass any battery. In addition, an ICE can produce energy as long as fuel is available, they can be recharged (i.e. refilled) very quickly and they do not constitute a disposal problem when replaced since they do not contain dangerous or polluting components.
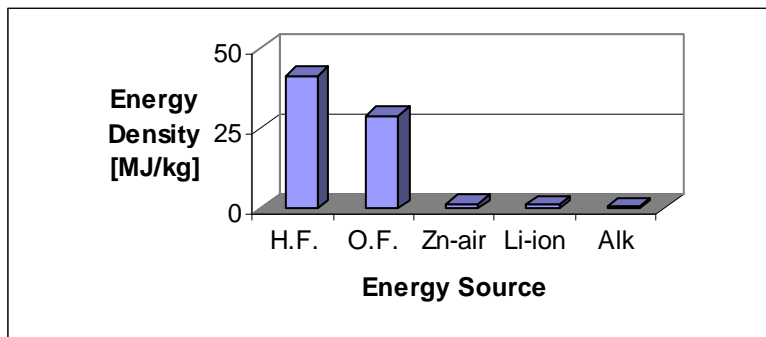
Figure 1: The energy density of the most commonly used electrochemical batteries and average lower heating values (energy density) of hydrocarbon and organic fuels. H.F. = hydrocarbon fuel, O.F. = organic fuel, Alk. = alkaline battery

Figure 2 shows an overview of energy sources for portable or autonomous miniature devices based on various physical principles.
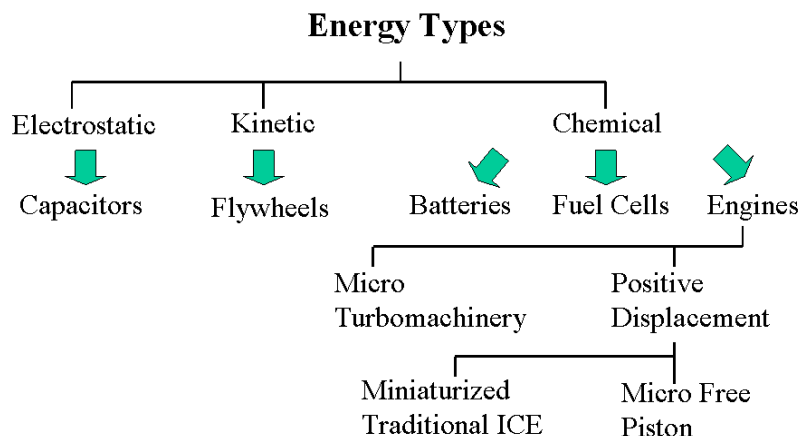
Figure 2: Energy sources for portable or autonomous miniature devices.

Table 1: The energy and power densities of portable or autonomous miniature devices.

Electrostatic	Capacitors			
		0.2	[J/cm^3]	Standard
		1000	[W/cm^3]	
		10	[J/cm^3]	Super
		15	[W/cm^3]	
Kinetic	Flywheels	1000	[J/cm^3]	
		3.3	[W/cm^3]	
Chemical	Batteries	2000	[J/cm^3]	
		0.15	[W/cm^3]	
	Fuel Cells	7000	[J/cm^3]	Hydrogen Reformed
		0.04	[W/cm^3]	
		3000	[J/cm^3]	Direct Methanol
		0.02	[W/cm^3]	
	Micro Turbo-machinery	under research		
	ICE	3000	[J/cm^3]	Miniaturized
		1.5	[W/cm^3]	
		2000	[J/cm^3]	Free Piston
		0.3	[W/cm^3]	

2.1 State of the art in alternative power generators

Nowadays, the largest research efforts for power generation have been made in two main areas: fuel cells and Power MEMS (Micro Electro Mechanical Systems). Nuclear energy is not reported since it is not considered worldwide to be a long-term candidate for power generation in small systems and only minor funding has been allocated for this activity by the Nuclear Engineering Education Research, NEER, at the Energy Department of the USA.

1- Fuel Cells currently represent one promising electric energy source. They convert chemical energy, provided by a proper fuel, into a usable electric energy. Worldwide, universities and industries are investigating this concept due to the following reasons:

- A high theoretical efficiency that can lead to a practical value of 60 % [1].

5

- Clean technology, e.g. no emissions of CO_2, CO, SO_x in the case of H_2 fuel cells, and only minor emissions of NO_x depending on the temperature of the process.

Micro fuel cells are considered a breakthrough for portable devices and are able to guarantee long operations as well as easy and fast recharge processes. The main drawbacks for micro scale fuel cells are related to the following issues [2]:

- The low power density implies the use of a hybrid system: a standard rechargeable chemical battery and a micro fuel cell as energy reservoir for recharging the battery.
- Significant technological problems for storing H_2 in the micro world and the need for increasing the energy density have led to investigations concerning the use of methanol in the fuel cells. Methanol gives rise to CO_2 as a combustion product.
- Direct methanol fuel cells are appealing from a technological point of view because of their relative simplicity, but have lower performances than reformed hydrogen fuel cells.
- Precious metals, such as platinum or palladium which are used as catalyst in both fuel cells and reformers, could increase in price if consumers suddenly demanded hundreds of millions of devices per year.

2- Microengines, several programs are underway in the field of Power MEMS, including both *microturbines* and *positive displacement micromachines*. The common goal is to replace the electrochemical batteries. The idea of developing microengines is supported by the high energy density of hydrocarbons and organic fuels, which display energy densities of respectively 44 and 29 MJ/kg. An engine generator would need a minimum overall fuel conversion efficiency of only 4 % to surpass any battery.

2 a - Microturbines have been developed in the US [3] [4] [5], Japan [6] and Europe [7]. The main problems concern the high rotational speed and the over-heating of bearings, and use of these systems are thus allowed only when blowing compressed air. Regarding the burners, complex combustors are under development in order to overcome the quenching problem in the micro domain. The preheating of the reactants [8] and the use of catalytic materials [9] have been investigated.

2 b- Positive Displacement Micromachines are a very promising approach as a result of the thermal energy not being converted into kinetic energy of the fluid. This is an advantage when the dimensions are scaled down to the millimeter scale since pressure losses, due to the drag forces with respect to inertial forces (low Reynolds numbers), are avoided. This is a typical problem with microturbines whose mechanical efficiency, excluding the thermal one, is lower than 15%. Furthermore in these systems, combustion is not critical thanks to the possibility of momentarily increasing the pressure and the temperature of the fluid by imposing a sudden compression. At the University of Minnesota, the feasibility of HCCI microcombustion was proved by Alchimar [10] [11] [12].

Alchimar proposed a mini free-piston engine, where the piston slid in a frame and the gas exchange was provided by ports as in a 2-stroke engine. Two requirements were involved: low friction and proper sealing. The only technological way to accomplish both issues was to fabricate the two coupling surfaces with extremely good finishing - a challenging task in the micro-domain.

2.2 The VIMPA project

The acronym VIMPA stands for: Vibrating Microengine for Power Generation and Microsystems Actuation. VIMPA is a cooperation between three universities: Scuola Superiore Sant'Anna (SSSA), Lund Institute of Technology, LTH, and Berlin Technical University, TUB. The original idea developed by SSSA was to obtain an elastic combustion chamber, 10 [mm] in diameter, whose vibrations were produced by a repeated autoignition of the fuel. The working principle is shown in Figure 3. The output energy is supposed to be collected either by an electric generator or a crank mechanism.
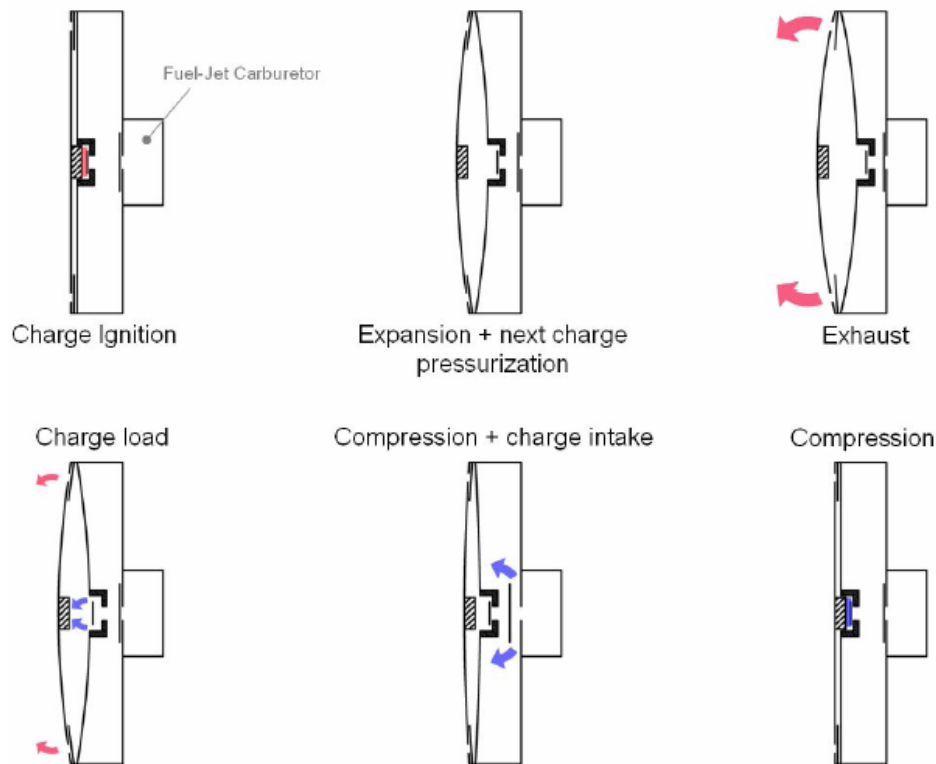
Figure 3: The VIMPA working principle.

The theoretical advantages of this concept are obvious. The high efficiency of HCCI combustion combined with a low friction structure (the only friction comes from the hysteretic behavior of the membranes under elastic deformations) would have led to excellent results. Unfortunately, the concept was proved to be

practically unviable and after two years of researches VIMPA seemed to be at a dead end path. The original idea was thus modified by LTH in order to obtain a viable device. The new VIMPA is basically a conventional free piston, scaled down according to the knowledge obtained on quenching and boundary layer phenomena (after a year and a half spent on understanding how HCCI combustion behaves in small volumes at high engine speed). The new VIMPA is shown in Figure 4, and its working principle will be explained in the paragraph entitled *VIMPA Design*.
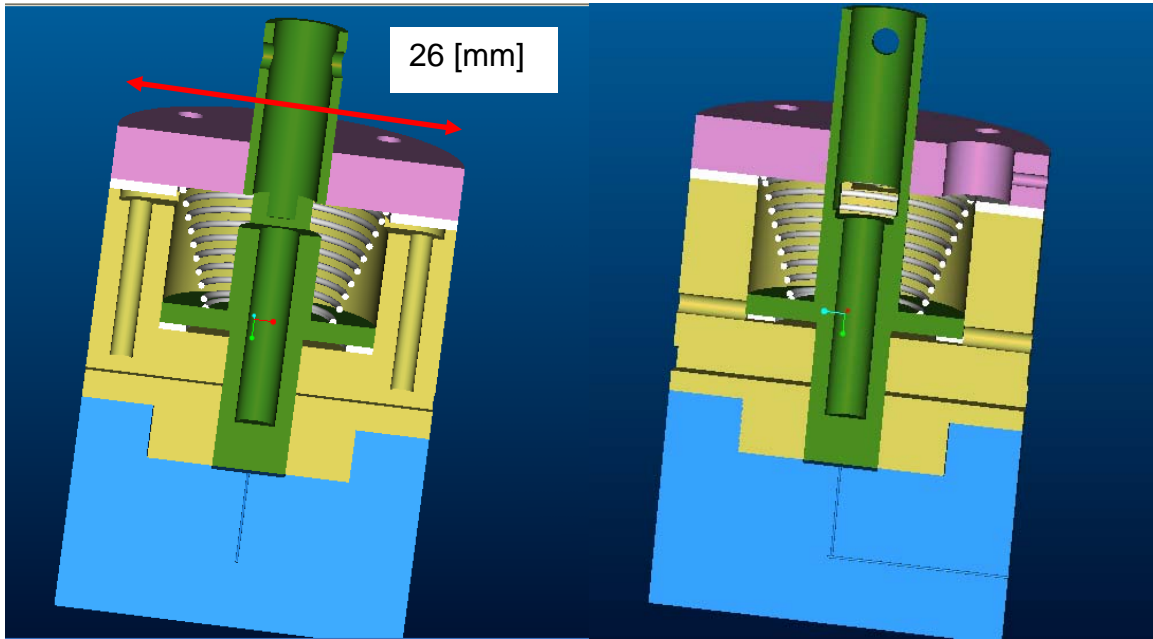
Figure 4: The second VIMPA design.

3. Internal combustion engine overview

This chapter contains a very short review of the main internal combustion engines used today. The objective is not to show what kind of engines cars or trucks are equipped with, but mainly to give an idea of how the ignition process takes place.

The two main internal combustion engines used today are the spark ignition engine, SI, and the compression ignition engine, CI. Each category can be divided into two sub-categories: 2- and 4- stroke. In a 2-stroke engine, compression, combustion/expansion, and scavenging processes are achieved in one revolution of the crankshaft while with a 4-stroke engine there is one stroke for each of the following four phases: compression, combustion/expansion, exhaust and intake. Two crankshaft revolutions are required for completing one thermodynamic cycle.

3.1 Spark Ignition Engine

In a Spark Ignition (SI) engine, fuel is supplied during the intake stroke resulting in a more or less homogeneous mixture being compressed and then ignited by the action of a spark plug. A flame propagates from the ignition point through the combustion chamber up to the wall, and the propagating speed is mainly a function of the turbulence level in the cylinder. The load is controlled by the amount of mixture inserted in the cylinder and this can be achieved by using a throttle in the intake. Unfortunately this element, especially at partial load, is the cause of pumping losses. The pumping losses are due to the fact that the mixture has to be sucked into the cylinder at throttled pressure, which is below atmospheric, and exhausted at ambient pressure. The proportion between air and fuel is kept at a stoichiometric level and in this way it is possible to achieve both the highest flame speed and allow the Three Way Catalyst to work properly, i.e. oxidize CO and HC, and reduce NO_x.

During the combustion process, one phenomenon that should be avoided is *knock* or spontaneous autoignition. If the pressure and temperature in the end gases, i.e. the not yet burned mixture, reaches autoignition conditions, it is possible to achieve combustion before the passage of the flame. This will cause a rapid pressure increase, an audible knocking sound, and pressure waves all over the combustion chamber. This abnormal combustion should be avoided since it can be the origin of severe damage to the engine. To achieve this goal with a specific fuel, it is necessary to decrease the inlet temperature and/or the compression ratio. The drawback of decreasing the compression ratio is a reduction of the amount of work that can be extracted from the hot burned gases during the expansion stroke. A typical compression ratio value is 10:1. The main emissions from an SI engine are NO_x, CO and HC, and an overview of their formation mechanisms will be given in the section *Emission characteristics*.

3.2 Compression Ignition Engine

In the Compression Ignition (CI) engine, only air is compressed and at the end of the compression stroke the fuel is injected into the cylinder. At the TDC, the pressure and temperature are high enough for the fuel to autoignite. To achieve this target, a high compression ratio is necessary especially during the cold start; and a typical value is 18:1. A high compression ratio leads to more work being extracted during the expansion stroke as compared to an SI engine, thus maintaining the amount of injected fuel constant. When the fuel enters the cylinder, the combustion is achieved in the layer of the spray cone in which air and fuel are mixed in fairly stoichiometric proportions. The combustion duration depends on the mixing time between air and fuel since the temperature is high enough for autoignition to occur, and as a consequence, this duration is directly proportional to the level of turbulence in the combustion volume. The load is controlled by the amount of injected fuel, and the throttle is not used. Consequently, the CI engine displays lower pumping losses at partial load than an SI engine. The main pollutants with this type of ignition process are: NO_x and particulate soot. Further information will be given in the paragraph *Emission characteristics*.

4. Homogeneous Charge Compression Ignition, HCCI

4.1 Introduction and background

HCCI is a third type of ignition process in the world of internal combustion engines, and it has features from both the SI and CI engines. With HCCI combustion, a lean and homogeneous mixture is compressed until the pressure and temperature are high enough for autoignition to occur. Because of the homogeneity of the mixture, the combustion starts simultaneously all over the cylinder; the difference as opposed to knock combustion is the reaction rate. In HCCI combustion this rate is much lower due to a high dilution of the fuel with air or residual gases.

This alternative combustion process was first described by Onishi in 1979 [13] and later by Noguchi [14]; both of which applied the concept to a SI 2-stroke engine. At that time, the objective was to decrease the fuel consumption at partial load by decreasing the cycle-to-cycle variation due to the high amount of retained burned gases. Figure 5 shows the main difference between SI and HCCI combustion. In SI combustion the fuel/air mixture releases all the available energy when the flame passes, while in HCCI only a part of the heat is released by the whole mixture until all of the unburned mixture is consumed.
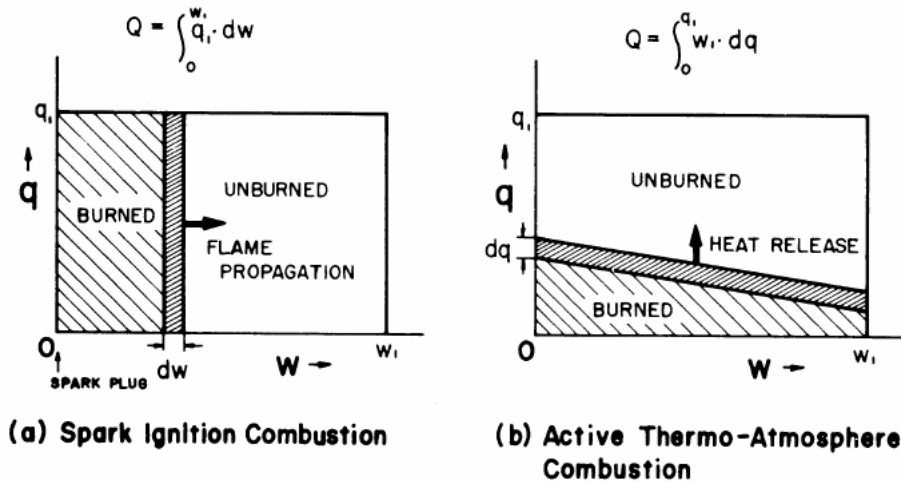
Figure 5: The main difference between SI flame propagation and auto-ignition HCCI [13].

In the eighties, the benefits of HCCI combustion were investigated for a 4-stroke engine. Low NO_x emissions and a high fuel conversion efficiency [15, 16] were found. From the beginning of the nineties, the interest increased and the research involved most of the aspects around this innovative concept.

11

4.2 HCCI ignition process

The autoignition process of HCCI combustion is controlled by the time history of the temperature and pressure during the intake and compression stroke. The autoignition process is governed mainly by the following radicals: H (hydrogen), OH (hydroxyl), H_2O_2 (hydrogen peroxide) and HO_2 (hydroperoxyl) [17, 18]. H_2O_2 and HO_2 concentrations increase progressively during the compression stroke as the pressure and temperature are increased, Figure 6. These two radicals also govern the low temperature reactions (LTR) or, in other words, the cool flame. At temperatures between 1050 and 1100 [K], H_2O_2 decomposes and forms OH that quickly reacts with the fuel molecules to produce heat and water. At this point autoignition starts and high temperature reactions (HTR) take place. At the autoignition point, the concentration of H and OH radicals increase very quickly while the H_2O_2 concentration drops, Figure 6.

The autoignition temperature is a function of the fuel used. For fuels where no LTR take place, e.g. natural gas, iso-octane and gasoline with many aromatics, the autoignition temperature is between 1050 and 1100 [K]. On the other hand, fuels that exhibit LTR, e.g. gasoline with a high paraffin content and fuels containing n-heptane, display autoignition temperatures between 920 and 950 [K], [19, 20].
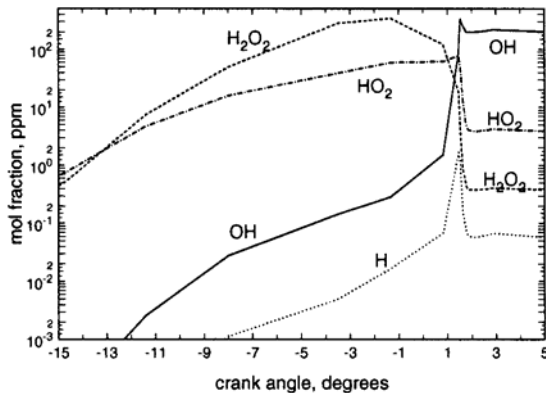
Figure 6: Concentrations of H, OH, H_2O_2 and HO_2 radicals as functions of the crank angle for natural gas not exhibiting two-stage ignition [17, 18].

At the point of the autoignition, when the H_2O_2 decomposes rapidly, the chain branching reactions triggered by this decomposition are:

Fuel + HO_2 → Alkyl + H_2O_2

H_2O_2 + M → OH + OH + M   (H_2O_2 decomposition ➡ autoignition)

Fuel + OH → Alkyl + H_2O

Alkyl $+ O_2 \rightarrow$ Olefin $+ HO_2$

$H + O_2 + M \rightarrow HO_2 + M$ (M = third body species)
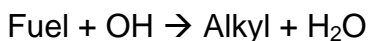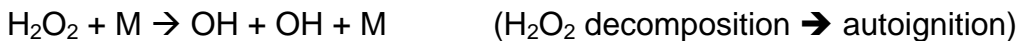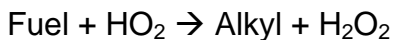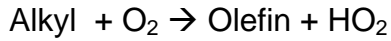
If the temperature is high enough, there is only one single high temperature chain branching reaction [17]:

$H + O_2 \rightarrow O + OH$
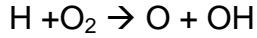
When the combustion involves LTR, the concentrations of CH_2O (formaldehyde), H_2O_2 and HO_2 increase very rapidly during cool flame reactions, Figure 7. A further increase in pressure and temperature is able to stop the LTR because of the third body collision mechanism between OH and H. The concentration of CH_2, H_2O_2 and HO_2 remain constant until the main autoignition, at which point H_2O_2 decomposes very rapidly and OH and H concentrations rise fast.
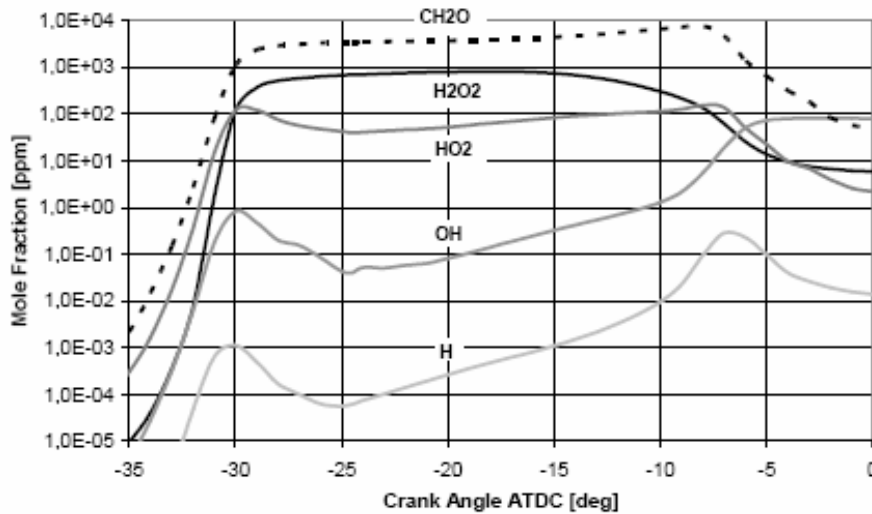
Figure 7: Concentrations of H, OH, H_2O_2 and HO_2 radicals as functions of the crank angle for the 2-stage ignition of PRF 70 [18].

4.3 Advantages and drawbacks of HCCI combustion

The most appealing and at the same time hated feature of HCCI combustion is the fast burning rate. To burn the fuel-air mixture in few CAD means to have a cycle very similar to the ideal Otto cycle which is more efficient than the Diesel one, if the compression ratio is kept constant. Thus short burn duration allows using a larger part of the expansion stroke for producing usable work. For a given output power and compression ratio this means that HCCI engines need less fuel compared to SI and CI which leads to lower CO_2 emission. Moreover the HCCI engine does not have a throttle because the load is controlled by the amount of fuel injected per cycle and this results in lower pumping losses compared to an SI engine running at partial load.

A CI engine has comparatively higher partial load efficiencies but soot, NO_x and smoke emissions are significant. In addition, a means of simultaneously reducing particulate, nitrogen monoxide and dioxide does not exist due to contrasting requirements. HCCI does not give rise to problems with NO_x and soot because due to the fast combustion the residence time of nitrogen at temperature higher than 2000 K (see par. 4.4 & 5.1) is not enough to give rise to substantial values of NO_x moreover the mixture is lean and it burns homogeneously all over the cylinder which prevents soot particle production.

The fast burning duration is an appealing feature of HCCI combustion but unfortunately it results in high pressure rise rate which can not be tolerated because it produces a lot of acoustic noise and it might lead to structural damages. Furthermore, the control of the combustion phasing is difficult since the ignition process relies on the spontaneous autoignition. The last but easy to fix HCCI drawback is the relatively high UHC production due to the low temperature during the cycle, a simple oxidizing catalyst can fix the problem.

4.4 NO$_x$ and soot formation regions

Two of the most appealing features of HCCI combustion are the low NO$_x$ levels, mainly a result of combustion temperatures below 1900 [K], as well as the absence of particulates, due to a premixed mixture and a high air/fuel ratio. However, also in HCCI combustion, in order to avoid NO$_x$ and soot formation, certain combustion regions have to be avoided. Figure 8 shows that the soot formation region is where the equivalence ratio is above 2 and the temperature is between 1700 and 2500 [K]. This is mainly the result of a high temperature and a lack of oxygen facilitating the formation of long-chained hydrocarbons. The thermal NO$_x$ formation regions (*Emission characteristics*) appear when the combustion temperature is above 2000 [K] and the equivalence ratio is below 2.

Figure 8 shows that the HCCI region exists up to a relative air/fuel ratio of 2 which is basically the case of air-diluted HCCI. If exhaust gases are used as diluents, on the other hand, the HCCI region can be extended up to a relative air/fuel ratio of 1. Equivalence ratios larger than one are not interesting in HCCI combustion, since a lack of oxygen can deteriorate the combustion rather quickly.
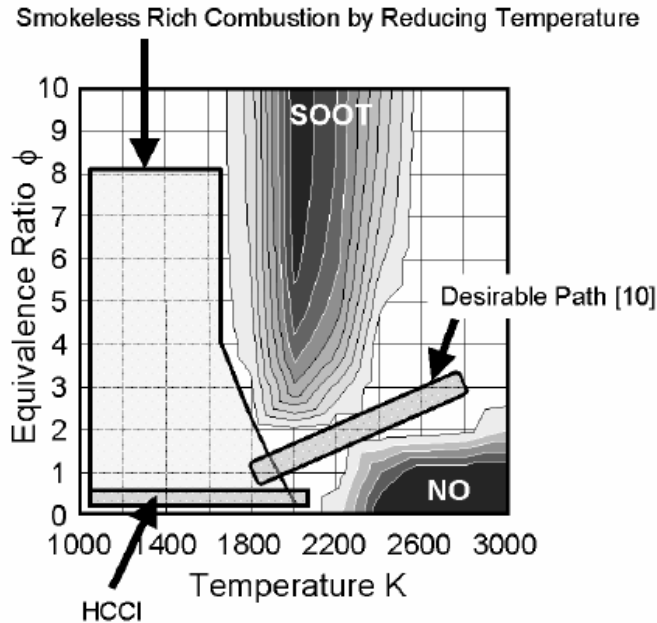
Figure 8: The soot and NO$_x$ formation regions plotted versus their corresponding equivalence ratios and combustion temperatures [21]. Reference 10 in this figure corresponds to reference 22 in the thesis.

4.5 Means for controlling HCCI

The HCCI ignition process is essentially governed by the chemical kinetics of the air/fuel mixture and the time histories of pressure and temperature in the combustion chamber. There are several ways of controlling the combustion phasing:

1- In-cylinder temperature

- Inlet air temperature.
- Compression ratio.
- Amounts of hot exhaust gases.
- Amount of cooled EGR.
- Cooling water temperature, wall temperature.

2- Air/Fuel chemistry

- It can be affected by a dual fuel injection system, i.e. injecting two fuels with opposite ignitability.

3- Mixture compositions

- It can be affected by fuel stratification in direct injection engines.

Some of these variables are much faster than the others and consequently it is possible to use them in a close loop control in order to keep the combustion phasing at the desired value from cycle to cycle.

4.5.1 Exhaust gas diluted HCCI, 2-stroke engines

This type of combustion is also known as ATAC (Active Thermo Atmosphere Combustion). The autoignition is achieved by trapping exhaust gases at partial load by using an exhaust valve that covers part of the exhaust port, Figure 9.
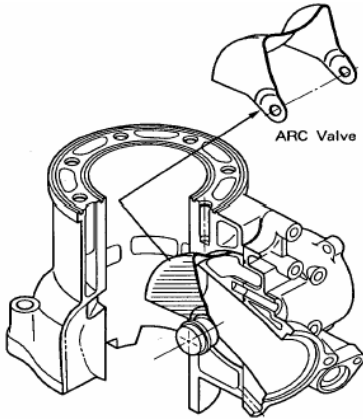
Figure 9: A Honda ARC 2-stroke engine [23].

In Figure 10, ATAC combustion is shown as a function of load and speed while Figure 11 shows the benefits of this new kind of combustion. The hot retained burned gases are able to stabilize the irregular SI combustion at partial load in a 2-stroke engine (COV is lower). The reason for the irregularities is that the high amount of residuals prevent a proper flame initiation when the spark is discharged. ATAC combustion is very difficult to achieve at low speeds and loads as a result of the temperature of the trapped residual gases being too low to initiate autoignition.
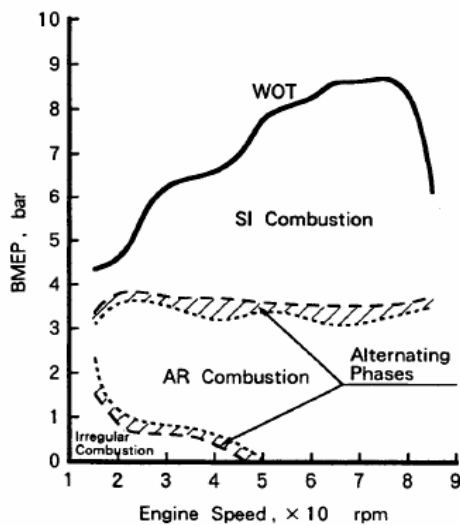
Figure 10: The operating range of ARC combustion in a Honda 2-stroke engine [24].
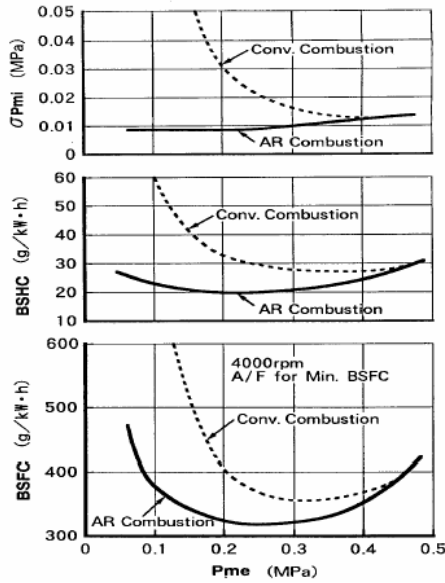
Figure 11: The Honda ARC 2-stroke engine, improvements in fuel consumption, hydrocarbon emissions and standard deviation of IMEP [23].

4.5.2 Exhaust gas diluted HCCI, 4-stroke engines

The autoignition in this case is achieved in the same way as in a 2-stroke engine; i.e. the residuals are trapped using a valve timing strategy: negative valve overlap (NVO) and exhaust valve rebreathing. With NVO the exhaust valve is closed earlier and the intake valve is opened late. This leads to a substantial amount of hot residual being trapped and the quantity is a function of the cam phasing. In Figure 12, SI and CAI (Controlled Auto Ignition) valve timing are shown. In CAI, the valve lift is much lower than in SI in order to avoid excessive accelerations and decelerations of the valve mechanism.
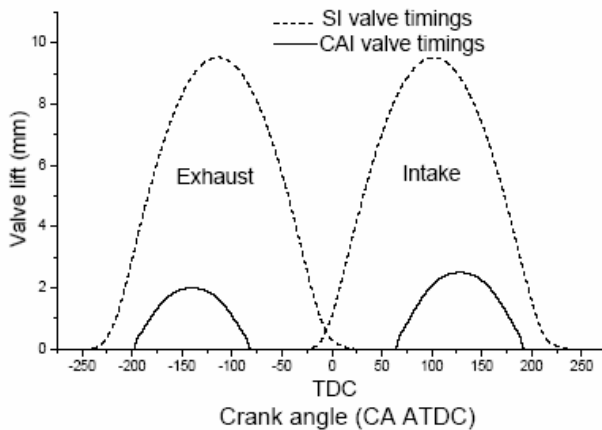
Figure 12: Valve timing strategy in SI and CAI combustion [25].

18

With the rebreathing technique the exhaust valve is opened one more time during the intake stroke thus allowing the exhausted gases to be sucked in. A conventional cam mechanism is not suitable in order to achieve this goal and consequently a valve mechanism that can be directly controlled is required. A Variable Valve Timing System (VVT) is suitable for this application.

With CAI, the maximum load decreases with engine speed since the time for initiating autoignition is lower. When the engine speed is increased, more residuals are needed to increase the charge temperature which simultaneously reduces the amount of oxygen, fuel and load. At low engine speed and loads, the temperature of the retained burned gases is not high enough to autoignite the mixture and misfire can occur. This problem can be solved by direct injection of fuel during the negative valve overlap. In this way part of the fuel is oxidized, leading to an increase in temperature, and the remaining fraction is used during the main combustion event.
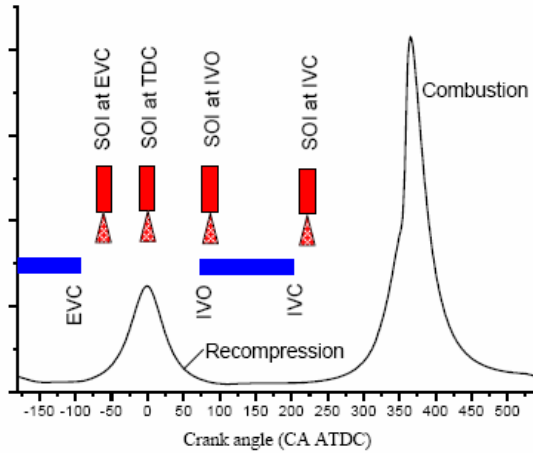
Figure 13: Injection strategies with negative valve overlap controlled autoignition [25].

Spark assisted HCCI combustion is also used for increasing the operative range of HCCI combustion. Even though the condition for having flame propagation is unsuitable, it is still possible to obtain the increased pressure and temperature required to promote the autoignition of the remaining mixture.

19
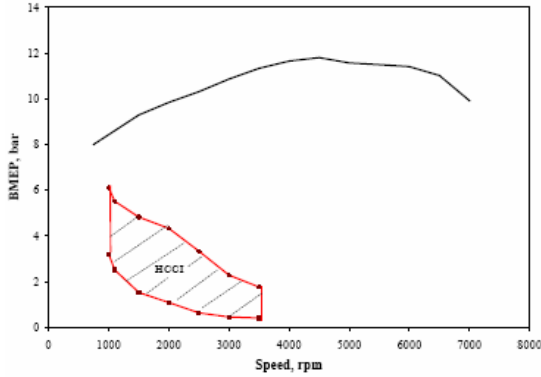
Figure 14: The CAI operating range as a function of speed and load [26].

4.5.3 Air-diluted HCCI

To achieve HCCI combustion in presence of an excess of air, it is necessary to increase the temperature and/or the pressure in order for autoignition to occur. The inlet air can be warmed up by using an electrical heater or an exhaust-inlet heat exchanger. On the other hand, the compression ratio can be adjusted by the use of a Variable Compression Ratio Mechanism or the Inlet Valve Closing. Figure 15 shows the relation between the effective compression ratio, the inlet air temperature and the fraction of gasoline in diesel fuel for achieving autoignition around TDC.
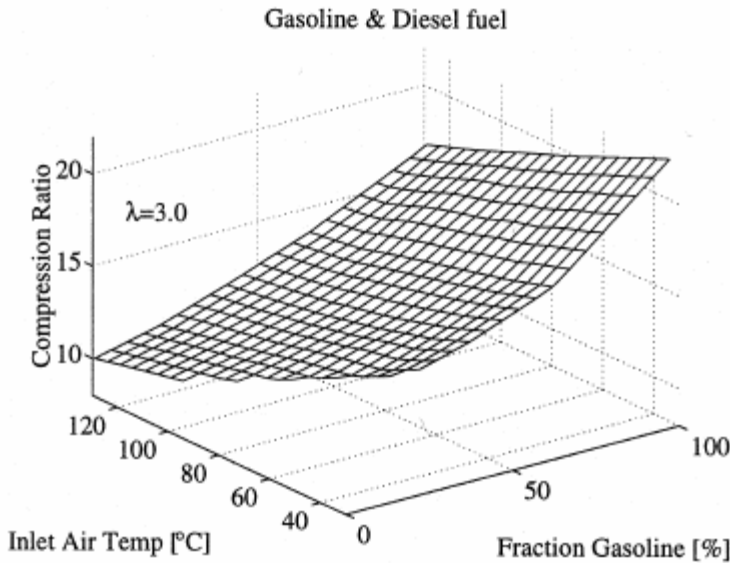
Figure 15: The relation between the compression ratio and the inlet air temperature with different mixtures of gasoline and diesel [27].

The inlet air temperature can be used for controlling the combustion phasing of HCCI combustion. For instance, heated and unheated air can be mixed in order

to achieve the desired temperature; the heat can be extracted from the cooling water and exhaust system [28]. Using a blend of two fuels with opposite ignitibility is another methodology for controlling the combustion phasing in air diluted HCCI [29].

It has to be underlined that using an excess of air rather than EGR is beneficial as a result of the ratio of specific heat being higher thus leading to a better thermodynamic efficiency. Also, in the case of air-diluted HCCI, the maximum load is limited by the pressure rise rate in the sense that when it is too high it becomes the source of audible noise.

4.5.4 Partially premixed combustion

Partially premixed combustion is an HCCI concept developed from a standard diesel engine and its main goal is to avoid the regions were NO_x and soot are formed, Figure 8. Two strategies have been proposed: one from Toyota and the other from Nissan. In the Toyota UNIBUS strategy there are two main injections; the first one is used for achieving a homogeneous mixture while the second controls the ignition timing [30]. Autoignition is achieved at the end of the second injection. Unfortunately, it is not possible to use this strategy in the entire operating range of the engine basically because the ignition of the diesel fuel can occur before a homogeneous mixture is achieved.

The Nissan MK concept consists in increasing the amount of EGR in order to increase the ignition delay and hence provide a homogeneous fuel/air distribution. It consists of three design steps; in the first, the amount of EGR is increased, in the second, the injection timing is retarded in order to obtain a further increase of the ignition delay and the third step consists in increasing the swirl ratio just before the autoignition in order to promote the mixing between fuel and air.

5. Emission characteristics

The regulated emissions for an internal combustion engine are: NO_x, CO, HC and PM. CO_2 is not a pollutant in the same meaning as the previous substances but it has a large environmental impact as it is a green-house gas. In this section a very brief description of the formation mechanism for each substance is given.

5.1 NO_x

This acronym is used for indicating both nitrogen monoxide, NO, and nitrogen dioxide, NO_2. In an internal combustion engine three processes are responsible for NO_X formation:

- Thermal NO_x.
- Prompt NO_x.
- Fuel NO_x.

Thermal NO_x has been extensively described by Zeldovich and is the product of the oxidation of the nitrogen present in air. The formation rate is exponentially dependent on the temperature, Esquation 1. The factors that affect its amount are: flame temperature, residence time at that temperature, homogeneity of the mixture and concentration of oxygen and nitrogen in the flame.

Equation 1: NO_x formation rate according to the Zeldovich mechanism.

$$\frac{d[NO]}{dt} = 6x10^{16}T^{-0.5}\exp\left(\frac{-69090}{T}\right)[O_2]^{0.5}[N_2]$$

HCCI combustion takes place in a highly diluted and homogeneous mixture and consequently the combustion temperature is rather low. Furthermore, the combustion is very fast, and these two effects result in very low NO_x emission levels.

The Prompt NO_x is the result of fast reactions in fuel-rich flame fronts or through intermediate NO_2 reactions [31]. The third mechanism for NO_x formation is fuel NO_x, which means the formation of nitrogen monoxide and dioxide from nitrogen contained in the fuel.

5.2 CO

Carbon monoxide, CO, is the result of an incomplete oxidation of the fuel and depends to a large degree on the relative air/fuel ratio. Its amount is very high for rich mixtures and inhomogeneous charge distributions. In the case of a lean and homogeneous mixture, its amount is influenced by the combustion temperature - if it is too low, reactions that lead to CO_2 are frozen and CO is obtained.

5.3 HC

The main sources for unburned or partially burned hydrocarbons include:

- Wall quenching.
- Crevice volume.
- Bulk quenching.
- Oil absorption.

Since the radical recombination is faster than the radical formation, a quenching distance exists on the combustion chamber walls, i.e. fuel does not react next to the walls. During the expansion stroke these hydrocarbons are sucked into the bulk volume and are then flushed out during the exhaust stroke.

During the compression stroke, a percentage of the fuel can be trapped in the crevice volumes, mainly in the gap between the piston and liner above the first piston ring. If this gap is smaller than the quenching distance, the trapped mixture does not react and with the aforementioned mechanism it is pushed out during the exhaust stroke.

Bulk quenching is the result of incomplete reactions due to a rapid temperature drop. This phenomenon occurs with very lean mixtures and very advanced combustion phasing. If the temperature in the expansion stroke is too low, i.e. the heat produced by the reactions is not sufficient to compensate for the temperature drop caused by the increase in cylinder volume, this may lead to quenching of the burning mixture.

During the compression stroke, a percentage of the fuel may be absorbed into the oil layer which is stuck on the cylinder walls and piston top land. In the expansion stroke, desorption occurs and the unreacted fuel is flushed out in the exhaust stroke.

It is important to underline that: during the expansion stroke, if the in-cylinder temperature is high enough and if oxygen is present, a certain amount of the

hydrocarbons (coming from the crevice, wall quenching and desorption from the oil layer) can react thus giving rise to lower UHC emissions.

5.4 Particulate matter

Particulate matter is formed during incomplete combustion especially from direct injection gasoline and diesel engines where insufficient mixing between fuel and air occurs. At 800 K, the particulate matter is principally a cluster of many small carbon spheres with very small amounts of hydrogen. At temperatures below 800 K these particles are coated with UHC and inorganic species such as sulfur dioxide and nitrogen dioxide.

5.5 Sulfur dioxide

SO_2 is formed during the combustion of sulfur-containing fuels. The amount of SO_2 emitted by cars and trucks has decreased during the years due to the decrease in the amount of sulfur in the fuel.

5.6 CO_2

Carbon dioxide is a natural combustion product together with water. CO_2 is considered a green house gas and increasing its amount in the atmosphere contributes to the global warming effect. Its emission has yet to be regulated. A reduction of CO_2 can be achieved by using engines that burn less fuel without compromising the output power (i.e. with a higher efficiency); with HCCI combustion it is possible to achieve this goal.

6. Heat release analysis

The in-cylinder pressure data were analyzed using a single zone heat release model. Such a model assumes that the temperature and mixture distribution are homogeneous all over the combustion chamber. With a car/truck-sized HCCI engine, this is a good assumption since the combustion occurs almost simultaneously throughout the entire combustion chamber. Even though the temperature is somewhat lower in the boundary layer, the use of this model still provides good results in such *big engines*.

Optical measurements [32, 33] have shown that when HCCI combustion occurs in a small volume, the boundary layer is 13% in the radial direction and 100% in the axial one because of the high surface to volume ratio when the piston is at TDC. As a consequence, and even though the mixture distribution is fairly uniform, the temperature gradient cannot be neglected. In this case, a multi-dimensional model would have been more appropriate but in order to obtain a reasonable computational time and avoid the use of more sophisticated approaches that would introduce more variables and thus more uncertainty, it was decided that the conventional basic model should be employed.

6.1 The basic model

This subsection describes how to obtain the equation used in the single zone heat release model. The first law of thermodynamics is applied to the combustion chamber volume which is assumed to be an open system:
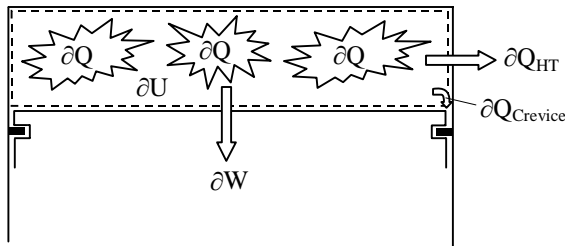
Figure 16: The energy balance inside the combustion chamber volume.

$$\partial Q = \partial U + \partial W + \partial Q_{HT} + \partial Q_{Crevice}$$

Here:

∂Q is the spatial averaged instantaneous heat release.
∂U is the change in internal energy.
∂W is the work performed by the gases on the piston.
∂Q_{HT} is the spatial averaged instantaneous heat transfer to the cylinder walls.

$\partial Q_{Crevice}$ represents the energy equivalence of the mass flow across the system boundaries.

The internal energy can be rewritten as:

$$U = mc_v T$$

Differentiating:

$$\partial U = mc_v dT + udm$$

Neglecting the blow-by, dm=0. Now considering the ideal gas law and assuming that the universal gas constant does not change significantly during the entire cycle:

$$pV = mRT$$

$$\partial T = \frac{1}{mR}\left(pdV + dpV\right)$$

Substituting this last equation in the expression for the internal energy yields:

$$\partial U = \frac{c_v}{R}\left(pdV + dpV\right)$$

The work performed on the piston by the gases can be expressed as:

$$\partial W = pdV$$

Combining everything together and keeping in mind that the blow-by has been neglected, $\partial Q_{Crevice}=0$,

$$\partial Q = \left(1 + \frac{c_v}{R}\right)pdV + \frac{c_v}{R}dpV + \partial Q_{HT}$$

The gases have been modeled as ideal which means:

$$R = c_p - c_v$$

$$\gamma = \frac{c_p}{c_v}$$

Rearranging the heat release expression and dividing it with the variation of crank angle, dΘ,

$$\frac{\partial Q}{\partial \theta} = \frac{\gamma}{\gamma - 1} p \frac{dV}{d\theta} + \frac{1}{\gamma - 1} V \frac{\partial p}{\partial \theta} + \frac{\partial Q_{HT}}{\partial \theta}$$

When the in-cylinder pressure, the volume trace and the heat transfer are known, the rate of heat release can be calculated. For a conventional-sized engine and when using normal diesel or gasoline fuel, the polytropic exponent, γ, is 1.30 during the compression and 1.33 during the expansion. The value is larger during the expansion because of the higher heat loss to the combustion chamber walls. During the combustion a linear interpolation between these two values can be used [34].

6.2 Heat transfer modeling

In the previous paragraph, one of the variables necessary for computing the net heat release was the spatial averaged heat transfer. The most used expression for computing this parameter in SI, CI and HCCI engines is the Woschni's correlation [34, 35]. The fundament of this model is the assumption that the Nusselt, Reynolds and Prandtl number relationship follows the one found for turbulent flow in pipes or over flat plates:

$$\mathrm{Nu} = A\,\mathrm{Re}^{b}\,\mathrm{Pr}^{c}$$

Unfortunately, this model is unsuitable for computing the heat transfer in small combustion chambers. Because of the speed of the engine and since a simple carburetor as the injection system is used, the fuel it is not perfectly vaporized when it enters the cylinder. Consequently, during the compression stroke, part of the compression energy is used in order to obtain vaporization, and thus the ratio of specific heat is not constant during the compression, Figure 17.
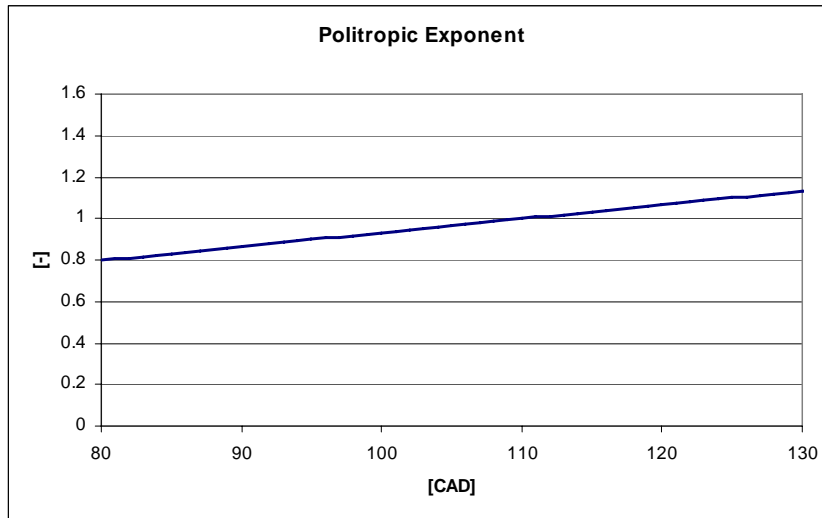
Figure 17: The variation of the polytropic exponent during the compression stroke.

Prof. Tunestål has introduced a self-tuning heat release model [36] that computes the instantaneous polytropic exponent immediately preceding and succeeding the combustion event. A linear interpolation of these values is performed during the combustion, and the ratio of specific heat trace is used for calculating the net heat release. The use of this interpolated exponent implicitly incorporates a model for losses (heat losses, crevice losses and blow-by) into the net heat release equation:

$$\frac{\partial Q}{\partial \theta} = \frac{\gamma_i}{\gamma_i - 1} p \frac{dV}{d\theta} + \frac{1}{\gamma_i - 1} V \frac{\partial p}{\partial \theta}$$

Here, γ_i is the instantaneous ratio of specific heat.

With this model the heat transfer can be very well predicted. In Figure 18 the total heat release has been computed using the Tunestål model.
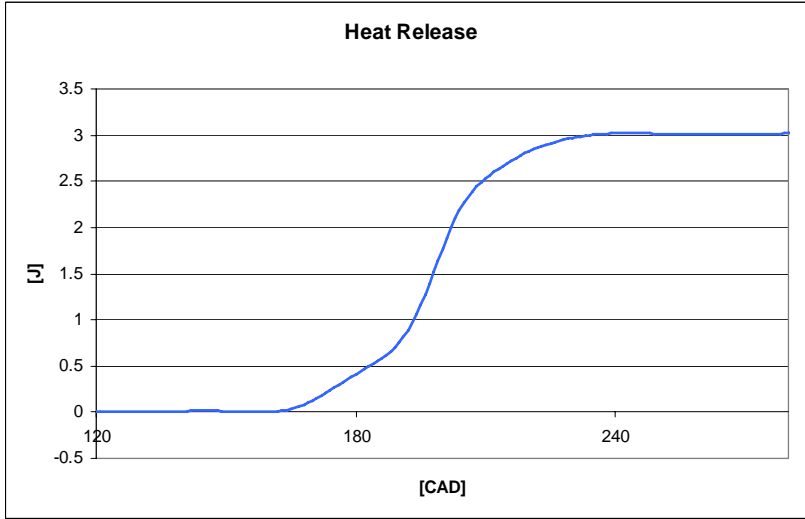
Figure 18: The net heat release as computed by the Tunestål approach.
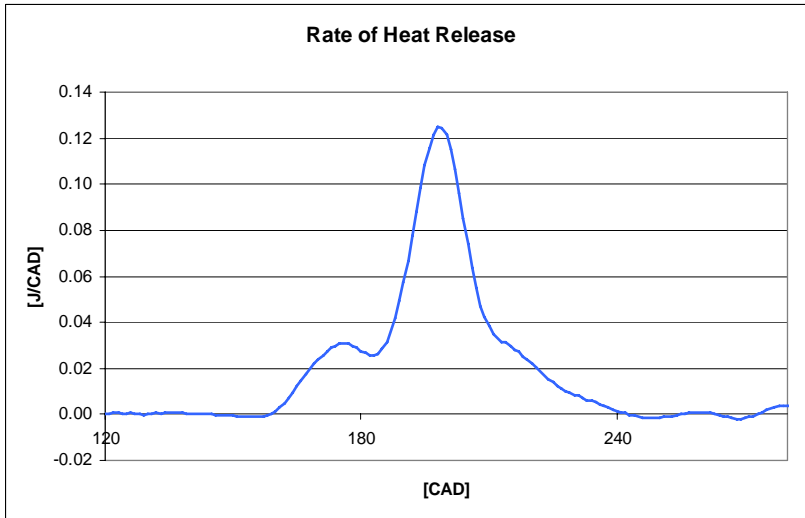
Figure 19: The net rate of heat release as computed by the Tunestål approach.
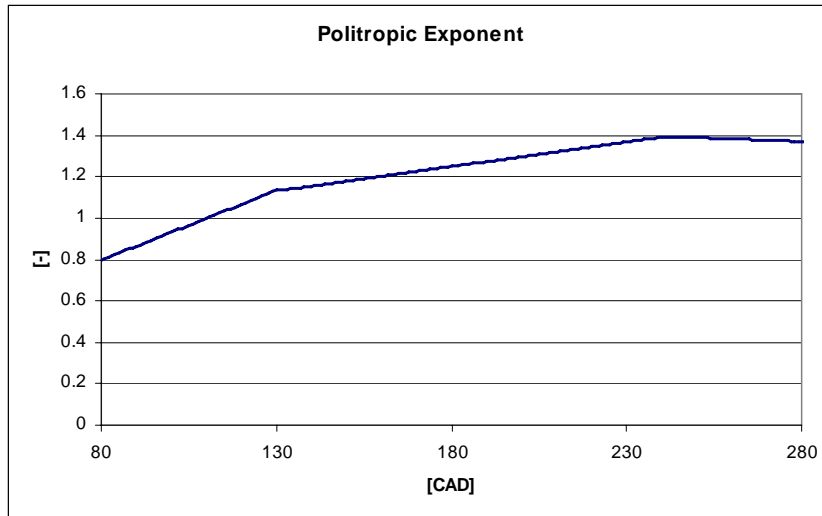
Figure 20: A typical instantaneous polytropic exponent trace during compression, combustion and expansion.

7. Flame quenching

Since the present thesis deals both with combustion in a small volume and with the design of a miniature free piston engine, quenching phenomena need to be taken into account in order to understand certain observations during the investigations and also to successfully design a mini free piston engine. This chapter offers a short review of the fundamentals behind flame quenching.

Flame quenching occurs at the walls of the engine's combustion chamber, as a result of the cool walls acting as a sink for heat and the active radicals generated within the flame. Quenching can occur under several different geometrical configurations: the flame may propagate normally, in parallel to or with an angle to the wall.

The flame quenching process is analyzed by relating the heat released by the flame with the heat lost at the walls, and the ratio of these two quantities is the Peclet number, Pe. This number is almost constant for any given geometrical configuration. Using two parallel plates, the minimum distance for flame propagation to occur implies having a Pe number close to 40 and this is valid for a wide range of conditions. In the present case, the Peclet number can be expressed as:

Equation 2: The Peclet number for two parallel plates.

$$Pe_2 = \frac{\rho_u \cdot S_L \cdot c_{Pf} \cdot (T_f - T_u)}{k_f \cdot (T_f - T_u)/d_q^2} = \frac{\rho_u \cdot S_L \cdot c_{Pf}}{k_f / d_q^2}$$

where $\rho_u, S_L, c_P, \mathrm{T}$ and k are respectively: density, laminar flame speed, specific heat at constant pressure, gas temperature and thermal conductivity. The subscripts u and f refer to unburned and flame conditions, respectively. When all these parameters are known, the quenching distance d_q, can be estimated.

For this geometrical configuration Lavoie [34] has developed an empirical correlation for calculating the minimum Pe number, without the quenching, being a function of the pressure and equivalence ratio:

Equation 3: The empirical Peclet number expression as developed by Lavoie.

$$Pe_2 = \frac{9.5}{\phi} \cdot \left(\frac{P}{3}\right)^{0.26 \cdot \min\left(1, 1/\phi^2\right)}$$

Here, P is the pressure expressed in atmosphere and ϕ is the equivalence ratio. The expression is valid in a pressure range between 3 and 40 [atm].

For one wall quenching distance, and when the flame is perpendicular to the plate, the Pe number can be expressed as follows:

Equation 4: The Peclet number for one wall quenching distance.

$$Pe_1 = \frac{\rho_u \cdot S_L \cdot c_{Pu}}{k_u / d_q^2} \approx 8$$

The subscript u denotes the properties evaluated for unburned gas conditions.

8. Boundary layer

Conventionally, the boundary layer thickness is defined by a certain percentage of e.g. free stream velocity. In the case of internal combustion engines, it can be defined as a percentage of the temperature of the bulk gases. Unfortunately, it is certainly not simple to measure the temperature distribution and substantial modifications are required on the test engine. More commonly, this thickness is calculated by acquiring chemiluminescence images of the combustion. The boundary layer thickness is then defined as the distance between 1 and 85% of the maximum derivative of the natural emitted light [37].

It is important to know the percentage volume mainly because this colder layer of gas prevents oxidation, leading to higher fractions of surviving hydrocarbons and intermediate combustion products at the end of the expansion stroke. Because of the higher density, a substantial fraction of the cylinder mass is contained within the thermal boundary layer. According to Heywood, for an average thickness of 3 [mm] at 90 CAD ATDC during the expansion, the volume of the boundary layer is 20% of the volume of the combustion chamber for typical engine dimensions. In this zone, since the average density is approximately twice that of the bulk gases, around 30 - 40% of the cylinder mass would be contained within this boundary volume.

Once again according to Heywood, the variation in boundary layer during the entire cycle is the following: the boundary layer thickness decreases during the intake and increases steadily during the compression and expansion up to 2 [mm]. It is relatively unstable during the exhaust process. During the overall cycle, the thickness is a function of the location throughout the chamber. The boundary layer on the piston crown and cylinder head is 2 – 3 times thicker than the one on the walls (using a disc-shaped combustion chamber), and the reason for this could be the absence of bulk flow adjacent to the head and piston top [38].

9. Experimental apparatus

9.1 Engine

An O.S. 25 single cylinder, 2-stroke, air cooled engine was used in all measurements. Three main cylinder head designs were employed; a bowl combustion chamber for achieving combustion through the action of a glow plug, and pancake and bowl configurations for running the engine in HCCI mode.

Figure 21: The O.S. 25 single cylinder engine.
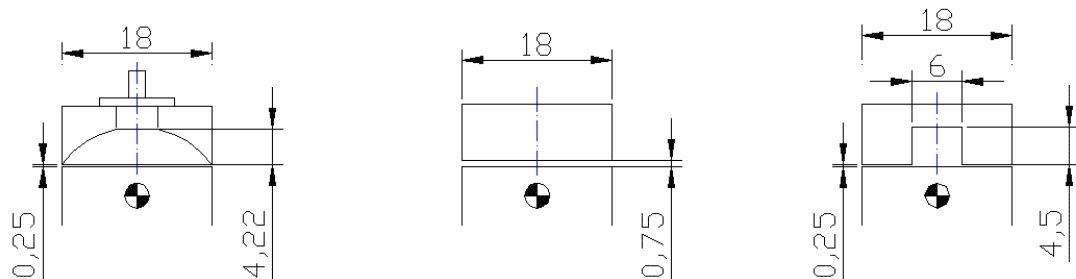
Figure 22: From left to right: the bowl chamber used during the glow plug experiments, the pancake and bowl combustion chambers used during the HCCI experiments.

Table 2 shows the timing of the intake and exhaust ports; the ports were designed and placed in a loop scavenging configuration.

Table 2: Geometrical properties of the test engine.

Displacement	4.11 [cm3]
Bore	18.00 [mm]
Stroke	16.50 [mm]
Exhaust port open	74 [BBDC]
Exhaust port close	74 [ABDC]
Intake port 1 open	58 [BBDC]
Intake port 1 close	58 [ABDC]
Intake port 2 open	37 [BBDC]
Intake port 2 close	37 [ABDC]

Table 3 shows the geometrical compression ratio. For the pancake combustion chamber, this parameter was changed by modifying the clearance height with various spacers. Because of the absence of piston rings, the effective compression ratio was much smaller than the geometrical one.

Table 3: Geometrical compression ratio.

Glow Plug		13.91	[-]
HCCI	Pancake	46.27	[-]
		23.63	[-]
		16.09	[-]
		12.32	[-]
		10.05	[-]
	Bowl	16.09	[-]

The injection of fuel was achieved by employing an elementary carburetor. This simple type of injection system had many deficiencies [34], for instance:

- At low load the mixture became leaner.
- At intermediate load the equivalence ratio increased slightly.
- The transient phenomena in the intake manifold were not compensated for.
- The mixture could not be enriched during the start-up or warm-up.
- It could not adjust to changes in ambient air density.

For these reasons, during all the measurements, the needle position was manually adjusted in order to obtain a maximum performance.

9.2 Load and Speed

The first three papers, that this thesis is based on, describe how the load and the speed were changed using propellers of various length and pitch, since these two parameters affected the output power in the following manner:

Equation 5: The output power as a function of engine speed and propeller geometry.

$$Power = const \cdot pitch \cdot diameter^4 \cdot RPM^3$$

Despite not using a closed-loop control for maintaining a constant speed, it was found that the COV of this parameter was between 0.2 and 0.4% in 200 cycles.

The last three papers report on the implementation of a closed-loop control in order to decrease the variation of the rotational speed of the engine. This was achieved by mounting an electric DC motor on the same shaft of the engine. This motor was a BOSH GOF 2000 CE that allowed a maximum speed of 30000 [rpm] and a maximum torque of 2 [Nm].

Figure 23: The BOSCH GOF 2000 CE.

9.3 Wall temperature control

The cylinder walls were cooled down in two ways: by air blown by the propeller and by custom-made cooling systems. The tailor-made coolers were only used during the HCCI operations mainly since the engine was connected to the electric motor and the cooling air flow from the propeller was no longer available. In this case the cooling system consisted of two parts: the first one was placed in front of the cylinder and was used for controlling the temperature of this element

while the second was necessary for cooling the carburetor. When the engine was running in HCCI mode, di-ethyl-ether, DEE, was used as fuel. This compound has a very low vaporization temperature. Moreover, when it passes through the hot carburetor, the fuel is vaporized and due to the resulting over pressure, it is pushed back in the tank thus giving rise to an unstable behavior of the engine.
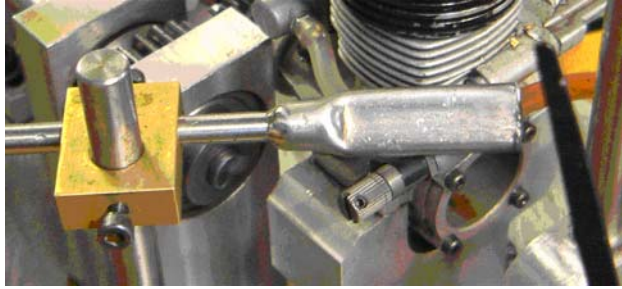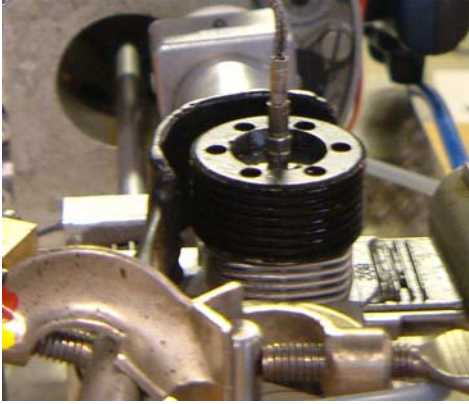
Figure 24: Cylinder cooling system.   **Figure 25: Carburetor cooling system.**

9.4 Inlet air heating

When the engine was running using the glow plug, as reported in Paper 1, a heater was employed for investigating the influence of warmer inlet air on the performance and emission of the engine. The heater was a Steinel HL 2010 E and a custom-made heat exchanger was designed for warming up the inlet charge.

Figure 26: Electrical heater.   **Figure 27: Heat exchanger.**
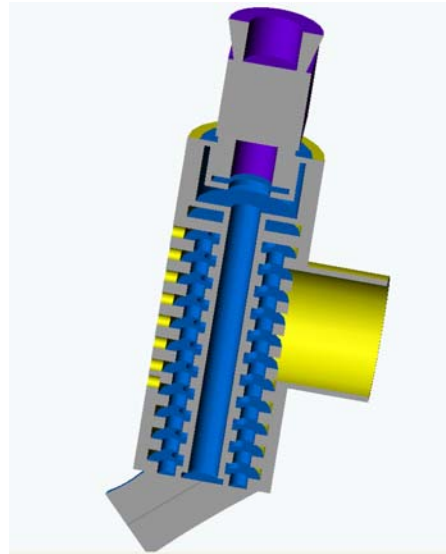
9.5 Exhaust gas analysis

Boo Instrument AB equipment was used for measuring the emissions. This device was able to detect HC, NO_x, CO_2, O_2 and CO. The HC and NO_x were measured wet while all the other gases were dry. The calibration was performed with specific concentrations of various span gases, and the zero level was found when using nitrogen as the zero gas.

The unburned and partially burned hydrocarbons were measured with a *Hydrocarbon Analyzer Model 109A*. This technique uses a Flame Ionization Detector (FID) and the measuring range was 0 – 100000 ppm. In order to support the flame, a gas mixture of 60% helium and 40% hydrogen was needed.

The *ECO Physics CLD 700 EL ht* was used for measuring NO_x. A Chemi Luminescence Detector (CLD) was employed and the instrument range was 0 – 10000 ppm.

The CO, CO_2 and O_2 concentrations were acquired with *UNOR 611* from *Maihak* using a Non Dispersive Infra Red analyzer (NDIR). CO_2 was measured in the range 0 - 16%, O_2 in the range 0 - 25% and CO in the range 0 - 10%.

9.6 Fuels

A variety of fuel blends were investigated in these experiments, and the basic compounds consisted of: ethanol, methanol, nitromethane and diethyl ether. Their properties are listed in the Table 4.

Table 4: Fuel properties.

	Formula	Q_L [MJ/kg]	α_{sotich} [-]	Octane Number
Ethanol	C_2H_6O	26.9	9	107
Methanol	CH_4O	20	6.47	106
Diethyl ether	$C_4H_{10}O_2$	36	11.2	-
Nitromethane	CH_3NO_2	10.5	1.69	-

9.7 Optical access

Optical access can be achieved in a variety of ways through piston, cylinder liner or cylinder head, depending on the type of diagnostic that is performed. Because of the small dimensions of the engine, the optical window was placed on the cylinder head for both the glow plug and HCCI engine. The field of view field was 100%. When the glow plug engine was used, this trigger device was mounted on the liner. To allow measurements of the cylinder pressure, the pressure sensor was mounted on the cylinder wall. An L shaped channel was drilled in the liner in order to achieve communication between the membrane of the sensor and the combustion chamber.
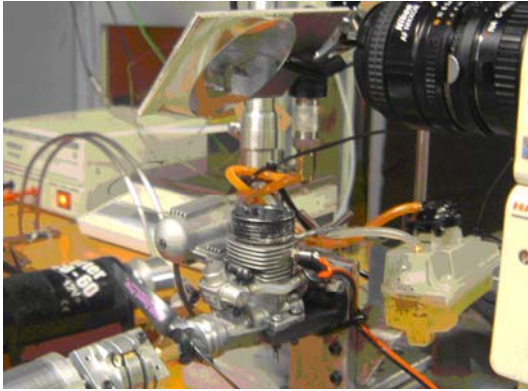
Figure 28: O.S. 25 with optical access.
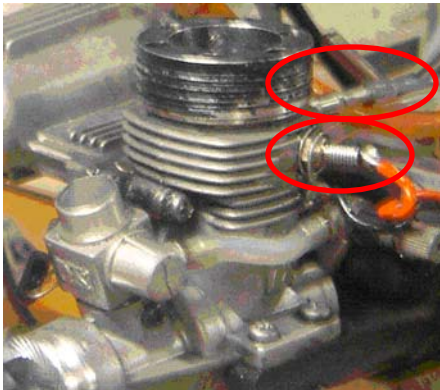
Figure 29: Glow plug and pressure sensor locations.
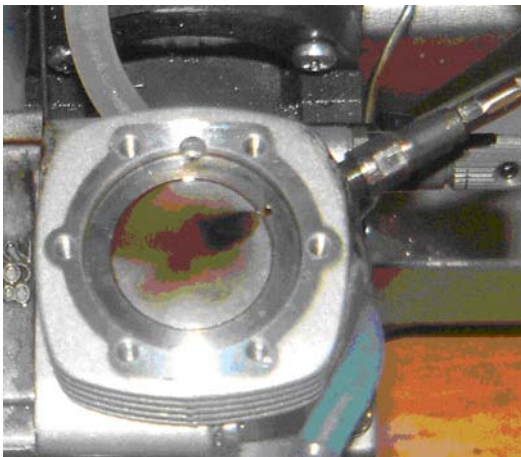
Figure 30: The pressure sensor location with the engine running in HCCI mode.

During the optical diagnostic measurements, the light emitted from CH, OH (hydroxyl) and C_2 radicals was recorded. This was performed by applying three band pass filters in front of the high speed camera:

Table 5: Filter specifications.

Species	Center Wavelength	Peak Transmittance
OH	308 [nm]	15%
CH	431 [nm]	40%
C_2	560 [nm]	45%

9.8 Data logging

A National Instrument SC-2345 data logger was used for data acquisition and closed-loop controls. It consisted of 16 analog inputs, 8 digital I/O lines and 2 unconditioned counter/timer I/O lines. The recorded data were mainly the temperatures, pressures, and the CAD and TDC signals coming from the encoder mounted on the same shaft of the engine. The temperatures were measured with thermocouples, type K, from Pentronic. The exhaust and crankcase pressures were acquired using a Keller PR 23 S piezoresistive pressure sensor, while the in-cylinder pressure was measured with a piezo-electric transducer.

9.9 Cylinder pressure measurements

The cylinder pressure changed because of variations in volume, combustion and heat transfer. Precise in-cylinder pressure measurements were vital in order to understand the behavior of the combustion by means of indicated work, efficiencies and also combustion phasing.

9.9.1 Pressure transducer

A piezoelectric pressure sensor was used for recording the instantaneous in-cylinder pressure. It consisted of a quartz crystal that was exposed to the gases through a diaphragm. When the pressure deformed the crystal, it produced an electric charge proportional to the pressure in the combustion chamber. Because of its nature, this transducer was only capable of measuring pressure changes and not absolute values as a piezoresistive sensor can do. During the present study, a Kistler Type 6052 C pressure transducer was used. This device was air cooled and such a cooling method was more than enough considering the small dimensions of the combustion chamber.

9.9.2 Charge amplifier

The charge produced by the quartz crystal was received by the charge amplifier whose task was to convert the incoming signal into voltage. A Kistler Type 5011 was employed to this effect and was used with an output signal of ±10 volts.

9.9.3 Determination of the calibration constant

The calibration constant of the pressure transducer could be obtained in three ways.

1-

Equation 6: Calibration constant function.

$$Cal\_const\left[\frac{Pa}{count}\right] = \frac{Range}{2^{Bits}}\left[\frac{V}{count}\right] \cdot S\left[\frac{MU}{V}\right] \cdot T\left[\frac{pC}{MU}\right] \bullet \frac{1}{C_{PT}}\left[\frac{Pa}{pC}\right]$$

Here:

The range implies the voltage measurement range in the A/D converter, and normally lies between -10 to +10 volts resulting in a range of 20 volts.
C_{PT} is the pressure transducer sensitivity given by the manufacturer.
T is the charge amplifier scale.
S is the charge amplifier sensitivity which is normally set equal to the pressure transducer sensitivity.
Bits are the number of bits of resolution in the A/D converter, and in the present studies a 16 bit A/D converter was used.

2- Another method is to calibrate the sensor using a known pressure, for instance by motoring the engine without exhaust manifold. The average pressure in the exhaust stroke can be assumed to be equal to 1 bar.

3- The last method is to use a static load. However, a significant drawback is that the dynamic properties of the transducer are not taken into account.

9.9.4 Pressure reference level

The pressure transducer only measured changes in pressure and consequently a reference level was needed. Three methods can be used:

1- The average cylinder pressure during the inlet stroke could be set equal to the intake manifold pressure. The average cylinder pressure was lower compared to the intake manifold pressure due to the pressure drop over the intake valve. This first point is valid for a 4-stroke engine, and can with certain changes also be used for a 2-stroke engine.

2- The cylinder pressure at the inlet BDC could be set equal to that of the intake manifold. This is valid for both 2 and 4-stroke engines.

3- The cylinder pressure at the gas exchange TDC could be set equal to the average measure exhaust backpressure. This is only valid for 4-stroke engines.

The author used method number 2.

10. Results: Glow Plug Engine

10.1 Introduction

A glow plug ignition engine is neither an SI nor a CI engine. In this kind of combustion, a mixture of fuel and air is compressed and then the ignition occurs as a result of:

- Compression energy.
- Heat supplied by the glow plug.
- Catalytic effect of the platinum wire of the glow plug.

There is no way to control the ignition timing basically because the process relies on a certain type of autoignition triggered by the glow plug. The glow plug element consists of a metal body, a central conductor and a coiled wire. The conductor and the wire sit inside the metal body, and one end of the wire is connected to the conductor and the other to the body. The conductor and the metal body are insulated from each other. The wire is an important part in the glow plug. Materials used in the wire vary considerably, but an important component is platinum, which can act as a catalyst. When the engine is cold (during starting), catalytic heating is not sufficient for autoignition, and therefore the wire is connected to a battery that causes resistive heating. Once the engine is running, the battery is disconnected and heating is provided to the plug element in three ways:

- The element remains hot from the previous cycle.
- Heat is generated by the compression of the air/fuel mixture.
- Heat is generated by catalytic action between the platinum alloy of the plug element and the fuel.
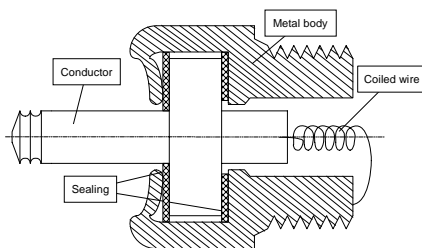
Figure 31: A sketch of a model engine glow plug.

10.2 Engine characterization

Since ethanol is an environmentally friendly fuel that can be obtained directly or indirectly from biomass at the cost of 1 $/gallon, the original idea was to use this fuel with HCCI combustion for the VIMPA engine. As a starting point for understanding how combustion behaves in a small volume at a high engine speed, a study of the behavior of a model airplane glow plug engine was carried out.

One of the VIMPA specifications was to obtain an as high as possible working frequency and consequently the tests were performed between 14500 and 17500 [rpm]. The speed was changed by using six different propellers; even though an electric motor was not used for keeping the speed constant, the coefficient of variation of this parameter was between 0.2 and 0.4 %. The fuel was a blend of 90% ethanol and 10% lubricant.

Table 6: Propeller specifications.

Propeller	Diameter [inch]	Pitch [inch]
1	8	4
2	9	4
3	9	6
4	10	7
5	10	8
6	11	9

Figure 32 displays the cylinder pressure traces. Even though glow plug combustion is a kind of autoignition process triggered by the glow plug element, the combustion event seems to be very soft, resulting in a low pressure rise rate (Figure 33). This resembles the ATAC combustion studied by Onishi [13], in which the high amount of retained burned gases, used for achieving autoignition, led to a soft release of heat. Figure 34 shows the amount of burned trapped gases estimated by a custom-made model, cf. chapter 12.
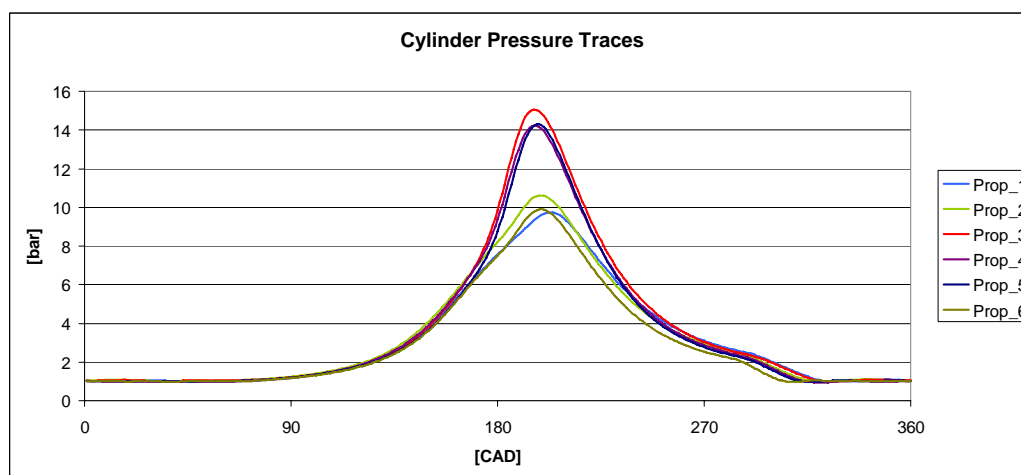
Figure 32: In-cylinder pressure traces acquired with a glow plug engine between 14500 and 17500 [rpm]. Propeller 1 is the fastest and propeller 6 the slowest.

Max Pressure Rise Rate

Figure 33 chart
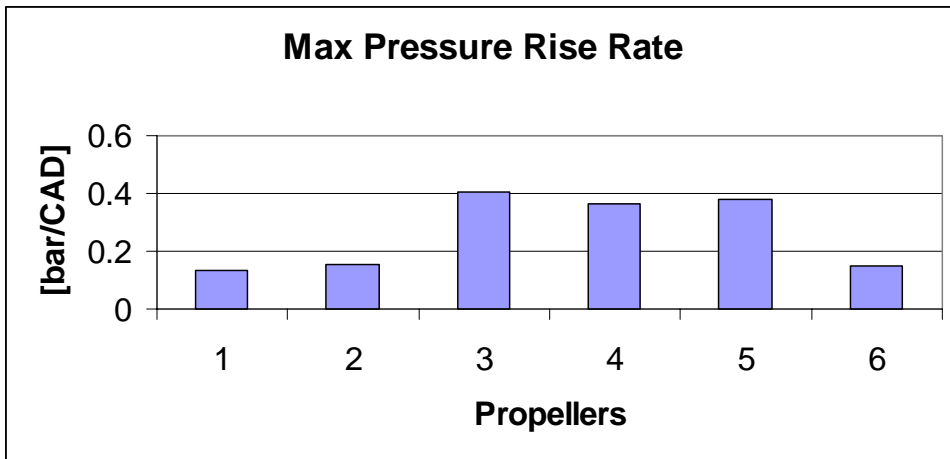
Figure 33: The maximum cylinder pressure rise rate acquired with a glow plug engine between 14500 and 17500 [rpm]. Propeller 1 is the fastest and propeller 6 the slowest.

Retained Burned Gasses

Figure 34 chart
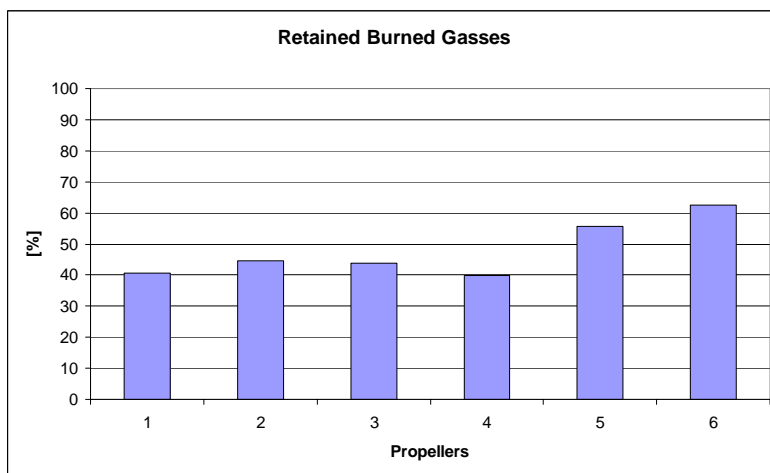
Figure 34: Estimated residual gases during six tests between 14500 and 17500 [rpm]. Propeller 1 is the fastest and propeller 6 the slowest.

By post-processing the cylinder pressure, the indicated mean effective pressure could be calculated, Figure 35. The chart shows sloppy behavior and it displayed high values (relative to this engine) between 15500 and 16500 [rpm] probably because the engine was tuned for achieving good performance in this range.
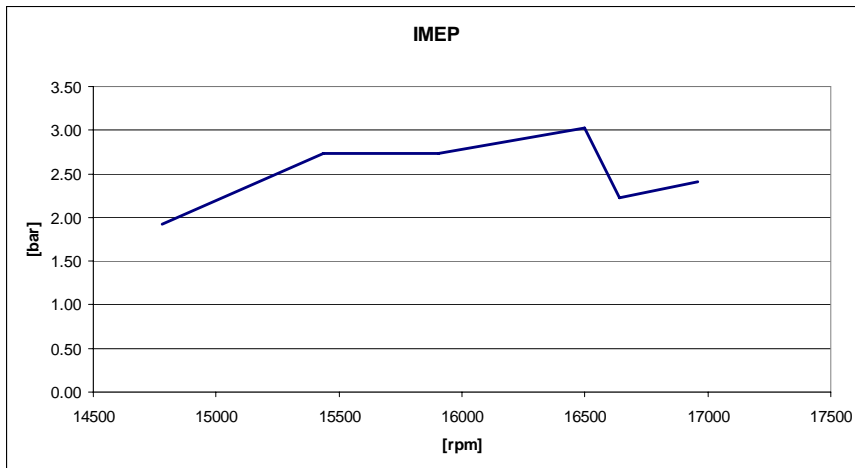
Figure 35: IMEP engine characteristic.

In order to replace the electrochemical batteries, as stated in the introduction, the VIMPA device should have an overall efficiency of at least 3.5%. Apparently this target did not seem to be unrealistic with a *normal* sized engine but unfortunately the combustion in a small volume at high engine speed presents some aspects that substantially lower the overall efficiency of the combustion process. Figure 36 shows the indicated efficiency for this glow plug model airplane engine. Its values were far below the ones expected and it should also be kept in mind that the overall efficiency was lower still because of the mechanical losses. Several reasons were the source of this unpleasant situation:

- Short circuiting of the fresh charge.
- Gap between the piston and liner, there were no piston rings.
- Crevice volumes in the inlet and exhaust ports.
- Quenching phenomena, which assumed a higher importance when the size of the engine decreased.
- High percentage of the boundary layer volume, further explanations will be given in the section *Optical Measurements*.
- Absorption of ethanol in the lubricant film.
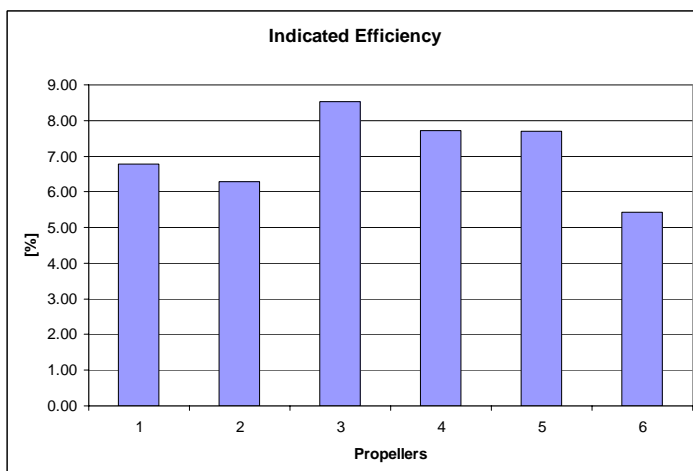
Figure 36: The indicated efficiency between 14500 and 17500 [rpm]. Propeller 1 is the fastest and propeller 6 the slowest.

In Figure 37 the rate of heat release is presented. This chart is shown in order to highlight the double stage combustion. Most of the total heat is released a few CAD after TDC. During the expansion stroke, the fuel that was present in the lubricant film and in the crevices was sucked into the bulk volume. Since the temperature was high enough, part of the fuel was involved in a second stage combustion that ended when the exhaust port opened [34]. This incomplete post-oxidation was the source of unburned or partially burned hydrocarbons, as well as carbon monoxide.
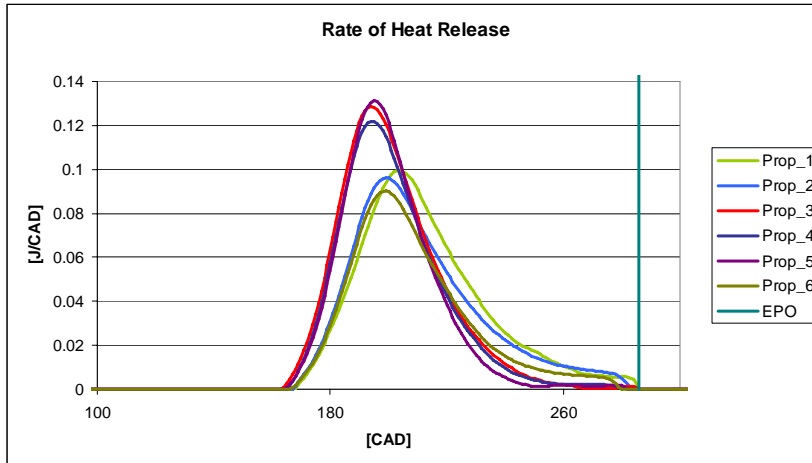
Figure 37: The rate of heat release computed between 14500 and 17500 [rpm]. Propeller 1 is the fastest and propeller 6 the slowest.

Emissions are an important issue when a mini high frequency engine has to be used for hand and not hand held applications in order to avoid intoxication or severe hazards for the users. The emission of HC, CO and NO_x were measured and are presented in Figure 38 in terms of specific emissions. The CO emission was not reported because the amount of carbon monoxide in the exhaust pipe exceeded the limit of the CO analyzer. This instrument only had a range between 0 and 5%. It was however believed that the CO concentration was below 10% according to the amounts emitted when the HCCI engine was tested, cf. Paper 3. The reasons for the very high HC values were:

- Quenching on the walls and of the bulk gases at the exhaust port opening.
- Oil absorption.
- Boundary layer.
- Crevices.

Unfortunately, it was impossible to quantify the relative importance of each parameter. Because of the incompleteness of the reactions during the exhaust stroke and the high percentage of boundary layer, the carbon monoxide concentration was estimated between of 5 – 10%. The values of NO_x were also high. In a mini high speed HCCI engine it was seen that the NO_x production was not only due to the Zeldovich mechanism but also to the Prompt mechanism [33]. In this case, it is not unreasonable to think that the reasons were similar mainly considering that:

1. Because of the high speed of the engine, the mixture was not subjected to high temperatures for long periods of time.

2. When the fuel entered into the combustion chamber it was not perfectly vaporized (see the decrease in temperature in Figure A1-1) and consequently the outer layer of the fuel drops burned. Reactions thus occurred in the fuel-rich flame front ➜ Prompt mechanism.
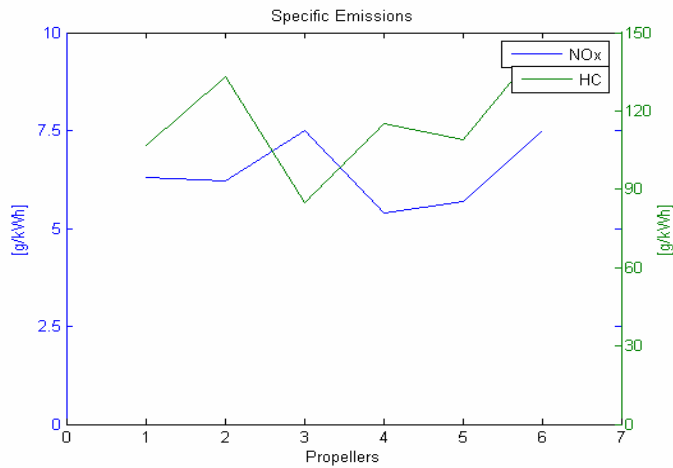
Figure 38: HC and NO$_x$ specific emissions computed between 14500 and 17500 [rpm]. Propeller 1 is the fastest and propeller 6 the slowest.

10.3 Influence of retained burned gases and preheated inlet air

Because of the very high specific emissions, investigations were performed to find out whether retaining more residual gases (by throttling the exhaust and thus increasing the backpressure) and heating up the inlet mixture would be a benefit. The engine was tested with the propeller that gave the best performance in the previous section (i.e. Propeller 3). It was impossible to keep the same speed during the three sets of measurements since the propeller was identical but the amount of fuel injected in each cycle was lower due to the modifications of the engine. The original idea was to test these modifications using the previous blend of ethanol and lubricant as fuel. Since the airflow was lower, the needle of the carburetor was almost in its inner position resulting in an irregular fuel flow and an unstable behavior of the engine. For this reason, the fuel was switched to a blend of 75.6% methanol, 14.4% lubricant and 10% nitromethane, which is the standard fuel for model airplane engines.

The test conditions for the three sets of measurements were the following:

1. Tin = 298 [K], Pex = 1.02 [bar], N = 13035 [rpm].

2. Tin = 298 [K], Pex = 1.15 [bar], N = 10225 [rpm].

3. Tin = 431 [K], Pex = 1.12 [bar], N = 9333 [rpm].

The reduction of specific emissions was significant especially when going from Test 1 to Test 2. Unfortunately, since less fuel was injected in each cycle both because part of the combustion volume was occupied by the retained burned gases and because of the decrease in inlet mixture density as a result of the increase in inlet temperature,

the performance was lower. It was thus suggested that since the emission values remained high and the use of a catalytic converter was an important issue, the best design criteria for the VIMPA engine would be to avoid the use of both a preheated inlet mixture and throttle in the exhaust in order to maximize the power density of the device. An after-treatment system can be placed in the exhaust in order to reduce the emissions.
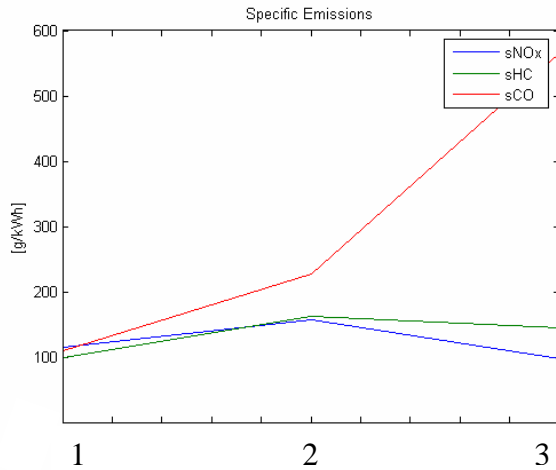
Figure 39: The variation of the specific emissions during the three tests.
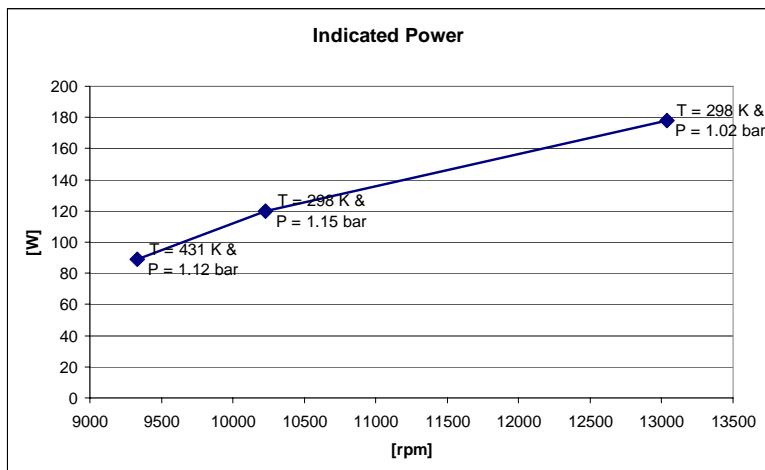
Figure 40: The variation of indicated power during the three tests.

The indicated efficiency was computed for the three cases and is shown in Figure 41. It was found that heating the inlet mixture and increasing the retained burned gases did not improve this parameter. When increasing the backpressure, the efficiency decreased, probably because the combustion phasing was less suitable and the pumping work was higher. On the other hand, when increasing the inlet temperature there was a slight increment of this parameter which was likely caused by a better fuel combustion efficiency.
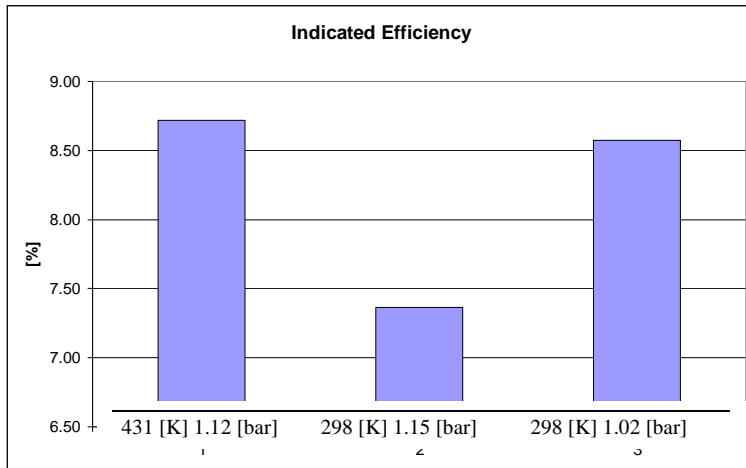
Figure 41: The variation of the indicated efficiency during the three tests.

10.4 Optical diagnostic

10.4.1 Combustion structure

Optical diagnostic was a key factor for clarifying the ignition, evolution and main features of glow plug combustion in a small volume. The knowledge of these parameters was important in order to lower the emission values and increase the work per cycle.

Optical diagnostic analyses were performed at both 9600 and 13400 [rpm]; the speed was changed by using two different propellers. The total chemiluminescence light was acquired together with that of formaldehyde and hydroxyl, believed to represent low and high temperature reactions, respectively. In order to achieve a full view of the combustion chamber, the glow plug and the pressure sensor were mounted on the liner, Figure 29. It was deemed very probable that the new location of the trigger element (-40 TDC) changed some combustion features, for instance the phasing, but it is important to keep in mind that the objective was to understand the ignition and evolution of the combustion rather than to characterize one specific operating point of the engine. The fuel was a blend of 65% methanol, 20% nitromethane and 15% lubricant. Figure 42 shows the total chemiluminescence light from one typical cycle at 9600 [rpm].

Figure 42: The total chemiluminescence light in a single cycle at 9600 [rpm].

The analysis of the cycles demonstrated that at low speed there were two possible ways to start the combustion:

1. Autoignition of the mixture in the warm/hot part of the combustion volume.
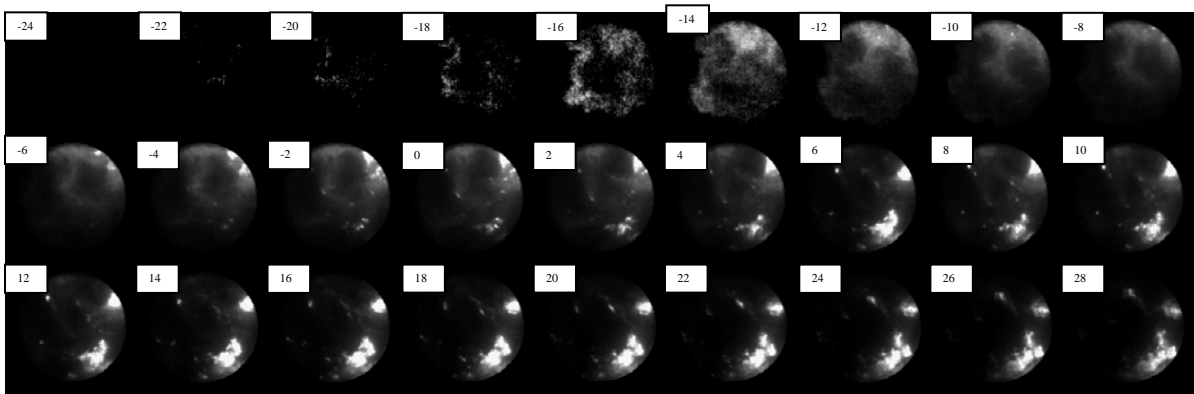2. Ignition of the air/fuel mixture on the glow plug orifice.

Figure 43a shows the first ignition mode while 43b displays the second one. Both figures suggest that a glow plug engine resembles to a compression ignition engine and that the combustion starts as a result of the compression energy and the heat coming from the hot platinum wire of the glow plug. Despite the triggering mode, once some mixture droplets were ignited, the reactions proceeded by *propagating autoignition*. Proof of this statement was the average propagating speed, i.e. 104 [m/s], which was much higher than a turbulent flame speed. One of the first conclusions that could be drawn was that these mini model airplane engines showed

a higher resemblance to HCCI engines rather that SI or CI ones. Their combustion mode can thus be denoted GACI: Glow plug Assisted Compression Ignition.
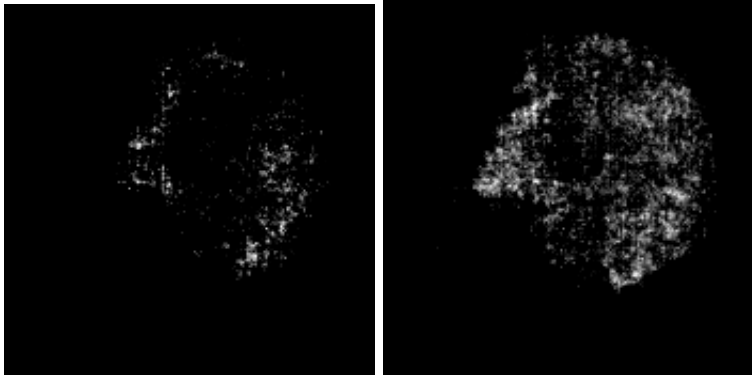
Figure 43a: Start of the combustion with mode 1.
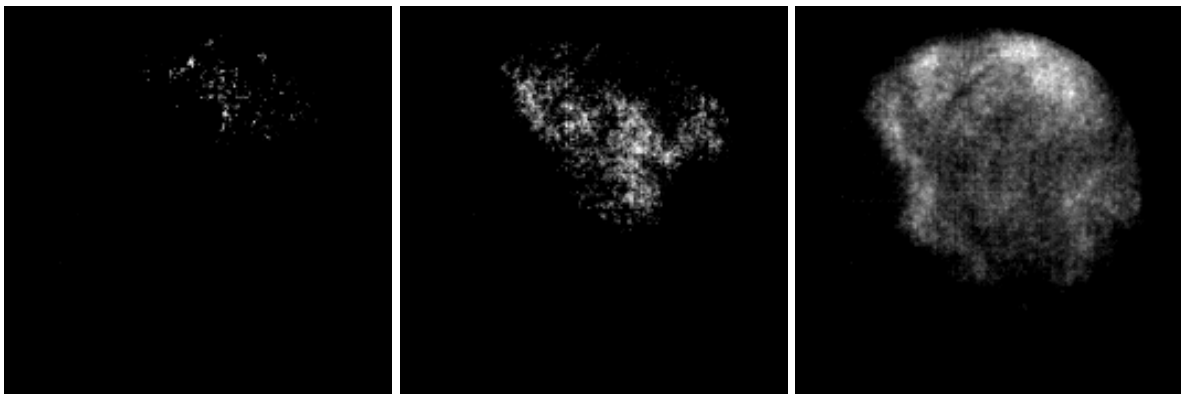
Figure 43b: Start of the combustion with mode 2.

Once the combustion was started, the reactions propagated in a non-uniform manner throughout the combustion chamber. This was a result of the temperature gradient originating from the presence of the exhaust pipe, glow plug and the airflow coming from the propeller. The low level of turbulence was the source of poor mixing between the fuel and the air, thus resulting in fuel stratification that led to soot formation in the last stages of the combustion. The combustion terminated on the cylinder walls since the fuel that was stuck there was pulled away and started to react with the remaining oxygen. These three features are shown in Figure 44.
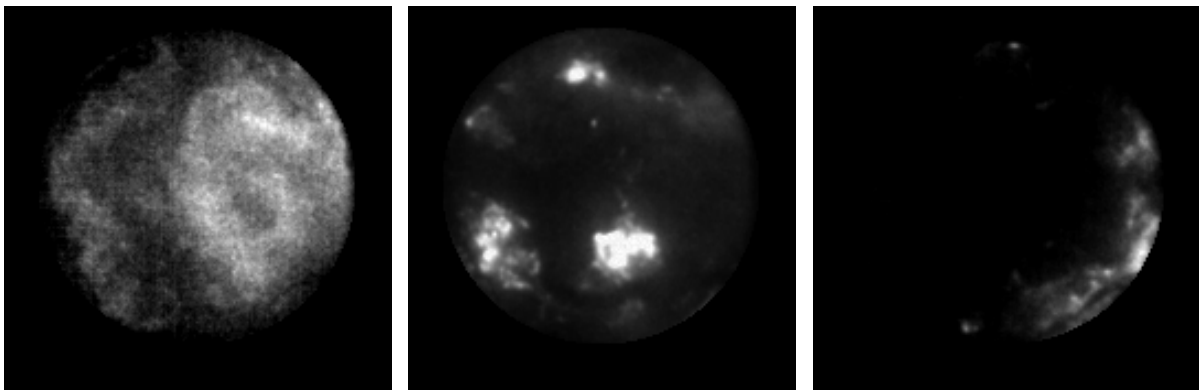
Figure 44: Reaction distribution, soot formation and the last stage of the combustion at 9600 [rpm].

Figure 45 shows the variation of the combustion features at 9600 [rpm] at -10 degrees after TDC. Even though there was a significant variation in combustion structure, the COV of the indicated mean effective pressure was only 5.2%.
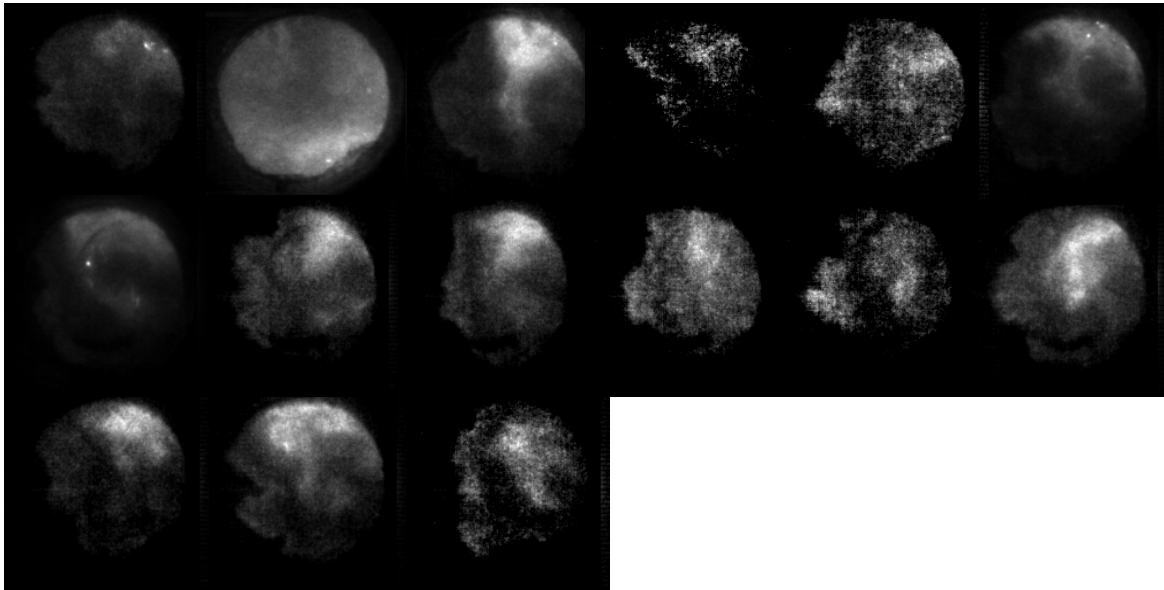
Figure 45: Combustion feature variations at -10 degrees after TDC, 9600 [rpm].

Figure 46 displays the total chemiluminescence light in a single cycle at 13400 [rpm].
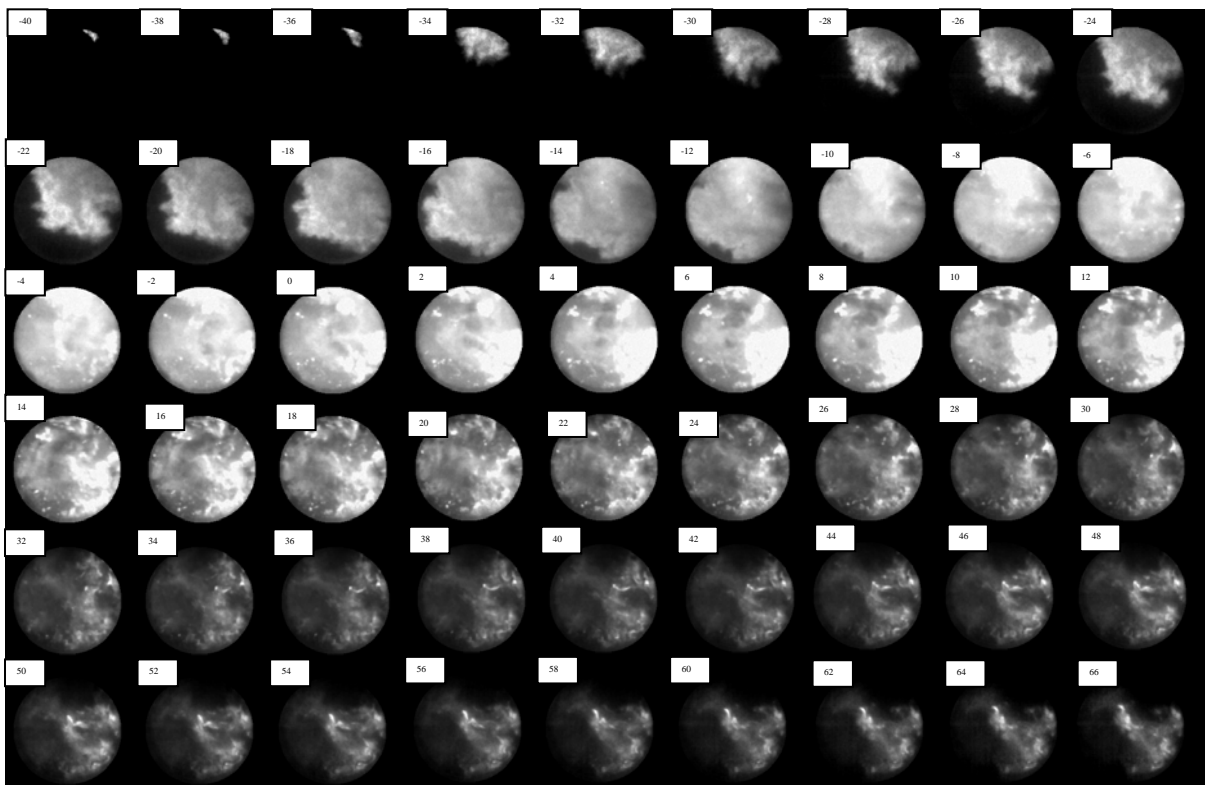
Figure 46: The total chemiluminescence light in a single cycle at 13400 [rpm].

The analysis of the cycles at higher speed demonstrated that, in this case, there was only one combustion mode. The reactions started on the glow plug surface for two

main reasons: the lower heat losses rendered the platinum wire hotter, plus there was not very much time for the reactions to start elsewhere. The propagation speed was computed and its average value was 86 [m/s]. In the second image of Figure 47, it is possible to see where the reactions take place. The thickness of this reaction area was on the order of 3 – 4 [mm] which was considered as further evidence that glow plug combustion was far from being a flame propagation phenomenon.
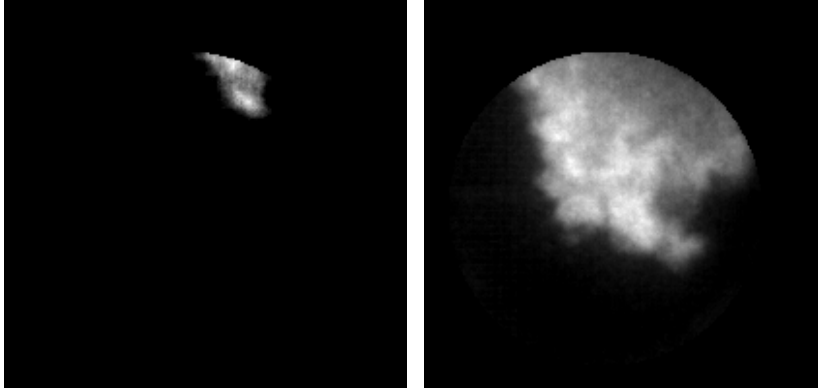
Figure 47: The start of the combustion at 13400 [rpm].

Figure 48 shows typical combustion features at 13400 [rpm]. Because of the better air/fuel mixing caused by the higher level of turbulence and as a result of the lower temperature stratification due to a reduction of the heat transfer, the reactions were homogeneously distributed throughout the combustion volume. This led to a lower combustion structure variation and a better fuel conversion efficiency (from 2.23 to 3.54 [bar] of IMEP). The improved mixing also gave rise to smaller soot particles and less fuel stuck to the cylinder walls (in this case, the reactions terminated in the center of the combustion volume).
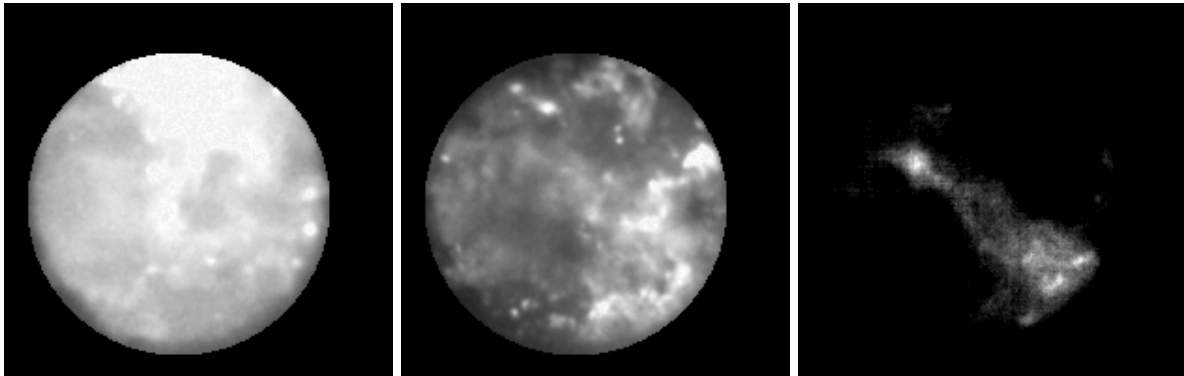
Figure 48: Reaction distribution, soot formation and the last stage of the combustion at 13400 [rpm].

10.4.2 Boundary layer

As described in the *Boundary layer* section (Page 32), the distance between 1- 85% of the maximum differential light intensity was used for computing the thickness of this layer at 9600 and 13400 [rpm]. Values of respectively 0.75 and 0.69 [mm] were obtained. Compared with literature [34, 37], these values were smaller, as the boundary layer thickness normally lies between 1 and 3 [mm]. The analysis of these

values showed that when the piston was at TDC, the boundary layer in the radial direction was approximately 13% while it was very close to 100% in the axial direction. This situation had a non-negligible impact on the emission levels since the intermediate products of the chemical reactions did not become fully oxidized. This can explain the very high amount of unburned and partially burned hydrocarbon, and the out-of-range level of carbon monoxide.
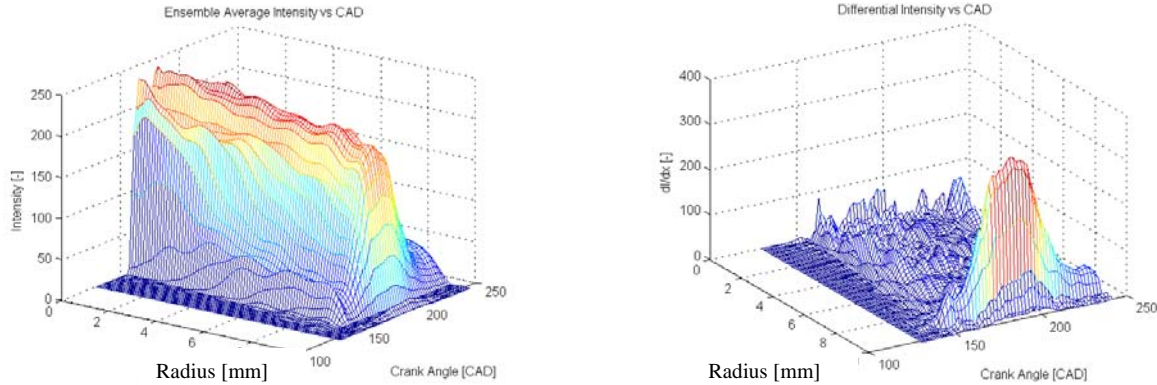
Figure 49: Ensemble average light and differential light intensities as functions of the radius and crank angle at 13400 [rpm].

10.4.3 Rate of heat release versus total chemiluminescence light

It is commonly accepted that CH, OH, C_2 chemiluminescence and naturally emitted light are proportional to the heat release in a flame. This statement is based on two observations [37]:

- The total emission intensity is proportional to the fuel rate in a laminar to a faintly turbulent premixed jet flame.

- The radicals are confined to a relatively thin region of the primary flame surface so that the total chemiluminescence might be thought proportional to the primary flame area and hence to the reaction rate.

In Figure 50, the rate of heat release has been plotted as a function of the crank angle together with the natural emitted light. This was done for a single cycle in order not to lose information due to the averaging process. The chart shows a good agreement in the first part and similarities in shape in the second. The disagreement in the second part was due to the soot formation in the later stages of the combustion. The soot fragments were glow particles and the emitted light was not directly proportional to the energy that they released.
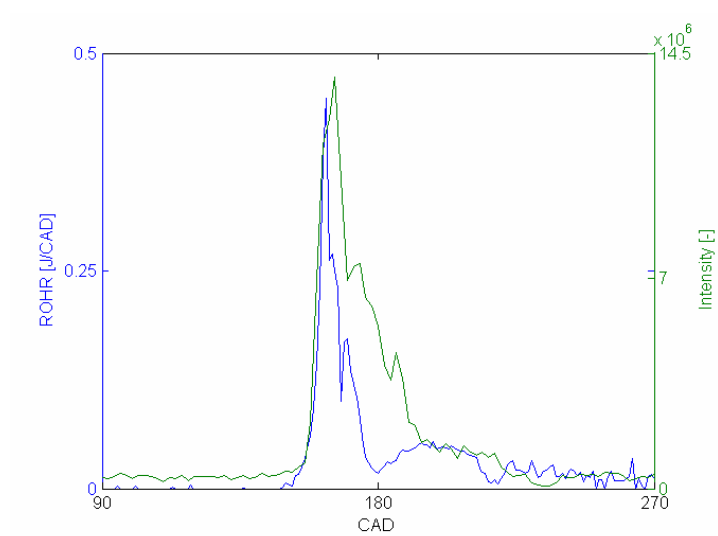
Figure 50: Rate of heat release and light intensity as functions of the crank angle.

10.4.5 Radicals formation and evolution

In Figure 51, the main stages of CH life during one cycle are presented. The reactions started next to the glow plug surface, and then propagated until almost the entire combustion chamber was involved in LTR. These low temperature reactions ended by fading uniformly all over the combustion volume. When a flame propagates, the CH radical is confined within the thin reaction zone, and the fact that, in this case, formaldehydes were distributed all over the chamber was further proof that this combustion process was very close to HCCI combustion.
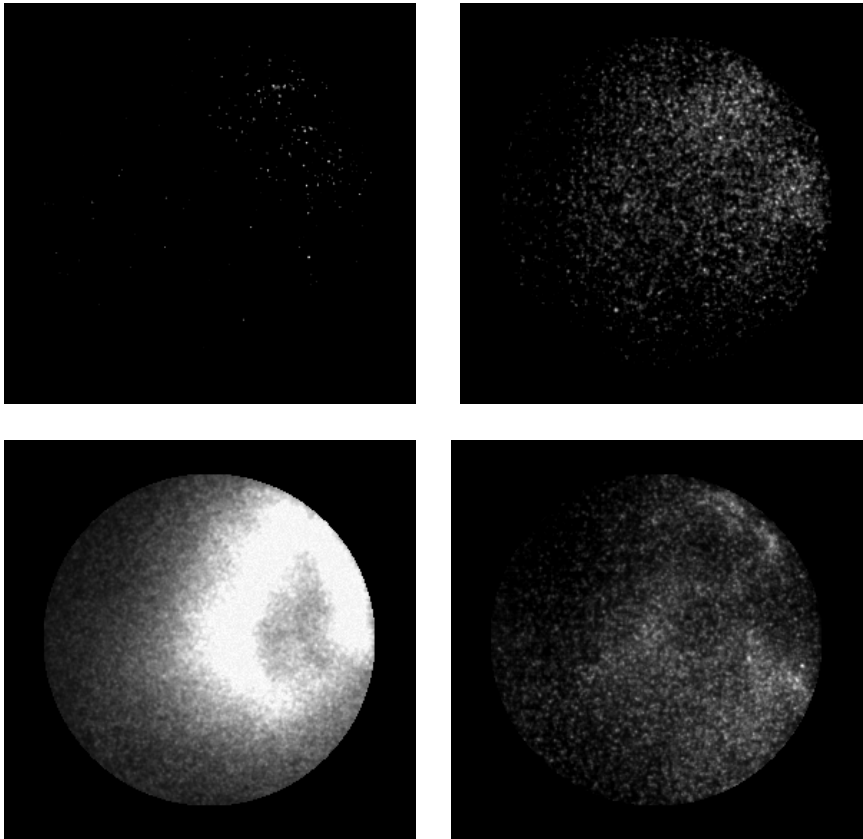
Figure 51: Formaldehyde formation and evolution at 9600 [rpm].

In Figure 52, the *life* of OH radical is shown. The evolution features of the HTR were very similar to the LTR: they started next to the glow plug, propagated and became almost homogeneously distributed in the combustion chamber. The last image does not show how OH radicals terminate, but rather displays soot particles. It has been seen that when an OH filter is applied, it is possible to visualize both high temperature reactions and soot particles. In order to understand what is what, the images have to be analyzed together with the heat release traces [40]. Once again, the fact that the reactions were spread out and not confined to a tiny area indicated that a propagating autoignition combustion took place.
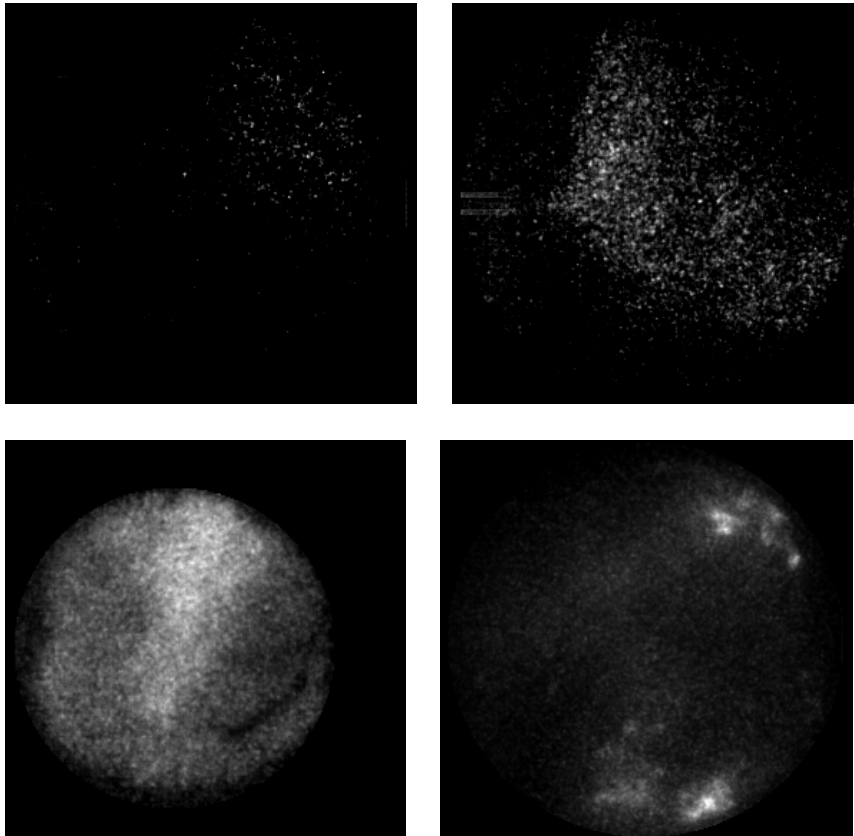
Figure 52: Hydroxyl formation and evolution at 9600 [rpm].

In Figure 53 the evolution of radicals is plotted as a function of the crank angle together with the rate of heat release. A CH – OH sequence can be seen as was also observed in ATAC and HCCI combustion [14, 41, 42]. In SI combustion, formaldehyde and hydroxyl radicals normally appear simultaneously in the reaction area.

Looking at diagram 53 it can be observed that almost 50% of the heat released is caused by LTR. Normally, this value is between 5 and 15%. To explain this phenomenon, the reader has to keep in mind that the percentage of boundary layer is almost 100% in the axial direction and 13% in the radial one (when the piston is at TDC). This means that most of the energy release originates from incomplete combustion reactions when the fuel molecules react into intermediate products. This can also explain the high level of carbon monoxide.
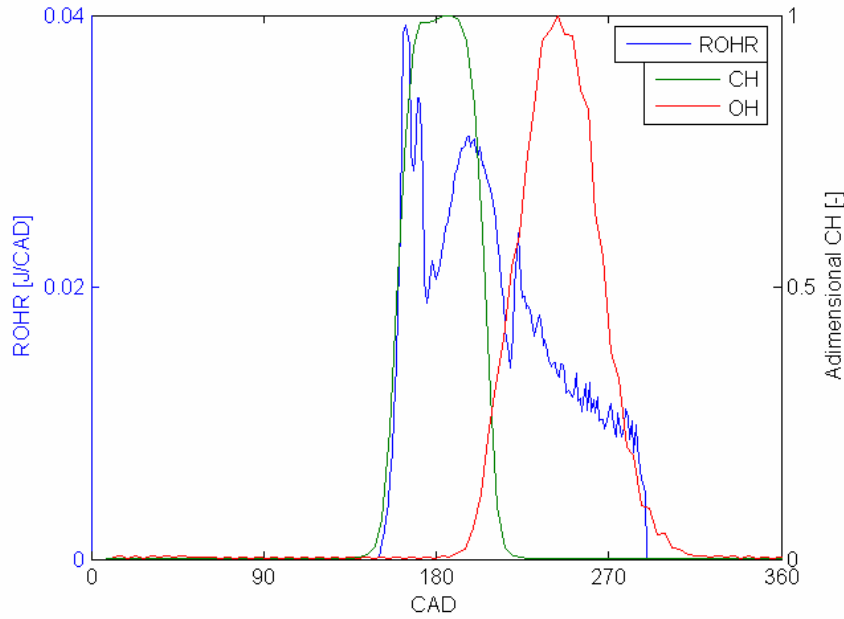
Figure 53: CH and OH radicals as functions of the crank angle plotted together with the rate of heat release at 9600 [rpm].

At 13400 [rpm], the features of the radical evolutions were rather similar to the low speed case; only two exceptions were noted. The first regarding CH; at the higher speed, the reactions were not distributed over the entire combustion chamber but were present only at the exhaust port after the initial propagation. This was probably due to fuel stratification resulting from the crevice and flow motion. The second observation concerned OH. At the higher speed, no soot particles were visualized and this was believed to be the result of an improved fuel/air distribution in the bulk volume.
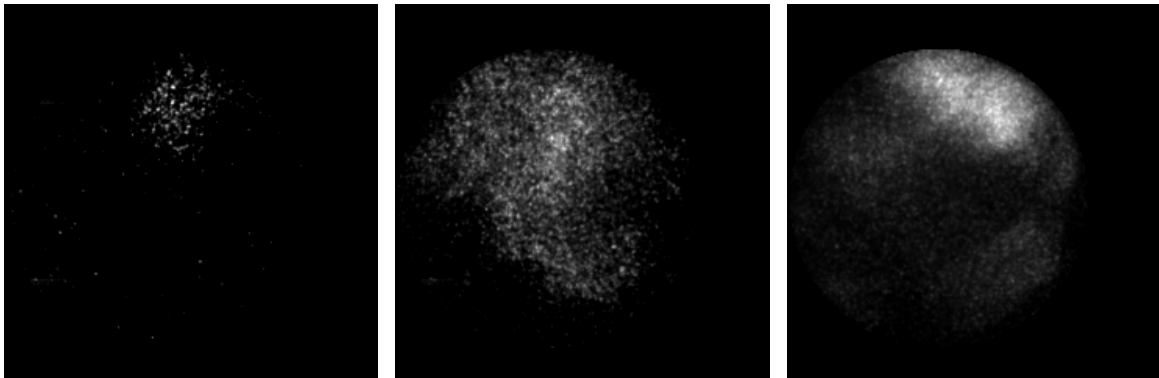
Figure 54: Formaldehyde formation and evolution at 13400 [rpm].

59

Figure 55: Hydroxyl formation and evolution at 13400 [rpm].

Figure 55 displays the radical evolutions, and, as can be seen, the CH – OH sequence was again present. Because of the lower heat losses due to the higher speed, HTR showed up earlier and were present at the same time as the LTR, but of course not in the same place. At higher speed, most of the heat was released by high temperature reactions, indicating that there were more reactions leading to CO_2 and H_2O. Because of this: IMEP was 1.59 times higher than in the low speed case.

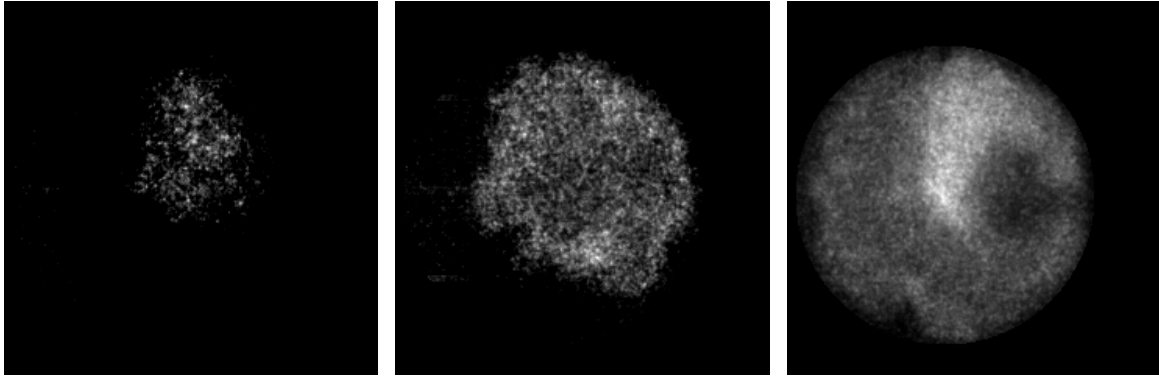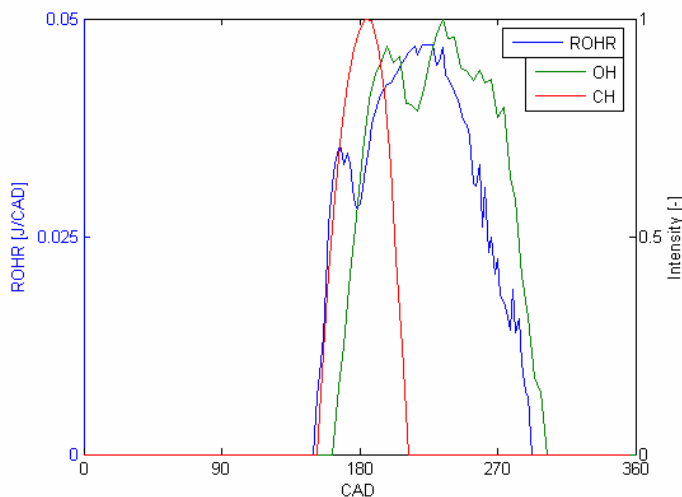**Figure 56: CH and OH radicals as functions of the crank angle plotted together with the rate of heat release at 13400 [rpm].**

11. Results: HCCI Engine

11.1 Introduction

The original idea of VIMPA was to use ethanol as fuel since it is environmentally friendly and only costs around 1 $ per gallon. Various attempts were thus carried out to achieve HCCI combustion with this fuel by using the modified O.S. 25 as a test engine. Unfortunately, it was observed that in the centi-scale, HCCI combustion with ethanol as fuel was unfeasible and the situation would have been even worse in the milli-scale. Since ethanol has a high autoignition temperature, it was impossible to achieve combustion only by using the compression energy, and consequently a heater was mounted on the inlet. The inlet air was heated up to 483 [K] and after a few minutes of warming up, the combustion started. However, it was extremely violent and resulted in the connecting rod breaking-down and the crankshaft becoming bent. The situation could not be improved even when these two components were fabricated with a higher quality steel or titanium. The idea of using ethanol in VIMPA was thus abandoned since the combustion could not be achieved in the milli-scale, because of structural problems and since the start up required too much time.

The next idea was to adopt a fuel that was still environmentally friendly but also easy to ignite. The choice came to diethyl ether, as it can be obtained from biomass and its autoignition temperature is only 170 [ºC] - sometimes even lower (up to 70-80 [ºC]) - because peroxides can experience self-accelerating (exothermic) decompositions. A reliable HCCI engine was achieved when using this fuel. The start-up needed only a few crank shaft revolutions and the autoignition relied on the energy from the compression.

11.2 Engine characterization

The characterization of the combustion process for the HCCI combustion with diethyl ether, DEE, using a modified O.S. 25 engine, was performed between 7500 and 17500 [rpm]. The load was changed by using six propellers (Table 7) and as in the case of the glow plug combustion, the speed could be considered constant since its coefficient of variation was between 0.2 – 0.4 [%]. Problems with the fuel flow in the injection line were experienced as a result of DEE vaporizing very easily. Thus, in order to improve the carburant flow, the fuel used was a blend of 80% DEE and 20% castor oil.

Table 7: Propeller specifications.

Propeller	Diameter [inch]	Pitch [inch]
1	9.5	9
2	9	8
3	8	8
4	7	8
5	6	5
6	5	4

Figure 57 dispays the indicated mean effective pressure, and a linear increase can be seen between 7500 and 17300 [rpm]. By increasing the speed, the heat losses were lower, thus resulting in a higher wall temperature, a lower temperature gradient in the combustion chamber and hence an enhanced fuel conversion efficiency. A better fuel combustion efficiency, rather than a more appropriate combustion phasing (Figure A2-5), led to higher values of IMEP.

When propeller number 6 was mounted, a linear trend of the IMEP increase was still expected. Strangely, this did not occur and the explanation was attributed to the non linear behavior of the friction losses.

As compared to glow plug combustion, the IMEP was visibly lower. The reason was found in the boundary layer thickness that was twice that of the glow plug case [40]. Increasing the cylinder wall temperature has been found to improve the performance [44]. Even though the amount of retained burned gases was substantial, cf. Figure 59, the combustion was more violent as compared to that in the glow plug case (maximum pressure rise rate, Figures 33 & 58). This is a typical situation with HCCI combustion basically because the mixture burned more or less homogeneously and simultaneously in the combustion chamber.
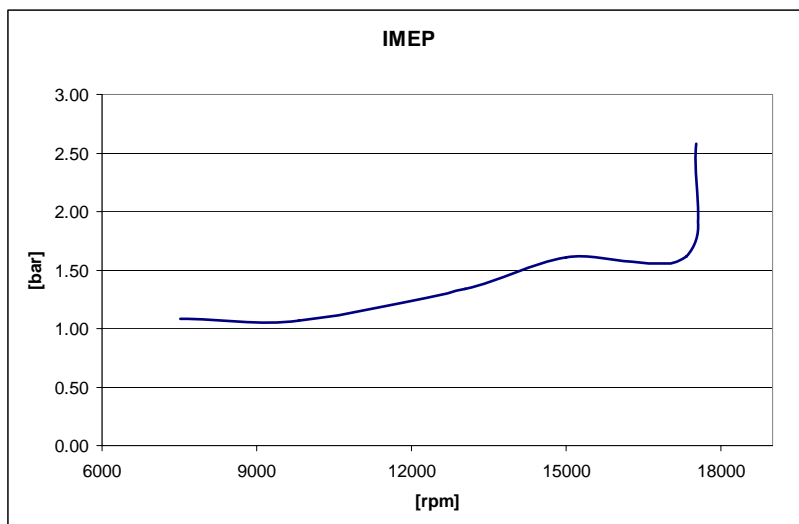
Figure 57: IMEP engine characteristic.
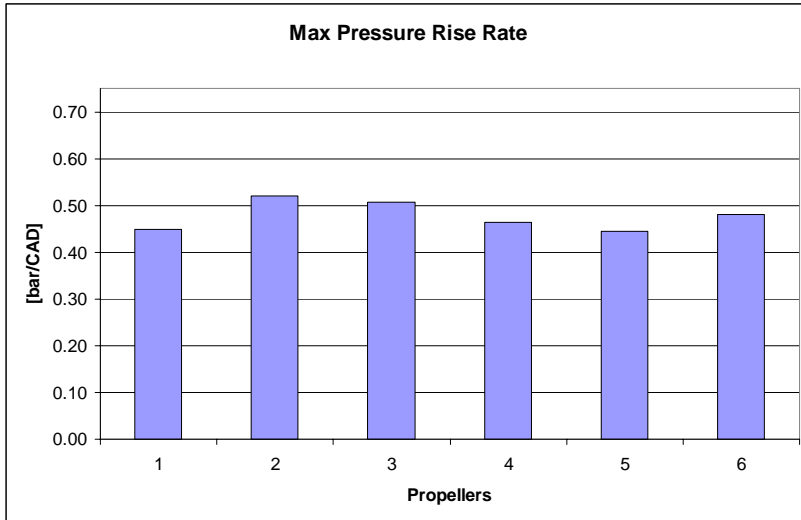
Figure 58: The maximum cylinder pressure rise rate acquired with a HCCI engine between 7500 and 17500 [rpm]. Propeller 1 is the slowest and propeller 6 the fastest.
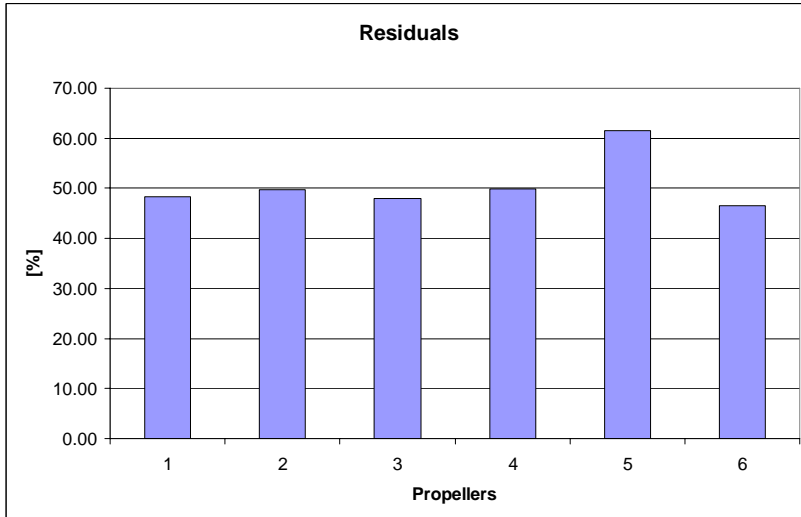
Figure 59: Estimated residual gases during the six tests between 7500 and 17500 [rpm]. Propeller 1 is the slowest and propeller 6 the fastest.

As stated in the introduction, the overall efficiency of the process had to be at least 3.5 [%] in order to replace electrochemical batteries with a mini internal combustion engine. Figure 60 shows the indicated efficiency. As in the case of IMEP, this parameter increased with engine speed because of the improvement of the thermal management. Unfortunately, the target of 3.5% was reached only with propeller 6. The reasons for this setback were the same as those described in the case of GP combustion. In the HCCI case, the efficiency was even lower because of a thicker boundary layer [40]. It will be shown later in the thesis that improving the thermal management can lead to indicated efficiency values higher than 3.5%.
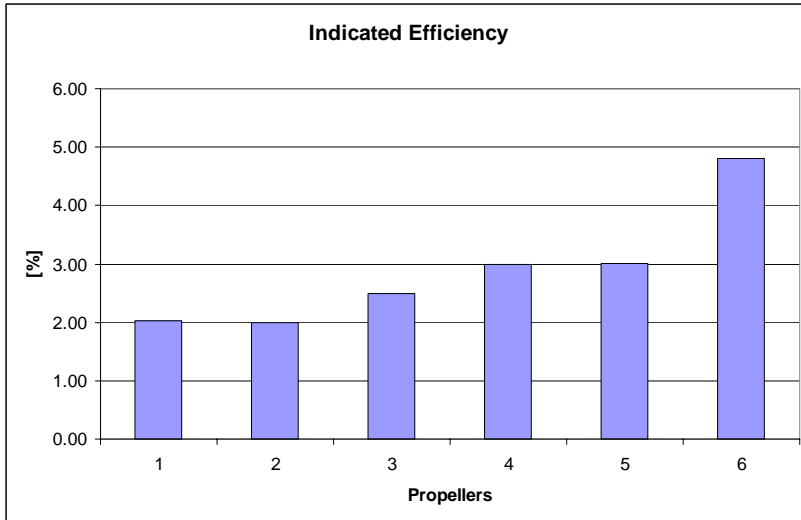
Figure 60: The indicated efficiency between 7500 and 17500 [rpm]. Propeller 1 is the slowest and propeller 6 the fastest.

The rate of heat release is shown in Figure 61. Three stages of the combustion can be seen: LTR followed by HTR and finally post-oxidation reactions. The first two stages are typical with DEE; they are mainly due to chemical bonding rather than the operating conditions. At relatively low speed, Figure 61 a, the HTR started immediately after the LTR without a well defined border, whereas at higher speed (Figure 61 b), the LTR and HTR behaved more like two separate combustion events causing a visible increase in energy release (Total heat release, Figure A2-4). The third combustion stage, i.e. post-oxidation, depended on the running conditions. With a low level of turbulence, a certain amount of the fuel could stick to the liner during the compression and main combustion. In the expansion stroke, the mixture was pulled away from the cylinder walls and reacted partially with the remaining oxygen. This gave rise to a tail in the heat release trace. Improving the degree of homogeneity and thereby getting rid of the third combustion stage, may be beneficial in terms of reduction of partially burned HC and CO since the chemical reactions were not quenched at the EPO.
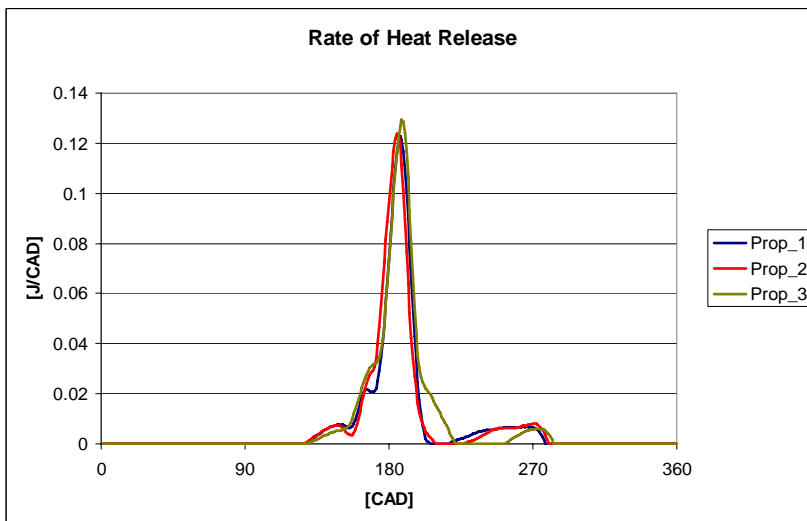
Figure 61 a: ROHR traces for propellers: 1, 2 and 3.
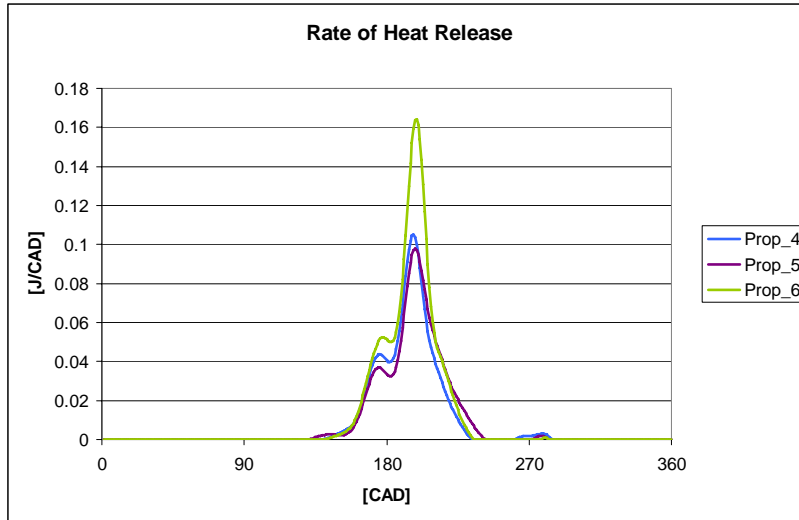
Figure 61 b: ROHR traces for propellers: 4, 5 and 6.

The rate of heat release traces were post-processed and the combustion duration was obtained in the CAD and time domain, Figure 62. When increasing the engine speed, it was found that CD remained fairly constant in the CAD domain whereas it decreased in the time domain. This result was in good agreement with studies performed on normal-sized HCCI engines [43]. The situation originated from the increase in cycle temperature due to the lower heat losses, which led to faster chemical kinetics and hence a shorter combustion duration in the time domain.
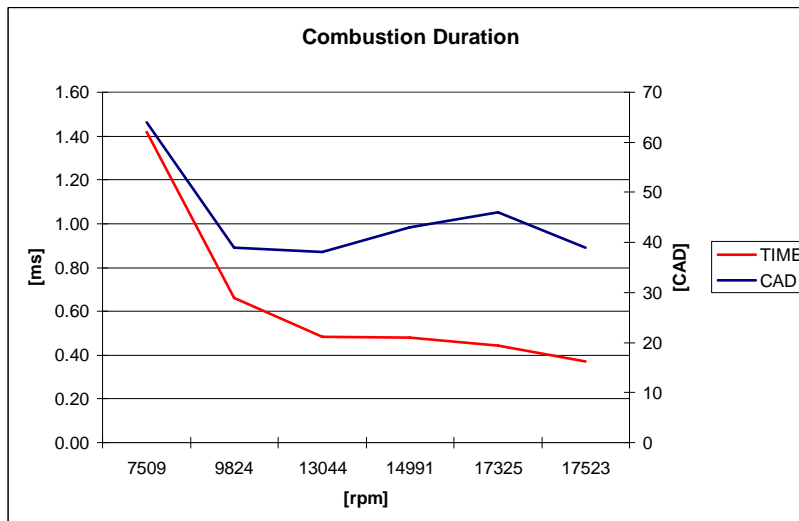
Figure 62: The combustion duration in the time and CAD domains versus engine speed.

Figures 63, 64 and 65 display respectively the specific emissions of HC, CO and NO_x. The reasons behind the high values of HC and CO were the same as those described in the section on glow plug combustion. This time, it was possible to record the CO concentration since a new analyzer with a range from 0 – 10% was used. Concentrations of unburned and partially burned hydrocarbons were higher in the HCCI case for two reasons:

65

- The oil absorption phenomenon was emphasized since the fuel blend contained 20% of castor oil.
- The boundary layer was thicker.

NO_x emissions were lower than in GP combustion because of the lower in-cylinder temperature in the HCCI engine, Figures A1-1 and A2-1. The measured NO_x was plotted versus the maximum cylinder temperature together with the values predicted by the Zeldovich mechanism, and the result can be seen in Figure 66. There were no similarities between the two lines suggesting that the NO_x formation mechanism in this small engine was not only due to the Zeldovich mechanism but also to the Prompt mechanism.
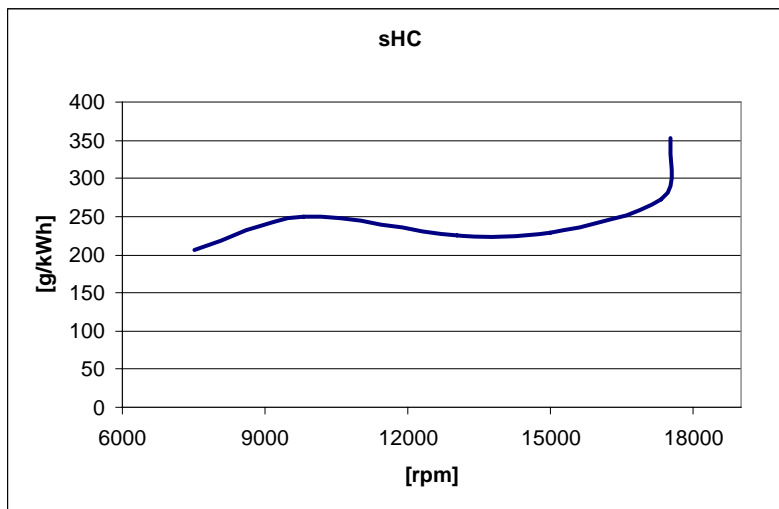
Figure 63: Specific hydrocarbon emissions versus engine speed.
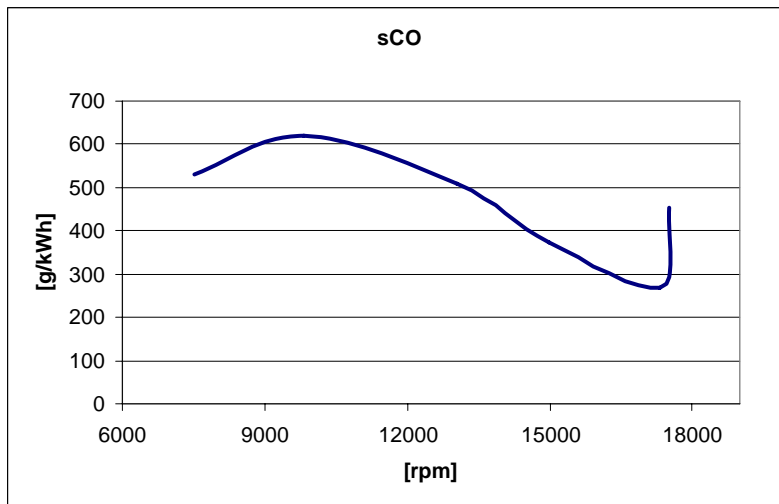
Figure 64: Specific carbon monoxide emissions versus engine speed.
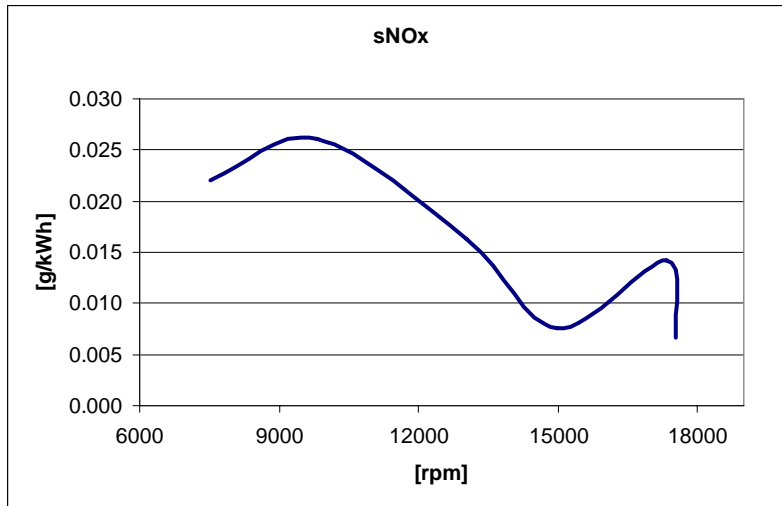
Figure 65: Specific NO$_x$ emissions versus engine speed.
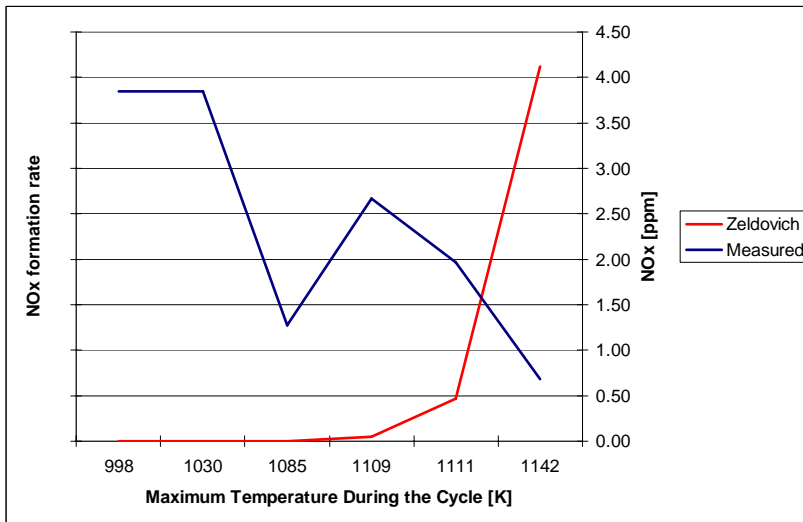
Figure 66: A comparison of the measured NO$_x$ concentrations with values predicted by the Zeldovich mechanism as a function of the maximum temperature in the cycle.

11.3 Optical diagnostic

11.3.1 Combustion structure

The first step was to achieve HCCI combustion in a small volume. Once this goal was achieved and a full characterization of the metal engine was carried out, optical diagnostic was used in order to understand the evolution of HCCI combustion in a small volume at a high engine speed. The analysis was carried out by acquiring naturally emitted light, formaldehyde, hydroxyl and C_2. The light emitted from this last radical was recorded since the radical was thought to be both the precursor of soot as well as of the reactions that lead to CO and CO_2. The measurements were performed at two speeds, 6500 and 14000 [rpm]. The speed was changed by using propellers number 1 and 4, Table 7. The fuel was once again a blend of 80% DEE and 20% castor oil. The compression ration was equal to the one of the *metal* engine thus allowing a comparison between the two engines. The only variable was represented by the heat transfer coefficient of the cylinder head. The optical access allowed a full view of the combustion chamber seen from above and, as was also the case for the optical diagnostic of the GP engine, the pressure sensor was mounted on the liner.

The total chemiluminescence light for a single cycle is shown in Figure 67. Small reaction islands appeared in the center at -2 degrees after TDC and two crank angles later they were spread all over the combustion chamber. Unfortunately, because of the bad CAD resolution, it was not possible to understand whether there existed a propagation of these reactions or whether other islands of the mixture started to burn. After a homogeneous combustion, an air jet, originated from the pressure sensor channel, entered the combustion chamber at +6 degrees after TDC. From +8 degrees after TDC the reactions occurred more and more on the side of the combustion volume, both because of the quenching from the air jet and because of the fuel stratification on the liner. These features were common to all the cycles and the only dissimilarities were the locations of the first few reaction spots and the flow motion introduced by the air jet.
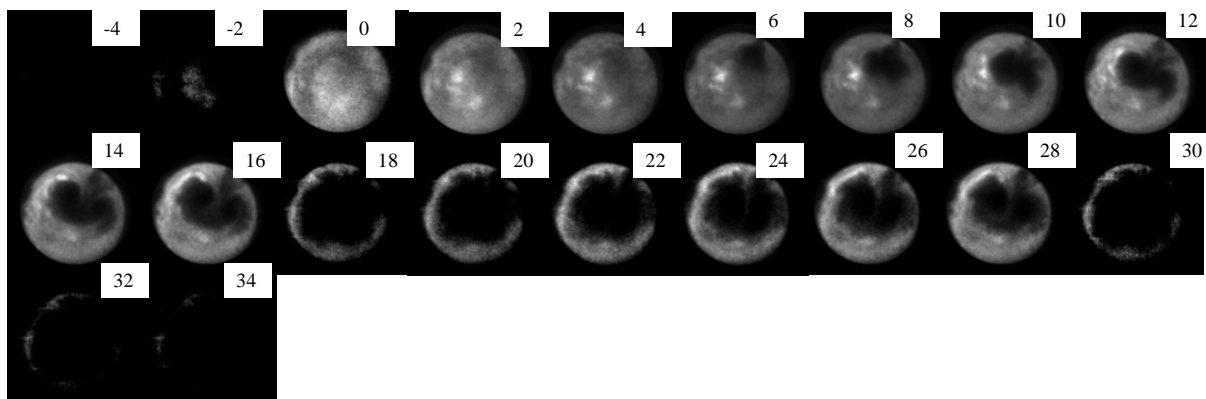
Figure 67: The total chemiluminescence light in a single cycle at 6500 [rpm].

Figure 68 shows the total chemiluminescence light at 14000 [rpm]. Because of the higher speed, the images were acquired every 4th CAD, thus resulting in even less valuable information on the beginning of the HCCI combustion. After analyzing the

pressure trace (Figure A2-6), the ROHR (Figure A2-8) combustion phasing, the combustion duration (Table A2-1) and the chemiluminescence images at low and high speed, it was believed that the evolution of the reactions between -2 and +2 at high speed, was very similar to that at low speed.
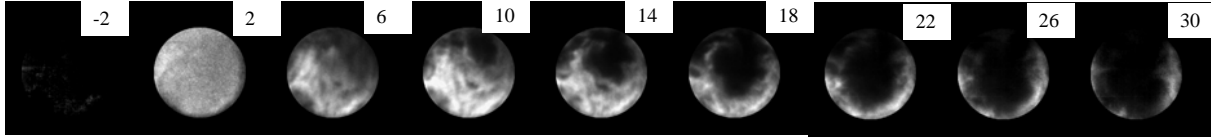
Figure 68: The total chemiluminescence light in a single cycle at 14000 [rpm].

Figures 69 and 70 display the total chemiluminescence light at +3 and +2 degrees after TDC at 6500 and 14000 [rpm], respectively. As compared to GP combustion, the variation of the combustion structure was much lower. The variation was smaller at the higher speed, probably due to less temperature stratification as a result of the lower heat flux.
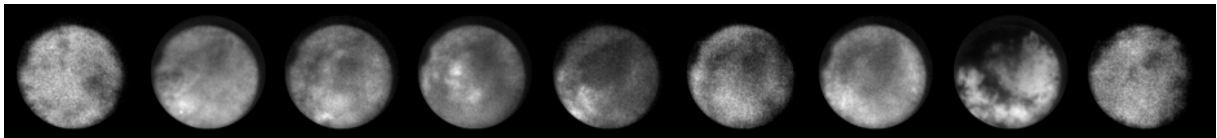
Figure 69: Combustion feature variations at +3 degrees after TDC, 6500 [rpm].
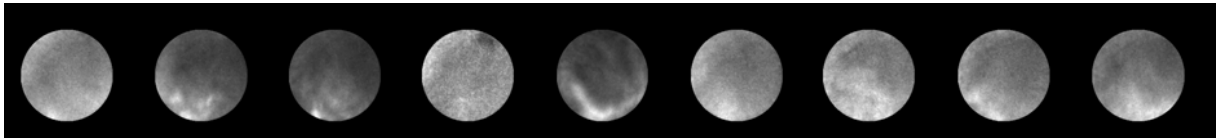
Figure 70: Combustion feature variations at +2 degrees after TDC, 14000 [rpm].

11.3.2 Boundary layer

The boundary layer thickness was computed using the same procedure as in the case of the GP engine, i.e. the distance between 1- 85% of the maximum differential light intensity. It was found that at high speed, its averaged thickness was 0.94 [mm] while at 14000 [rpm] it was 1.45 [mm], i.e. 54% thicker. The increase in thickness with speed was probably due to the fact that there was not enough time for reaching steady state conditions. Compared to literature [34, 37], this thickness was smaller as it normally lies around 3 [mm]. The percentage of boundary layer was computed and for a piston at TDC, it was found to be 100% in the axial direction whereas it was 10.2 and 15.5% respectively at 6500 and 14000 [rpm], in the radial direction. As in the case of the glow plug engine, this situation had a huge impact on the emission levels of HC and CO mainly because the temperature was too low for achieving a complete oxidation of the mixture. Figure 73 shows the variation of the boundary layer thickness during the combustion event. As was stated by Heywood [34], a well-defined trend of this thickness cannot be detected during the course of the combustion.
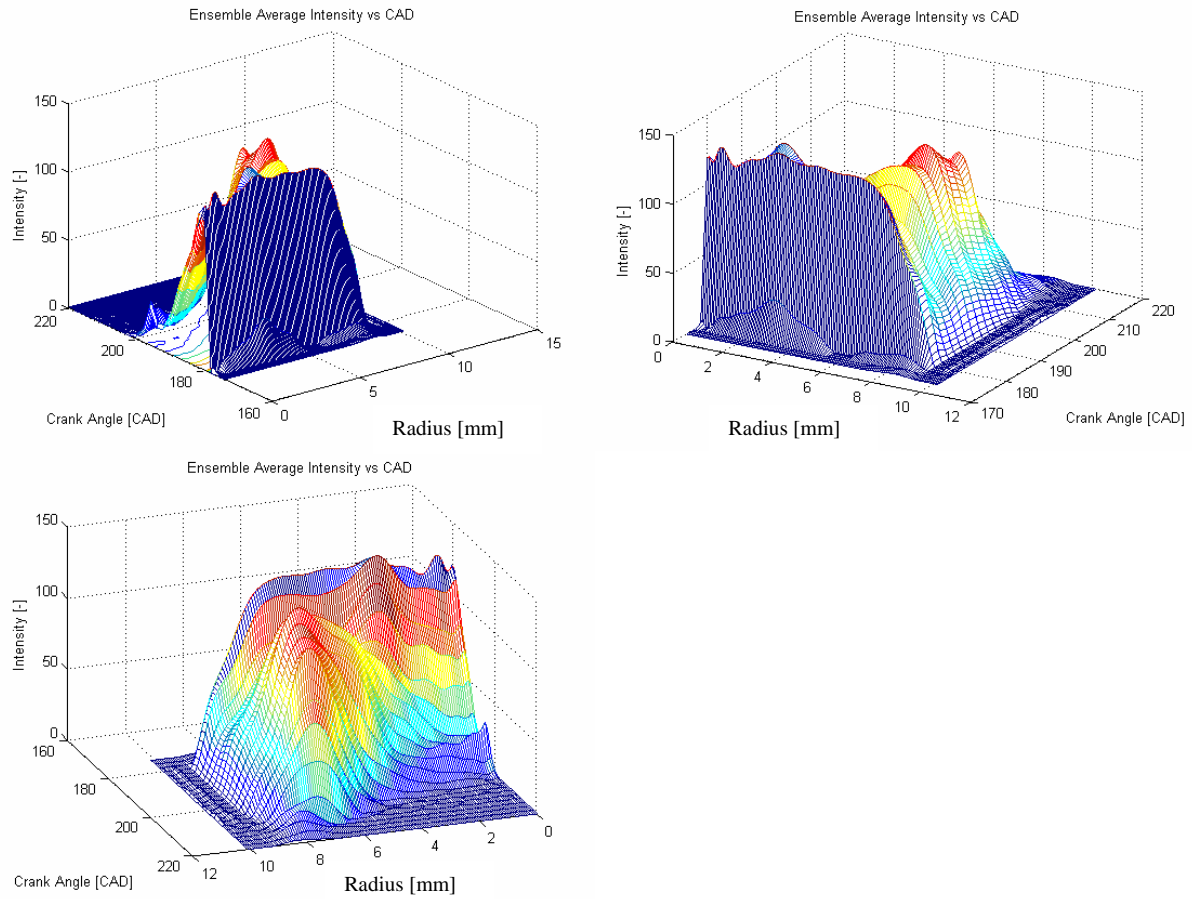
Figure 71: Ensemble average light intensity as a function of the radius and crank angle at 6500 [rpm].
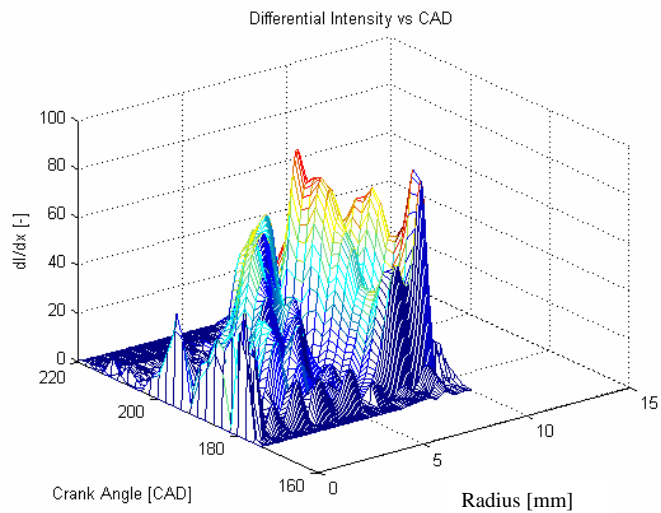
Figure 72: Ensemble average differential light intensity as a function of the radius and crank angle at 6500 [rpm].
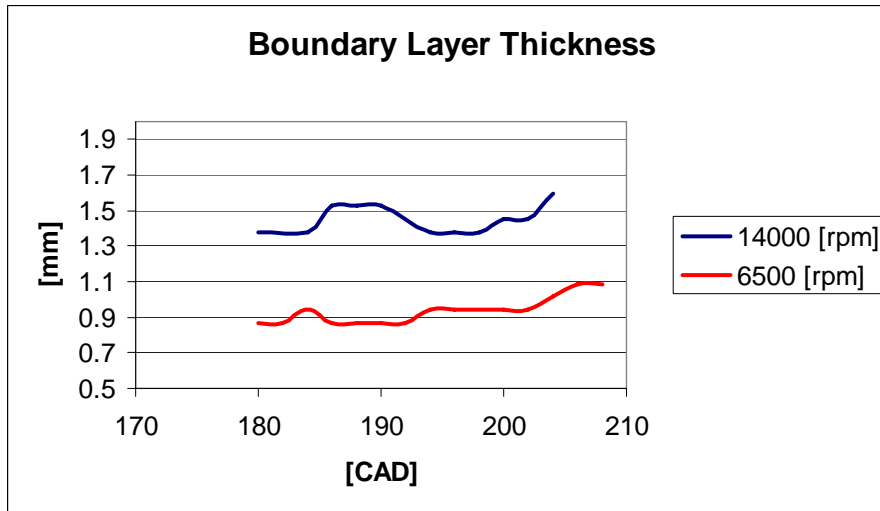
Figure 73: Variation of the boundary layer thickness during the combustion event at 6500 and 14000 [rpm].

11.3.3 Rate of heat release versus total chemiluminescence light

As in the case of the GP engine, the natural emitted light from HCCI combustion is proportional to the heat release in a flame [37]. These two quantities are plotted in Figures 74 and 75 respectively representing the low and high speed cases. Because of the small difference in combustion structure between the cycles, the curves in the figures are averaged values. A good agreement was found in the first part of the two traces both at high and low speed. In the second part, there was a mismatch between the ROHR and the natural emitted light, especially at 6500 [rpm]. The source of this mismatch was the presence of soot particles (Figure 78), since the light emitted from the soot particles was not directly proportional to the energy they released. Because of the higher homogeneity of the mixture there was a lower formation of soot particles, and at 13400 [rpm], the mismatch was lower (Figure 82).
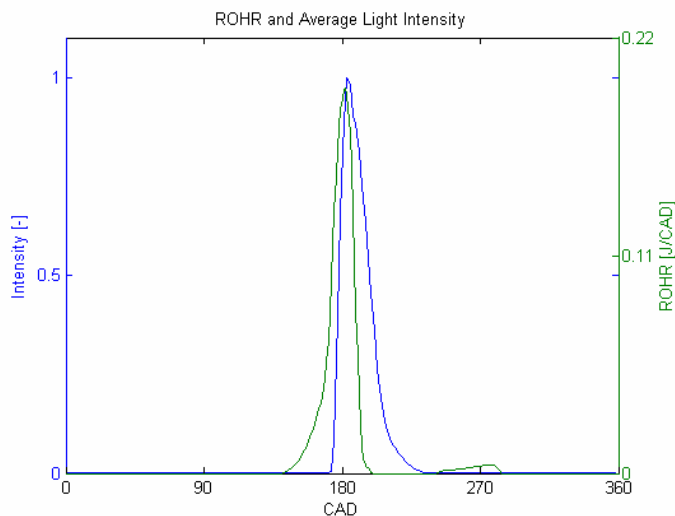
Figure 74: Rate of heat release plotted with the naturally emitted light, 6500 [rpm].

71
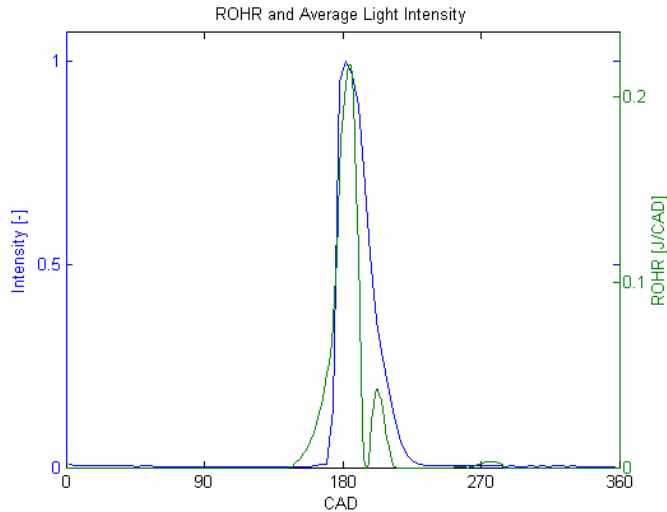
Figure 75: Rate of heat release plotted with the naturally emitted light, 13400 [rpm].

11.3.4 Radicals formation and evolution

Figure 76 shows the low temperature reaction distributions at 6500 [rpm]. Very little valuable information can be extrapolated from these images as a result of a bad CAD resolution and a very low light intensity from the low temperature reactions. Uniformly spread reactions can only be seen at TDC.
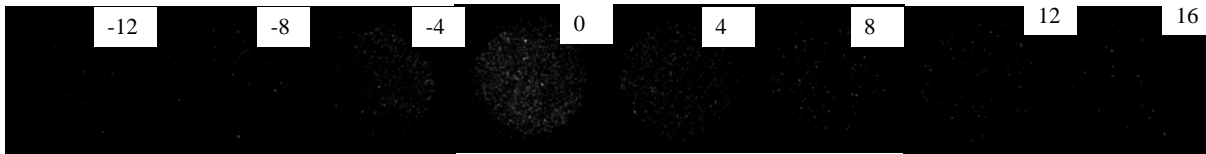
Figure 76: CH light in a single cycle at 6500 [rpm].

Figure 77 displays the OH distribution. A homogenous phase was followed by a heterogeneous one indicating that the last images showed soot and not high temperature reactions. This was also confirmed in the C_2 images in Figure 78.
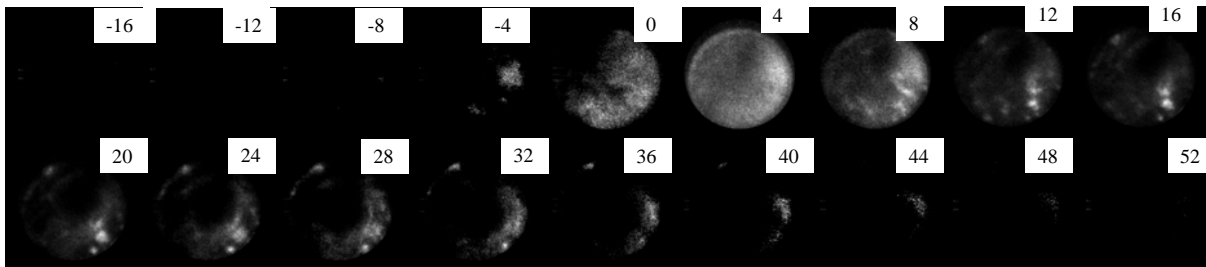
Figure 77: OH light in a single cycle at 6500 [rpm].

Figure 78 displays the C_2 light distribution. C_2 was measured since it was thought to be both the precursor of soot as well as of the reactions that lead to CO and CO_2. The formation of C_2 was unclear; nothing was visible prior to -1 degrees after TDC. A homogeneous light distribution could only be observed at -1 degrees after TDC, where reactions leading to CO and CO_2 could be visualized. From 1 to 31 CAD aTDC,

the images displayed a heterogeneous light distribution indicating that in the second part of the combustion, soot formation occurred due to an uneven distribution of the fuel in the combustion volume. This was exactly as in GP combustion at low speed.
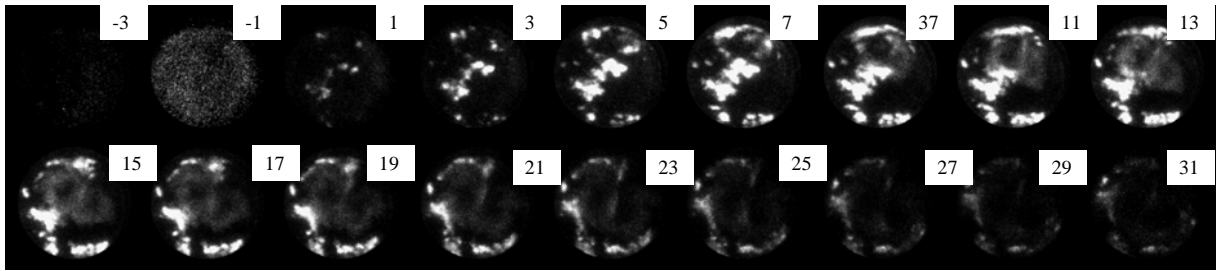
Figure 78: C$_2$ light in a single cycle at 6500 [rpm].

In Figure 79, the radical evolution is presented. In this small high speed HCCI engine, the sequence C$_2$, CH and OH was found, and the same evolution has been observed in normal-sized HCCI engines [13, 14, 41, 42].
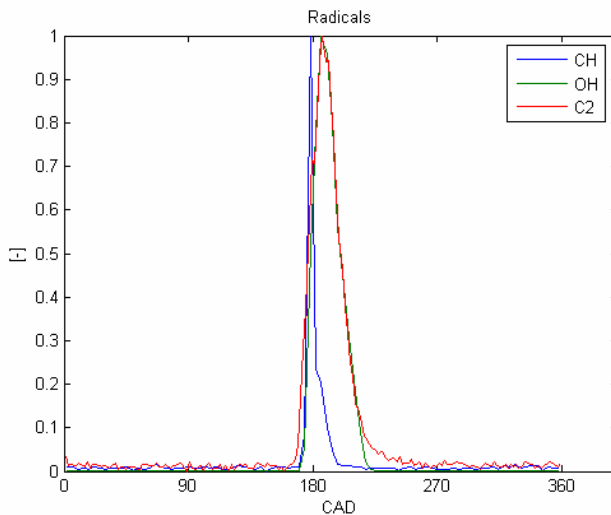
Figure 79: Radical evolution at 6500 [rpm].

Figures 80, 81 and 82 show CH, OH and C$_2$ distributions in a single cycle at 13400 [rpm]. Since formaldehyde was acquired only every 6th CAD and since the light emitted from LTR at high speed was lower than that at 6500 [rpm], there was not much to be said regarding formaldehyde. At 13400 [rpm], the light emitted from C$_2$ and OH was homogeneously distributed which was an indication that only reactions were visualized. This statement was further confirmed in Figure 83 where the match between OH and ROHR was very good. As in the case of glow plug combustion, it was possible to reduce the soot formation and at the same time improve the performance of the engine by increasing the speed and hence enhancing the homogeneity of fuel/air and temperature distributions (Table A2-1).
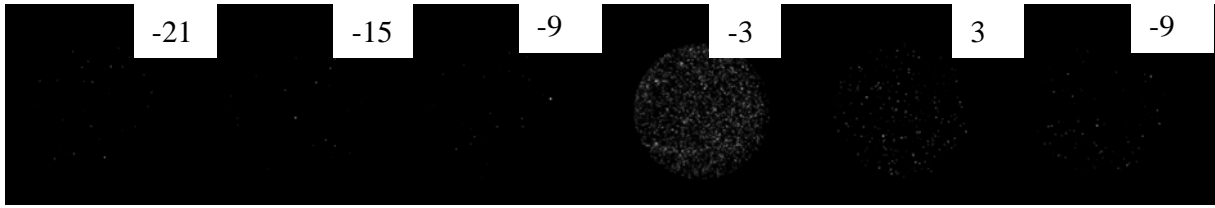
Figure 80: CH light in a single cycle at 13400 [rpm].
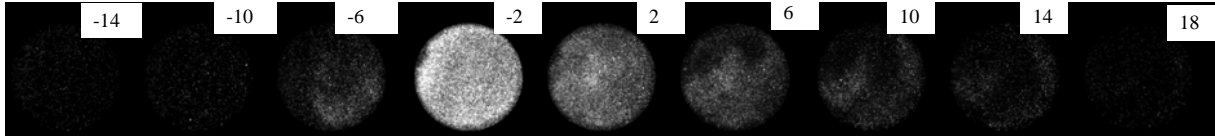
Figure 81: OH light in a single cycle at 13400 [rpm].
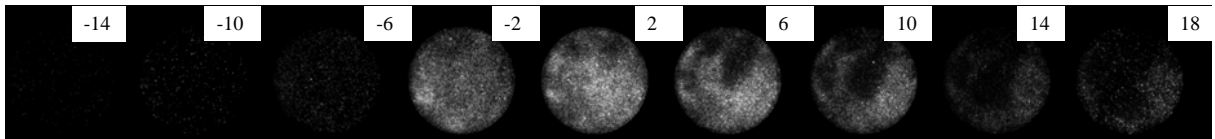
Figure 82: C$_2$ light in a single cycle at 13400 [rpm].
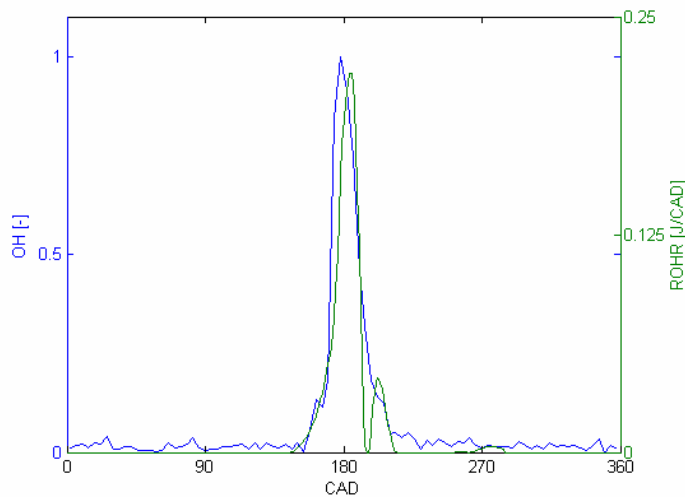
Figure 83: Rate of heat release plotted with hydroxyl light at 13400 [rpm].

At high speed, the radical evolution was the following: OH, C$_2$ and CH. It was very unusual to see the low temperature reactions appear after the high temperature ones. However, it has to be kept in mind that CH was sampled every 6th CAD and that its emitted light was very weak. Hence, the initial moments of LTR evolution have been missed.
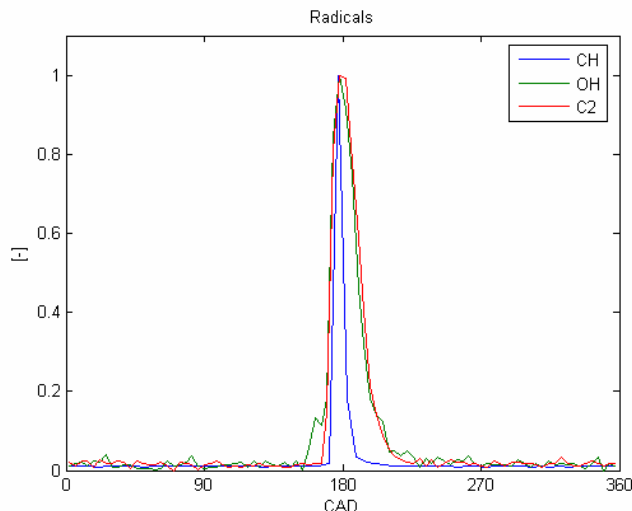
Figure 84: Radical evolutions at 13400 [rpm].

11.4 Metal engine versus optical engine

HCCI combustion is a process that relies on the autoignition of the fuel and consequently the temperature distribution in the combustion volume can substantially affect the behavior of the engine. The objective of this section is to compare the combustion features of metal and optical engines in order to understand whether the use of a quartz window could affect the performance of HCCI combustion. The comparison was carried out between the two engines with Propellers 1 and 4 as load.

At low speed, certain similarities in the shape of pressure, temperature and ROHR traces could be noted. The difference was due to the fact that the thermal conductivity of the quartz cylinder head was lower than that of its aluminum counterpart, thus resulting in a higher cylinder temperature in the optical engine and hence a different performance. With propeller 4, i.e. at high speed, the two engines showed no similarities whatsoever. This was mainly because of the heat transfer from the aluminum cylinder head being much higher than the one from the quartz head.

According to these results, two conclusions could be drawn for this small HCCI engine:

1. The optical engine behaved differently from the metal one and consequently the optical diagnostic merely represented an indication of what was going on.
2. The performance improvement of a mini high speed HCCI engine may be achieved with an enhanced thermal insulation of the cylinder head, considering that the heat transfer in the axial direction was much higher than that in the radial one.

A comparison between a metal and optical engine when using a normal-sized HCCI combustion chamber should answer the question whether the results presented in this section were particular for HCCI combustion in a small volume at a high engine speed.
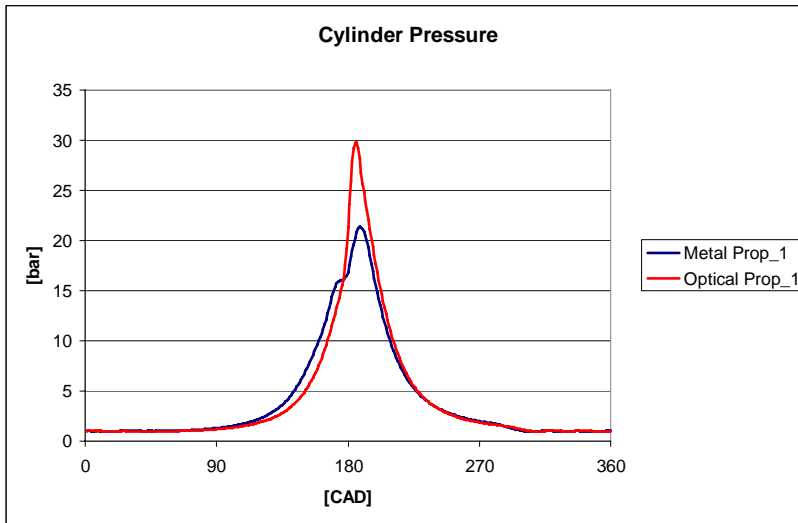
Figure 85: Cylinder pressure traces acquired for an optical and metal engine with Propeller 1 as load.
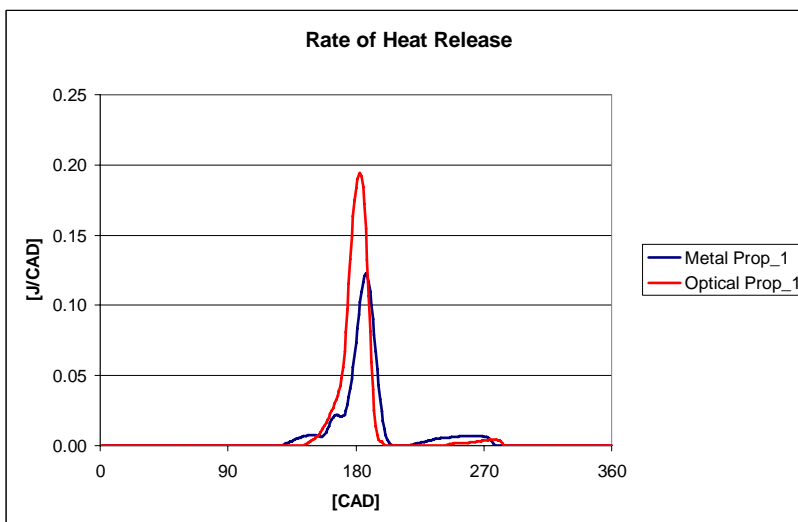
Figure 86: Rate of heat release traces obtained through post-processing the data from the optical and metal engines with Propeller 1 as load.
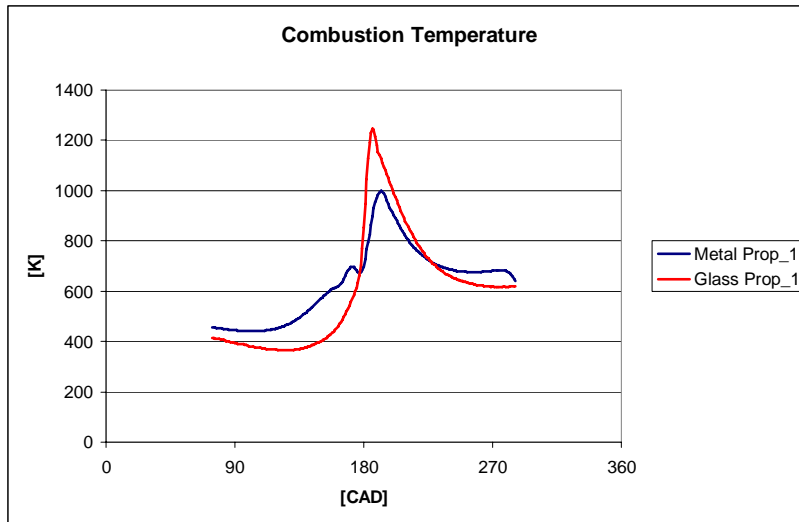
Figure 87: In-cylinder temperature traces obtained through post-processing the data from the optical and metal engines with Propeller 1 as load.

Table 8: Summary of the performance of the optical and metal engines when Propeller 1 was used as load.

	Optical	Metal	Variation [%]
N [rpm]	6646	7509	-11.49
x10 [ABDC]	169	166	1.81
x50 [ABDC]	182	186	-2.15
CD [CAD]	21	64	-67.19
CD [ms]	0.53	1.42	-62.93
Res [%]	39.10	48.27	-19.00
IMEP [bar]	1.78	1.08	64.81
Power [W]	81.82	56.15	45.72
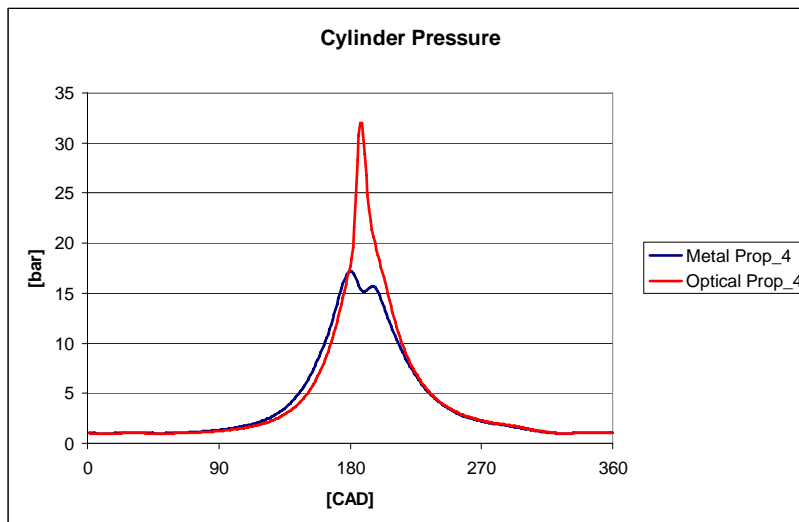
Figure 88: Cylinder pressure traces acquired for an optical and metal engine with Propeller 4 as load.
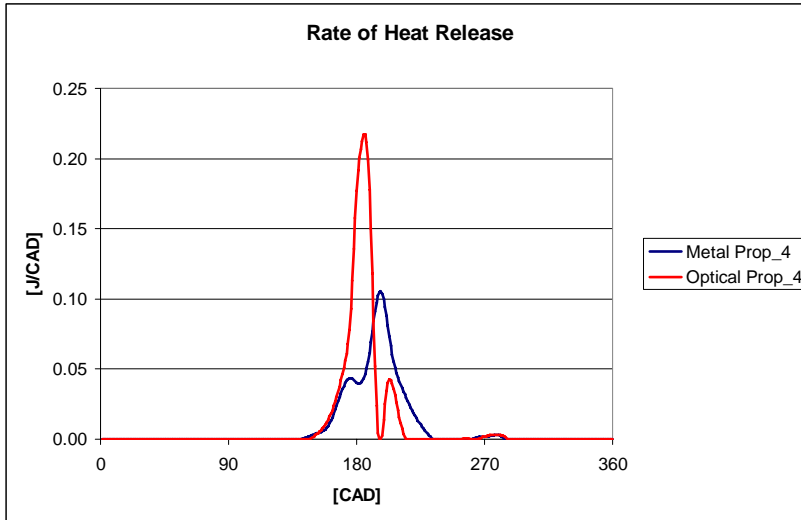
Figure 89: Rate of heat release traces obtained through post-processing the data from the optical and metal engines with Propeller 4 as load.
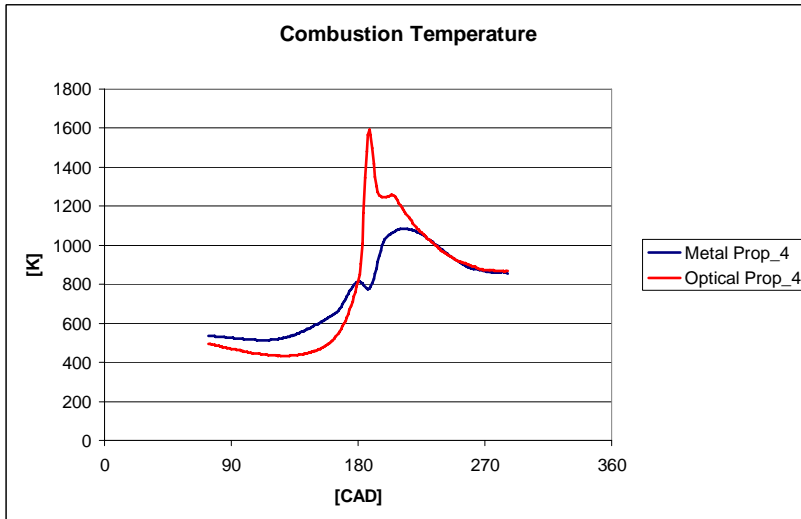
Figure 90: In-cylinder temperature traces obtained through post-processing the data from the optical and metal engines, with Propeller 4 as load.

Table 9: Summary of the performance of the optical and metal engines when Propeller 4 was used as load.

	Optical	Metal	Variation [%]
N [rpm]	14069	14991	-6.15
x10 [ABDC]	172	171	0.58
x50 [ABDC]	184	195	-5.64
CD [CAD]	29	43	-32.56
CD [ms]	0.34	0.48	-28.14
Res [%]	50.83	49.92	1.82
IMEP [bar]	2.48	1.61	54.04
Power [W]	240.96	166.24	44.95

11.5 Parameters affecting HCCI combustion

Once the viability of HCCI combustion in a small volume and at a high engine speed was proven, an analysis was carried out concerning certain parameters that may affect the process. This was done in order to optimize the small scale HCCI combustion. The variables under examination were:

- Squish distance.
- Wall temperature.
- Combustion chamber geometry.

11.5.1 Squish distance

For a pancake combustion chamber geometry, the squish distance was adjusted by using 5 spacers: 0.25, 0.50, 0.75 and 1.00 [mm]. The thicknesses of these spacing elements were of the same order of magnitude as the boundary layer and quenching distance. As a result, the performance was no longer mainly proportional to the compression ratio, $IMEP, \eta \propto 1 - \dfrac{1}{r_c^{\gamma-1}}$, but to quenching phenomena as well. It was impossible to further increase the squish distance since the compression energy was no longer enough to ignite the fuel.

A blend of 80% DEE and 20% castor oil was used, and for each squish distance, three measurements were performed. These were carried out at 3000, 7000 and 12000 [rpm].

The IMEP is shown in Figures 91 a and b. For each speed, it can be observed that IMEP initially increased when the compression ratio decreased and with a further reduction of this last parameter, the performance dropped until it became impossible to ignite the mixture. The phenomena can be explained in the following way. The thicknesses of the first two spacers were in the same size range as the quenching distance and consequently this parameter limited the conversion of fuel to usable work. The quenching effects became less and less important for an increasing squish distance up to an optimum point, i.e. 0.75 [mm]. After this optimum value, the effects of the quenching distance were less significant and the performance became proportional to the compression ratio as is generally the case for normal-sized engines. The same behavior was observed with the indicated efficiency, Figure 92.
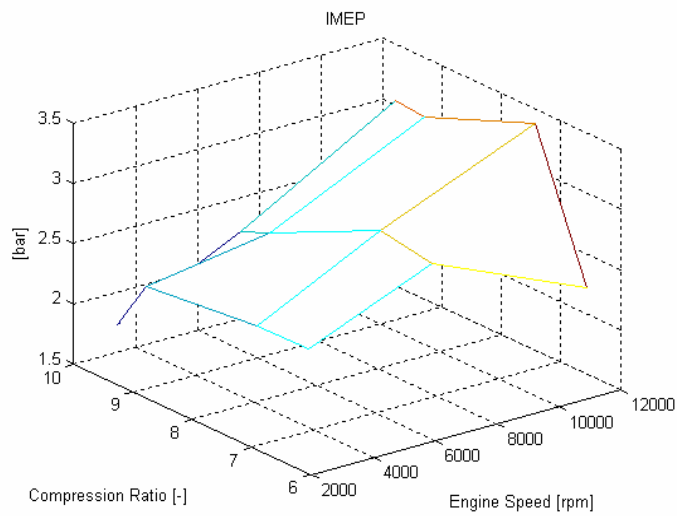
Figure 91 a: 3-D chart of IMEP as a function of engine speed and compression ratio.
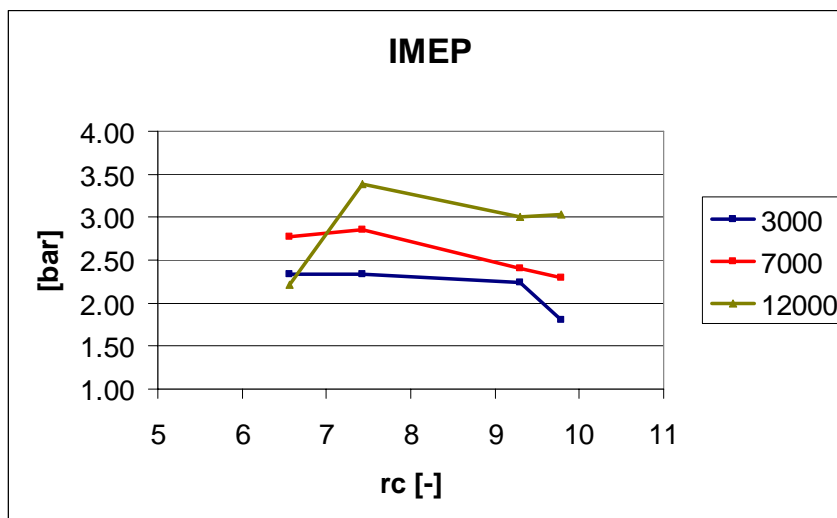
Figure 91 b: 2-D chart of IMEP as a function of engine speed and compression ratio.

Indicated Efficiency
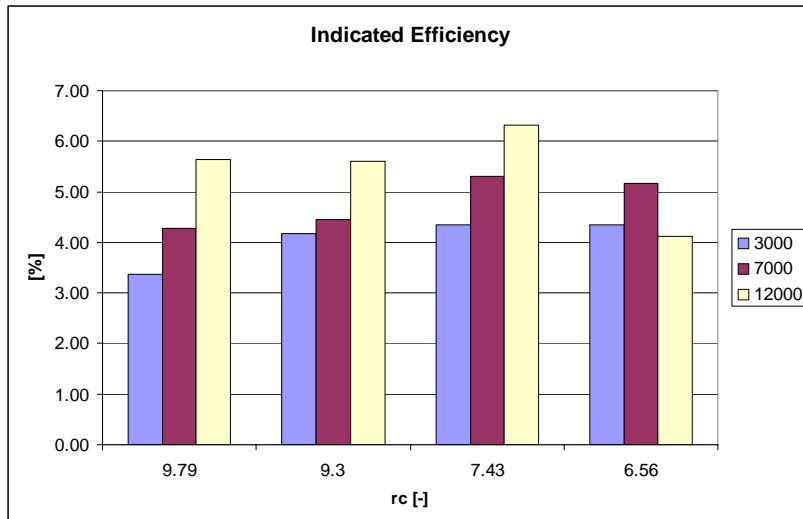
Figure 92: The indicated efficiency as a function of engine speed and compression ratio.

For the smallest spacer thickness, quenching phenomena were visible in the ROHR traces at all speeds, and for the second smallest spacer thickness, these phenomena appeared only at 7000 [rpm]. The quenching gave rise to a slowing-down of the release of heat when the piston was approximately at TDC. As it moved away from the top dead center, the reaction rate sped up again.
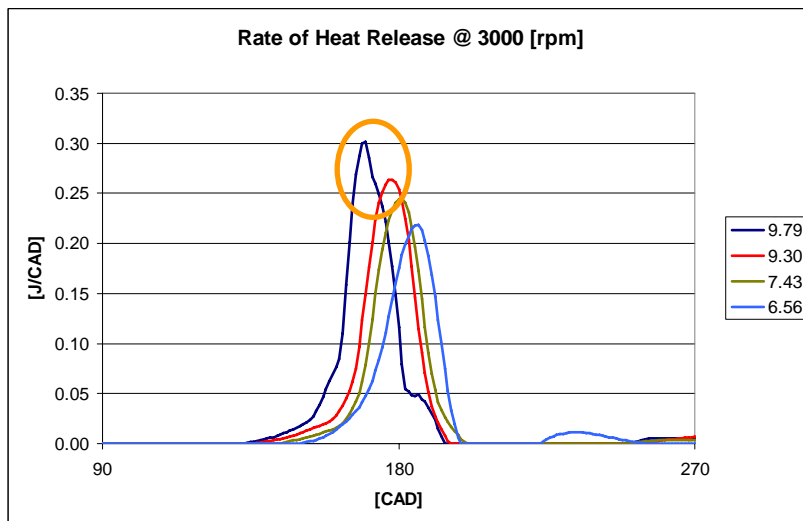
Figure 93 a: Ensemble averaged rate of heat release at 3000 [rpm] using four rc.
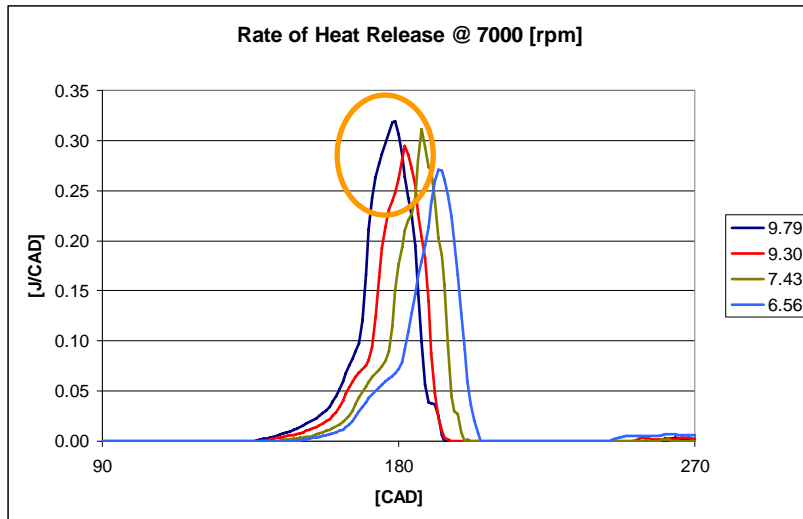
Figure 93 b: Ensemble averaged rate of heat release at 7000 [rpm] using four rc.
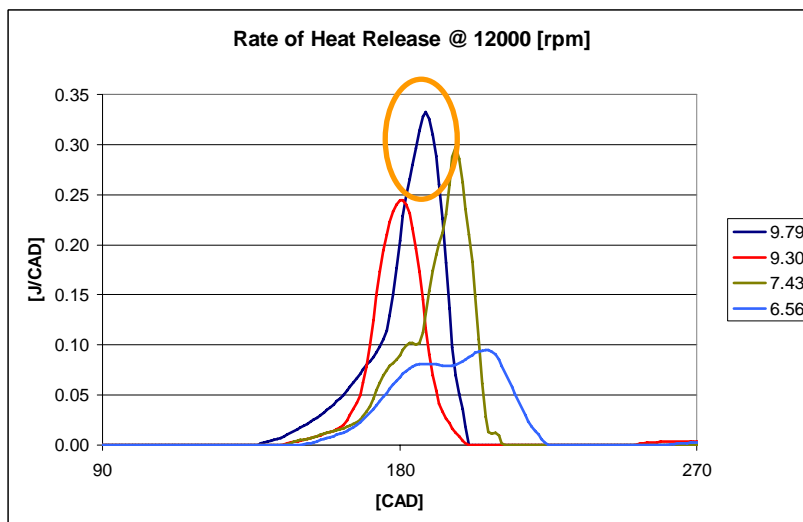
Figure 93 c: Ensemble averaged rate of heat release at 12000 [rpm] using four rc.

These sets of measurements assumed a fundamental importance in designing the VIMPA engine. Knowing that with a squish distance of 0.25 [mm] combustion remained possible as well as knowing that the optimum compression ratio was 7.43 [-], made it possible to calculate the minimum dimensions of the VIMPA combustion chamber, cf. *VIMPA Design.*

11.5.2 Wall temperature

HCCI combustion relies on the autoignition of the fuel and hence it is very sensitive to the combustion chamber temperature and boundary conditions. The study was performed in order to investigate whether increasing the cylinder wall temperature would result in an improved performance and indicated efficiency of the engine. The wall temperature was changed in the following way:

- High pressure air jet.
- Uncooled cylinder.
- Thermal barrier coating.

Figure 94 shows the IMEP values as functions of the wall temperature. The general trend was an initial decrease in IMEP values followed by an increment. This phenomenon was due to the fact that when the wall temperature was increased, two parameters worked in the opposite directions: the combustion efficiency (Figure 96) and the scavenging efficiency. The scavenging efficiency decreased with an increase in wall temperature basically because of the simultaneous warming of the crankcase due to the small dimensions of the engine. A warmer crankcase gave rise to a lowering of the density of the inlet mixture and poor performance was obtained. When the engine was not cooled, the loss in scavenging efficiency had a larger influence on the IMEP than the increment in combustion efficiency (i.e. the IMEP decreased). On the other hand, when the engine was hot, the improved conversion efficiency was higher than the loss in scavenging efficiency (i.e. the IMEP increased). Both these cases displayed lower IMEP values than when the engine was cooled. When pressurized air was used for cooling the cylinder walls, the scavenging efficiency was much higher, but unfortunately the combustion efficiency was rather low. The indicated efficiency followed the same trend as IMEP, Figure 95.
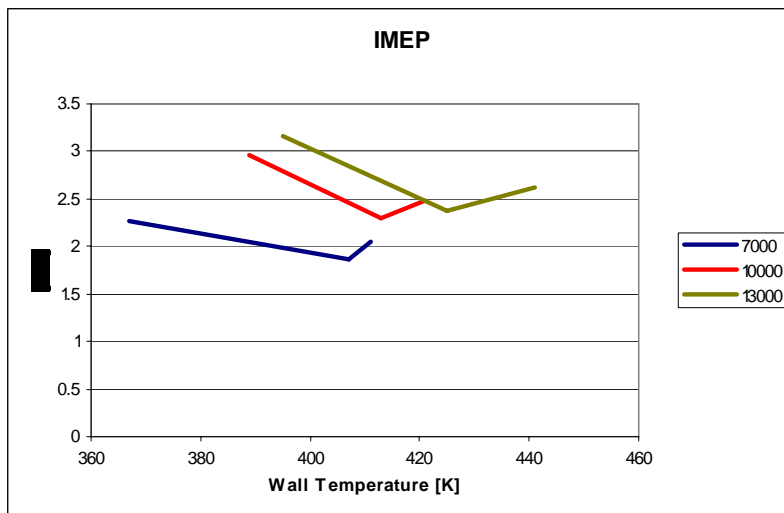
Figure 94: The IMEP variation as a function of the wall temperature and engine speed.
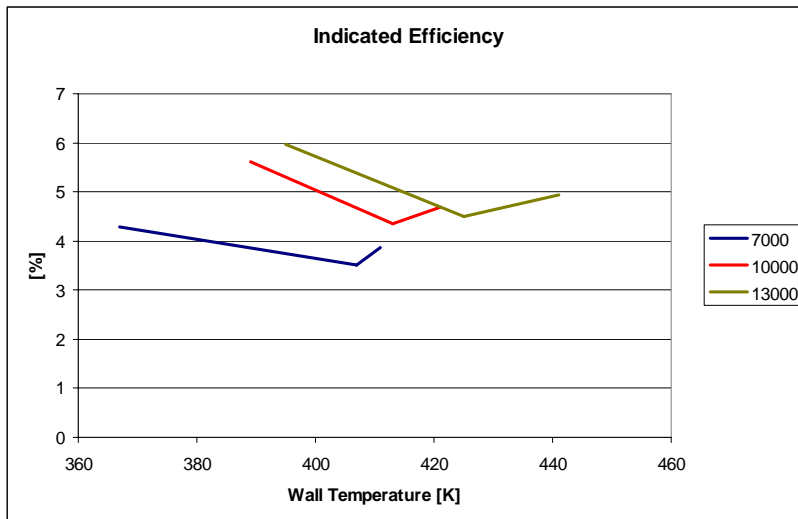
Figure 95: The indicated efficiency variation as a function of the wall temperature and engine speed.

In Figure 96, the combustion efficiency is plotted. When using the same cooling/thermal insulation method, an increase in speed increased the combustion efficiency since the heat losses were lower and the quenching distance, consequently, was smaller. Hence, more fuel could be converted into available energy. Increasing the wall temperature and maintaining a constant engine speed initially caused the combustion efficiency to worsen because of a smaller amount of mixture being inserted into the cylinder. Thereby, the radical recombination was enhanced on the cylinder walls. Later, a further increase in the wall temperature enabled both an improvement of the reactivity of the mixture and a reduction of the quenching distance.
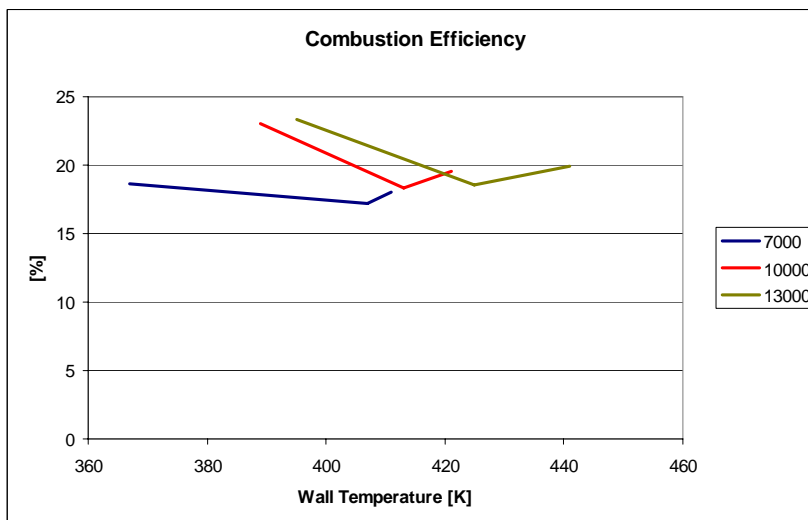
Figure 96: The combustion efficiency variation as a function of the wall temperature and engine speed.

The information that can be gained from this section is that the design of a miniature engine, such as the VIMPA, needs to include a cold crankcase and warm/hot combustion chamber walls in order to have good scavenging and relatively high combustion efficiencies.

11.5.3 Combustion chamber geometry

The aim of these measurements was to investigate whether the use of a bowl cylinder head was beneficial compared with the pancake geometry as a result of a lower area-to-volume ratio which should lead to less heat losses. The geometries of the two combustion chambers are shown in Figure 22.

Figure 97 shows the IMEP calculated for the bowl and pancake combustion chambers. In this study the parameters that affected the performance were:

- Heat losses.
- Quenching phenomena.

At 7000 rpm, because of the lower area-to-volume ratio and the low quenching problems on the side of the bowl, the bowl cylinder head displayed a better behavior as compared to the pancake combustion chamber. By increasing the engine speed to 10000 rpm, it was possible to increase both the retained burned gases as well as the combustion chamber temperature. An increment of the residual gases signified a lowering of the mixture's reactivity and thus an increase of the quenching distance. On the other hand, an increase in the combustion chamber temperature would lead to more reactive mixture and a lower sensitivity to the quenching phenomena. Because of the low squish distance on the side of the bowl, i.e. 0.25 [mm], the quenching phenomena assumed a non-negligible importance in this area causing the reactions to occur mainly in the bowl. On the other hand, because of the improvement of the thermal management, the reaction rate increased all over the pancake combustion chamber. For these reasons, at 10000 [rpm], the pancake geometry provided a better performance than the bowl cylinder head. A further increase in engine speed, 13000 rpm, emphasized the phenomena described at 10000 [rpm].
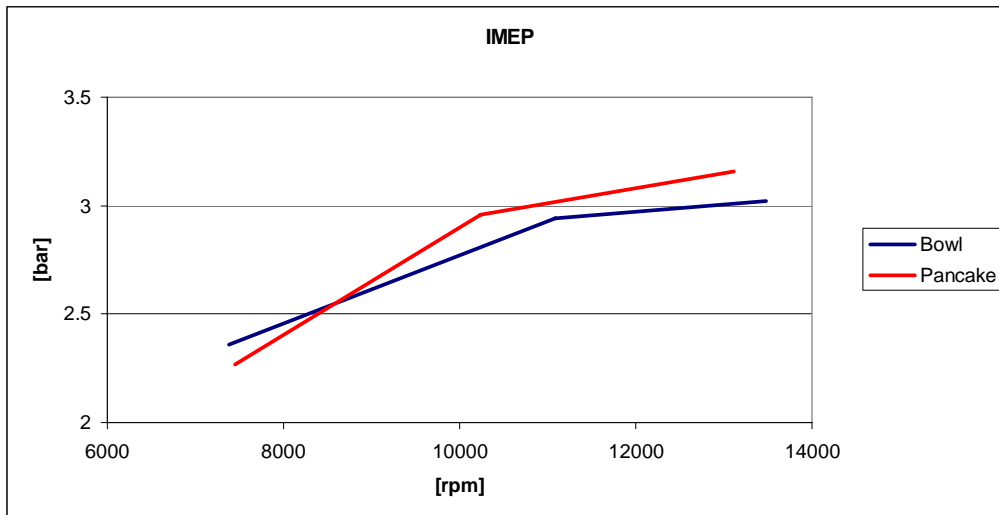
Figure 97: IMEP versus engine speed using a bowl and pancake combustion chambers.

Figure 98 shows the indicated efficiency. For the pancake geometry, this parameter increased with speed as a result of the thermal management being improved all over the combustion chamber. In the bowl combustion chamber, the indicated efficiency was basically constant since the quenching phenomena increased on the side of the bowl and the reaction rate improved in the bowl. These two phenomena compensated each other.
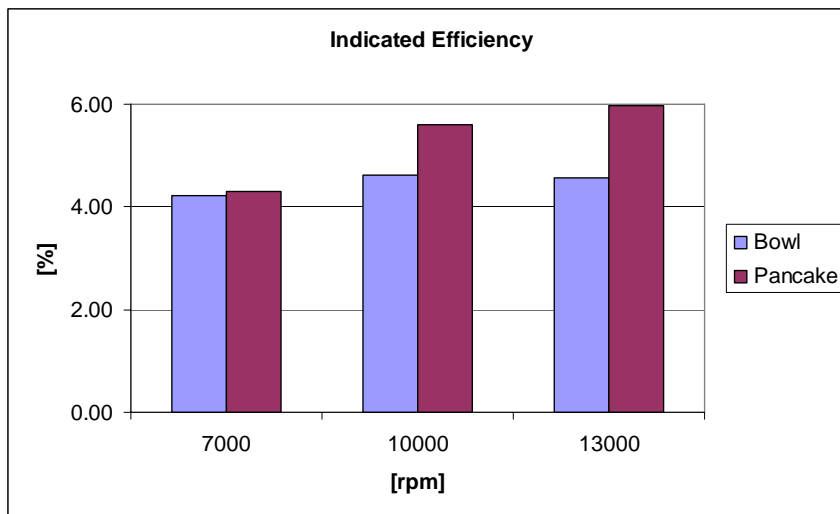
Figure 98: The indicated efficiency versus engine speed using a bowl and pancake combustion chambers.

After these sets of measurements it could be concluded that for centi-scale HCCI combustion, the pancake combustion chamber was the most suitable geometry. This was due to it being less sensitive to local quenching problems as was the case of the side areas in the bowl combustion chamber. Moreover, the speed could be optimized in order to obtain a compromise between the thermal management and the amount of retained burned gases thereby leading to a good output power.

12. Trapping efficiency and residual models

12.1 Introduction

The quantification of the trapping efficiency and residual gas fraction is one of the key factors for understanding the behavior, in terms of performance and emissions, of a 2-stroke engine.

In 1914 Hopkinson was the first to introduce the perfect mixing and perfect displacement models for computing the trapping efficiency and other important parameters in a 2-stroke engine [45]. Unfortunately these models represent two ideal cases and none of them can approximate the reality accurately. Since the "truth" lies in between, Benson and Brandham suggested a two part model for the scavenging process [46]; at the beginning the perfect displacement was used and when a prescribed delivery ratio was reached, the perfect mixing model was adopted.

Nowadays the most used 1D algorithm for estimating the trapping efficiency and various parameters of a 2-stroke engine is the one introduced by Blair [47]. This method incorporates the perfect displacement and the perfect mixing models but instead of switching from one to the other (as with Benson and Brandham) the transition is smoother. The two models are used simultaneously; when the fresh charge enters the cylinder a percentage of it mixes with the burned gases and is expelled through the exhaust port while the remaining part is displaced inside the cylinder. The percentage of fresh mixture that mixes with the burned gases increases linearly with the instantaneous value of the scavenging ratio. This model is simple to implement, it is fast in terms of computational time, the tuning is simple and it has been shown to predict reality with relatively good accuracy for a broad range of scavenging ratios and port configurations [47]. Finally, there is the possibility of using a full CFD model that can give good results but unfortunately has a non-negligable computational time.

This section describes an alternative method for calculating the trapping efficiency and residual gas fraction. As in the Benson and Brandham model [46], the perfect mixing and perfect displacement models are combined but here the border between them is a multiple of the time required for the largest eddy to perform one revolution. This is due to the mixing depending on the flow and turbulence motion inside the cylinder rather than on a prescribed value of the delivery ratio. This new "switch" model is not an attempt to replace the reliable and well-known Blair model. However, it has been noted that for a mini high speed HCCI engine, the difference, expressed as a percentage, between the measured trapping efficiency, and that predicted either by the Blair model or the present model is much lower for the latter.

Accurate measurements of the trapping efficiency and residuals are difficult to obtain because of the problem of measuring the fresh trapped mixture. It was Sammons who, in the 40s [48], proposed to measure the oxygen concentration in the exhaust in order to calculate the trapping efficiency for engines that were running rich. Due to the inaccuracy of the exhaust analyzers of that period, the method was forgotten until the 70s when it was revived by Sanborn [49]. According to this method, if the engine is fed with a rich mixture, oxygen is present in the exhaust because of a short-circuiting of the charge. Because of the simplicity of this method, it is still widely used

for calculating the trapping efficiency. However, when applied to a very small engine operating at a high rotational speed, not all of the oxygen in the exhaust originates from the by-passed fresh charge, but is also due to quenching phenomena and incomplete combustion. Consequently the results from the model are inadequate in this case. Flow visualization experiments [50] and flow velocity mapping techniques have provided useful information but unfortunately their accuracy is not very high and there are not always data available for the engines under examination.

In the section 12.3, a method for performing a direct measurement of the trapping efficiency is proposed. The technique consists in very accurate and fast measurements of the temperature in the crankcase during the intake, the exhaust temperature and an estimation of the blow-down temperature before the intake port opens. It will be shown later on that the trapping efficiency is a linear function of these three temperatures.

12.2 Model

As previously stated, this model is a combination of the perfect mixing and perfect displacement models. The estimation of the trapping efficiency and residual gas fraction was performed under the assumptions that:

- The flow through the inlet and exhaust ports was 1-D compressible.
- The rotational speed of the largest eddy increased linearly with the mean piston speed.
- The largest eddy was circular and its diameter was half that of the bore.
- The inlet temperature was the one measured in the crankcase.
- The fresh charge that was bypassed during the scavenging process had the same temperature as the crankcase and was not heated when traveling through the combustion chamber.

In the first part of the scavenging process, only the burned gases were pushed out because of the action of the fresh charge; and thus the perfect displacement model was used:

Equation 7: Set of relations used for computing the residuals and trapped fresh charge.

$$m_{res}(\theta) = m(\theta) - m_{out}(\theta) \cdot d\theta$$
$$m_{FT}(\theta) = m_{FT}(\theta - 1) + m_{in}(\theta) \cdot d\theta$$
$$m_{FM\_OUT}(\theta) = 0$$

Here:

m_{res} is the residual mass fraction.
m is the instantaneous cylinder mass.
m_{out} is the mass flow through the exhaust port.
m_{in} is the mass flow through the inlet ports.
m_{FT} is the mass of the trapped fresh mixture.
m_{FM_OUT} is the mass of fresh mixture that goes to the exhaust tail.

θ is the instantaneous CAD.
dθ is the differential CAD.

After one turn of the largest eddy, the perfect mixing model is adopted:

Equation 8: Set of relations used for computing the residuals and trapped fresh charge.

$$m_{FM\_OUT}(\theta) = m_{FM\_OUT}(\theta - 1) + \dot{m}_{out}(\theta) \cdot \frac{m_{FT}(\theta)}{m(\theta)} \cdot d\theta$$

$$m_{FT}(\theta) = m_{FT}(\theta - 1) + \dot{m}_{in}(\theta) \cdot d\theta - \dot{m}_{FM\_OUT}(\theta) \cdot d\theta$$

$$m_{res}(\theta) = m_{res}(\theta - 1) - \dot{m}_{out}(\theta) \cdot \frac{m(\theta) - m_{FT}(\theta)}{m(\theta)} \cdot d\theta$$

The crank angles necessary for switching from the first to the second model were computed in the following way:

Equation 9: Set of relations necessary for computing the CAD interval between the two models.

$$\Theta = \frac{360 \cdot N}{60} \cdot t$$

$$t = \frac{L}{v}$$

$$v = k \cdot 2 \cdot l \cdot \frac{N}{60}$$

$$L = 0.5 \cdot B$$

Here:

Θ is the CAD interval between the perfect mixing and perfect displacement models.
t is the time necessary for the largest eddy to perform one revolution.
L is the diameter of the largest eddy.
v is the speed of the largest eddy.
N is the engine speed.
k is the tuning parameter.

Finally, the residual mass fraction and trapping efficiency can be computed as follow:

Equation 10: The trapping efficiency and residual gas fraction.

$$\eta_{trap} = \frac{m_{FT}(\theta_{EPC})}{m_{in}(\theta_{EPC})}$$

$$\%_{RES} = 100 \cdot \frac{m_{res}(\theta_{EPC})}{m(\theta_{EPC})}$$

Further details of the equations used in this model can be found in Paper 6.

12.3 Validation and tuning

The validation of the model was done by measuring the trapping efficiency. If fast measurements of the crankcase and exhaust temperature are possible and the blow-down temperature is estimated, the trapping efficiency can be written as:

Equation 11: The measured trapping efficiency.

$$\eta_{trap} = \frac{T_{AVG\_EX} - T_{AVG\_IN}}{T_{AVG\_BD} - T_{AVG\_IN}}$$

This is because the average exhaust gas temperature in one cycle can be seen as a linear function of the crankcase and blow-down temperatures:

Equation 12: The average exhaust gas temperature.

$$T_{AVG\_EX} = (1 - \eta_{trap}) \cdot T_{AVG\_IN} + \eta_{trap} \cdot T_{AVG\_BD}$$

Here:

T_{AVG_EX} is the average exhaust gas temperature for one cycle.
T_{AVG_BD} is the average temperature during the blow-down phase.
T_{AVG_IN} is the average crankcase temperature for one cycle.

Further explanations concerning Equation 12 can be found in Paper 6.

Once the measured trapping efficiency is obtained, the value of the tuning parameter, k, can be chosen in order to match the model to the experimental data. The value of k does not change with the engine speed.

12.4 Results

The model was validated by experiments carried out on a mini high speed HCCI engine fueled with a blend of 80% DEE and 20% castor oil, operating between 10000 and 20000 [rpm]. Figure 99 and 100 show respectively the variation of the calculated trapping efficiency and the residual mass fraction as functions of the tuning parameter and the engine speed.
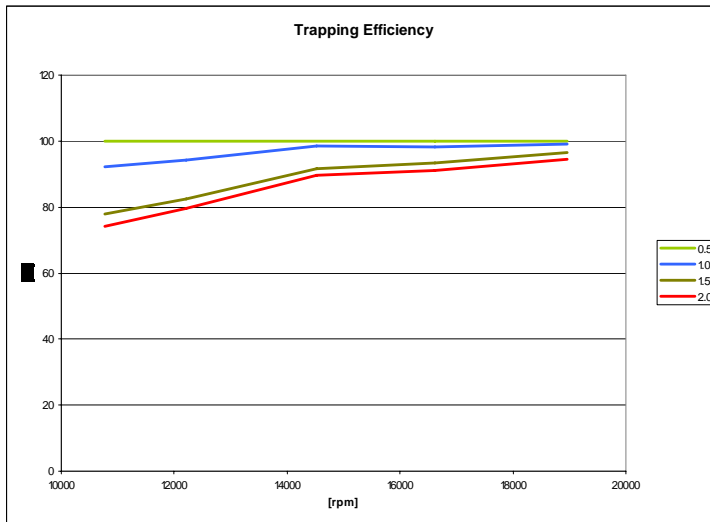
Figure 99: The calculated trapping efficiency as a function of the engine speed and tuning parameter.
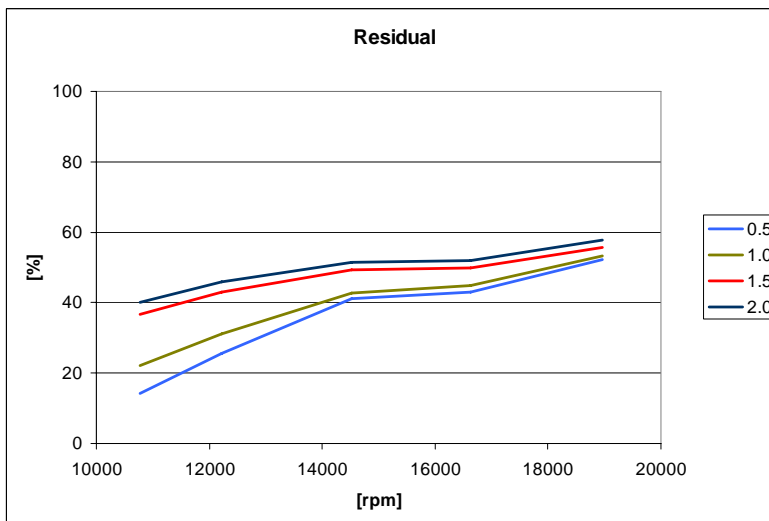
Figure 100: The calculated residual mass fraction as a function of the engine speed and tuning parameter.

Figure 101 displays the measured trapping efficiency and its counterparts calculated with the custom model as well as the Blair model. The tuning parameter was set to 1. The agreement between the results of the custom model and the measured values of the trapping efficiency was better than what one can achieve with the Blair model. Figure 102 shows the errors, expressed as percentages, of the two models as

compared to the experimental results for the trapping efficiency. The errors were found to decrease significantly for increasing rotational speed.
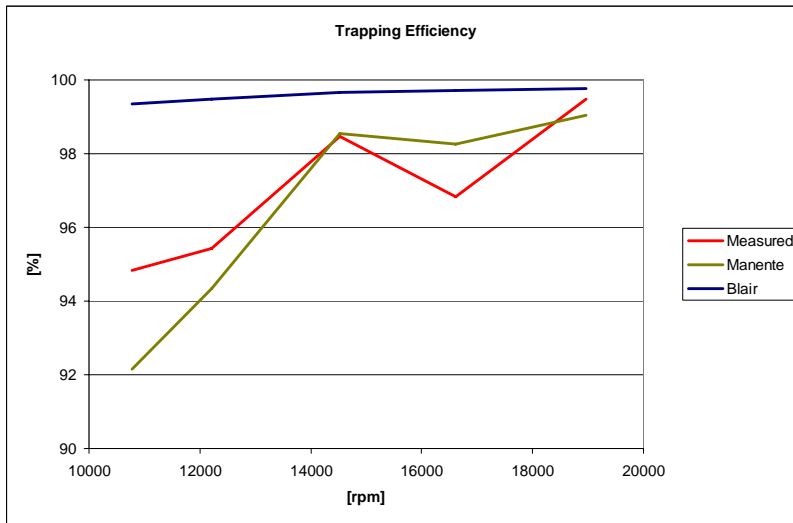
Figure 101: The measured trapping efficiency plotted with those computed with the Blair and the custom-made models.
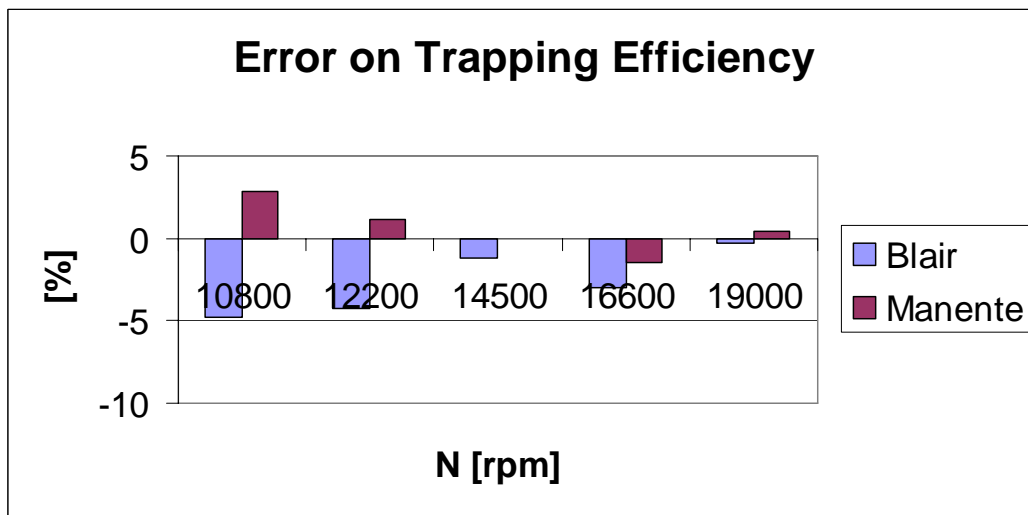
Figure 102: The errors, expressed as percentages, between the measured trapping efficiency and those computed with the Blair and the custom-made models.

Figure 103 shows the residual gas fraction as computed with the Blair and the custom-made models. The two models showed similar trends and the difference between them was decreased with an increasing engine speed. The custom-made model consistently displayed higher values than the Blair model.
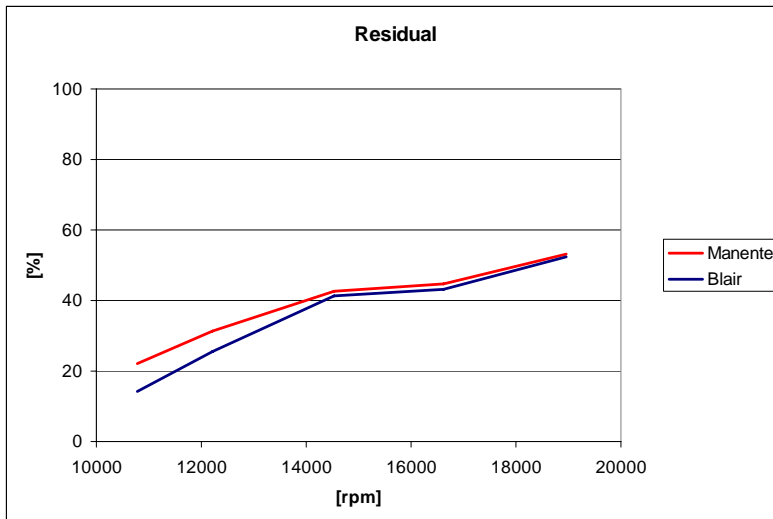
Figure 103: The residual gas fraction computed with the Blair and the custom-made models.

Figure 104 shows the trapping efficiencies, calculated with various models, versus the delivery ratio. Unfortunately, during the tests, this parameter varied only between 26 and 37%. The proposed model matched the experimental data better than the others; Blair's algorithm showed a small discrepancy, and the perfect mixing and perfect displacement models were too simplistic to give accurate results.
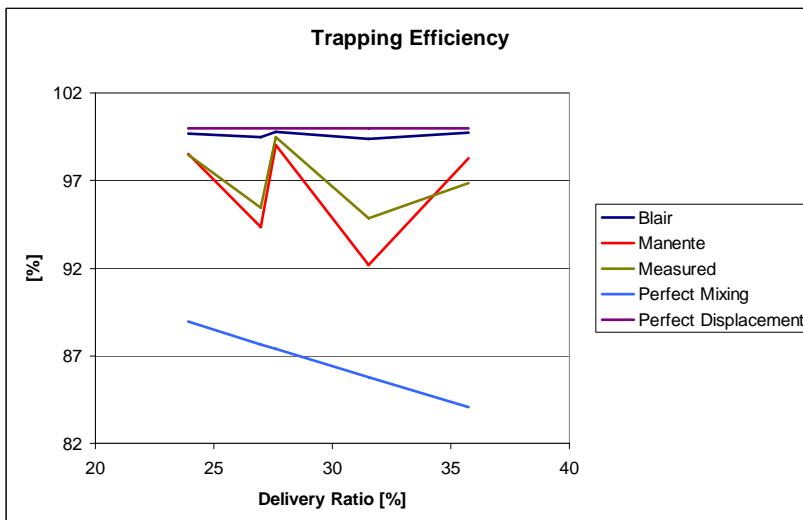
Figure 104: The trapping efficiency (calculated with the Blair, perfect mixing and perfect displacement models as well as the one under examination) as a function of the delivery ratio.

12.5 Future work

The method for estimating the trapping efficiency and residual gas fraction was applied to a wide range of rotational speeds, a narrow range of delivery ratios and was validated using a mini high speed HCCI engine. It would be interesting to study the accuracy of this algorithm for a broader range of delivery ratios, different port configurations and when using a normal-sized engine in order to investigate whether it would be possible to achieve the same accuracy as the Blair model [47].

13. VIMPA Design

The knowledge gained during this first year and a half of my PhD project was subsequently put to use in the design of the second version of VIMPA, Figure 4. The design consisted in developing the entire combustion chamber, crankcase and piston. The next sections show the working principle and design criteria of this mini high speed, free piston engine.

13.1 Working principle

The thermodynamic cycle was very similar to a 2-stroke HCCI engine, with two main differences:

- The way the air was sucked into the crankcase.
- The control of the piston motion.

In Figure 105, the main parts of the VIMPA engine are shown:

1- Stopping spring.
2- Intake channel.
3- Crankcase.
4- Working piston.
5- Combustion chamber.
6- Exhaust channel.
7- Crankcase piston.
8- Air intake port.
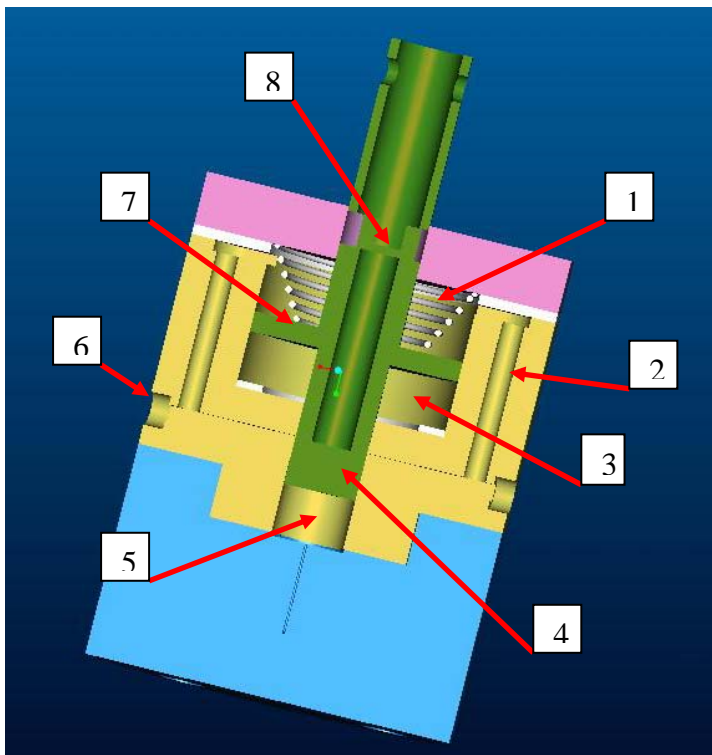
Figure 105: VIMPA main components.

After the ignition, that takes place around TDC, the piston starts to move up:

- The mixture in the combustion chamber burns and expands.
- The fresh mixture in the crankcase is compressed and pushed into the intake channels, but is not yet in communication with the combustion chamber.
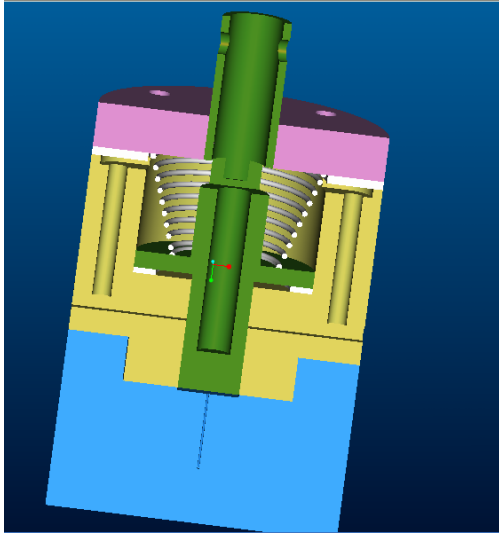
Figure 106: Working piston at TDC and crankcase piston at BDC.

When the working piston is at -62 CAD aBDC, the exhaust ports open and the exhaust phase starts. At -50 CAD aBDC, the intake ports open. The pressure in the combustion chamber is almost ambient and the fresh mixture is sucked inside as a result of the working piston moving outward and because of the over-pressure created by the crankcase piston.
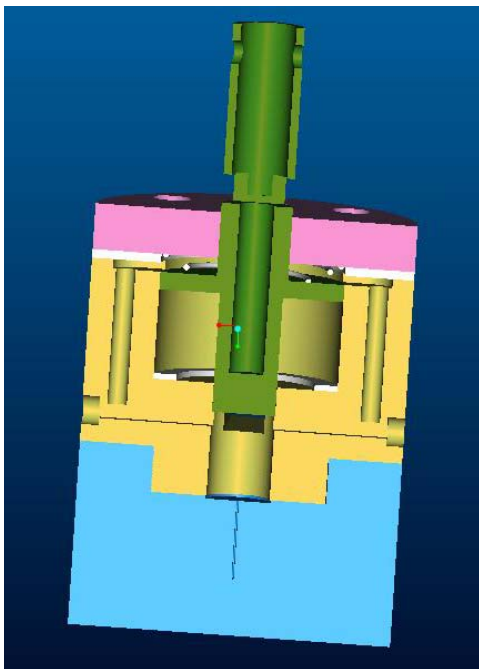
Figure 107: Working piston at BDC and crankcase piston at TDC.

The working piston is stuck at BDC until the force exerted by the spring and the pressure in the crankcase is higher than the one created by the pressure in the combustion chamber. When this condition is met, the working piston starts to move down and the mixture is compressed until the ignition takes place around TDC. The cycle thus starts over again.

When the working piston is at TDC and the crankcase piston is at BDC, two ports on the piston shaft put the ambient surroundings in contact with the crankcase thus allowing fresh air to be sucked inside.
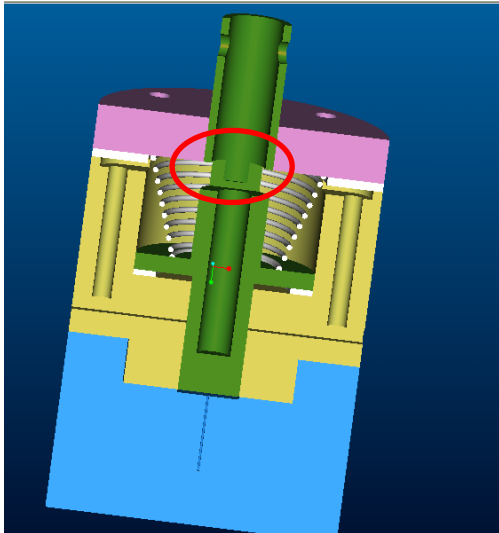
Figure 108: Fresh air intake.

The fuel is injected by the use of a simple carburetor mounted on top of the crankcase; the purple plate in Figure 108. A check valve is placed between the carburetor and the crankcase in order to prevent back-flow when the crankcase piston moves up.

The combustion mode was chosen as HCCI since the idea was to keep the design as simple as possible. This combustion relies on autoignition of the fuel and hence additional components such as a spark or glow plug were not necessary. Diethyl ether was chosen as fuel. The output power was collected by an electromagnetic linear generator mounted on the shaft of the piston.

13.2 Combustion chamber

It has been shown that when diethyl ether is used as fuel in HCCI combustion, the ignition takes place without quenching problems even when the distance between the top of the piston and cylinder head is only 0.25 [mm] [51]. It has also been shown that the compression ratio that gives the best performance in HCCI combustion with DEE is 7.43 [-] [51] and that the most suitable combustion chamber in a mini engine is one with a pancake geometry [44]. The knowledge of these three parameters allowed the calculation of the minimum dimensions of a VIMPA combustion chamber with all the ports closed.

Equation 13: Relation for calculating the stroke of the VIMPA engine.

$$rc = \frac{V_{max}}{V_{min}} = 1 + \frac{V_d}{V_c} = 1 + \frac{St \cdot 0.25 \cdot \pi \cdot D^2}{Sq \cdot 0.25 \cdot \pi \cdot D^2}$$

$$\Rightarrow St = SF \cdot Sq \cdot (rc - 1)$$

Here:

rc is the compression ratio.
V_{max} is the maximum volume in the combustion chamber.
V_{min} is the minimum volume in the combustion chamber.
V_d is the displacement volume.
V_c is the clearance volume.
St is the stroke when the ports are closed.
Sq is the squish distance.
D is the bore.
SF is the safety factor that takes into account leakages between piston and liner, as well as heat losses.

It is assumed that the bore is equal to the stroke when the ports are closed.

The calculations led to the following results:

Table 10: VIMPA combustion chamber geometry.

D	5.48	[mm]
St	5.48	[mm]
Sq	0.25	[mm]
SF	3.08	[-]
rc	22.92	[-]

The combustion chamber had a pancake geometry.
For the scavenging process, two intake and two exhaust ports symmetrically placed in the circumferential direction were used in order to avoid short-circuiting of the fresh mixture.
The flow through the ports was modeled as 1-D compressible:

Equation 14: Relations governing the flow through the intake and exhaust ports. The subscript 1 indicates the inlet conditions while 2 refers to the outlet.

$$\dot{m}(t) = \frac{C_D \cdot A \cdot P_1}{\sqrt{R \cdot T_1}} \cdot \left(\frac{P_2}{P_2}\right)^{1/\gamma} \cdot \left\{\frac{2 \cdot \gamma}{\gamma - 1} \cdot \left[1 - \left(\frac{P_2}{P_2}\right)^{\gamma - 1/\gamma}\right]\right\}^{1/2}$$

in case of chocked flow:

$$\dot{m}(t) = \frac{C_D \cdot A \cdot P_1}{\sqrt{R \cdot T_1}} \cdot \gamma^{1/2} \cdot \left(\frac{2}{\gamma + 1}\right)^{\gamma + 1/2 \cdot (\gamma - 1)}$$

It was assumed that during one cycle, the mass of the mixture that had to be sucked into or be exhausted from the cylinder was equal to the displacement volume times

the density of the mixture at ambient conditions. The pressure difference during the intake and the exhaust was assumed to be constant and was set to 0.1 [bar] and 0.3 [bar], respectively. The calculations were computed in order to provide an optimum performance at 12000 [rpm]. The exhaust was opened at -62 aBDC while the intake took place at -50 aBDC. The ratio between the height and width of the exhaust and intake ports was set to 0.50 in the first case and 0.70 in the second.

Table 11: Port geometries.

	Width	Height	
Exhaust	3.52	1.85	[mm]
Intake	1.80	1.25	[mm]

13.3 Crankcase and piston ports

The crankcase was designed in order to give an absolute pressure of 1.5 [bar] before the opening of the intake ports. The compression stroke was approximated with a polytropic relation: $P \cdot V^{\gamma} = const$. The value of gamma was set to 1 since the fuel was not perfectly vaporized at high speed and consequently a part of the compression energy was spent in fuel vaporization. The volume of the crankcase was approximately fourfold the one in the combustion chamber, thus preventing back-flow during the scavenging process. Two holes were drilled on the side of the crankcase piston, Figure 109, so as to avoid a depression being created when the piston moved up. The stiffness of the spring in the crankcase was chosen to minimize the time that the piston was stuck at BDC before the force from the spring and the pressure in the crankcase was higher than that exerted by the combustion pressure. With the given piston geometry, using steel, the stiffness was found to be 600 [N/m].

The ports in the upper part of the piston were designed in order to supply a mass of air in each cycle equal to the displacement volume times the ambient density. It was assumed that the flow was 1-D and compressible, cf. Equation 14; and the area was optimized to work properly at 12000 [rpm]. There were two ports, circumferentially symmetric, with heights of 2.5 [mm] and widths of 4.3 [mm].

Figure 109: Orifices for pressure equalization.
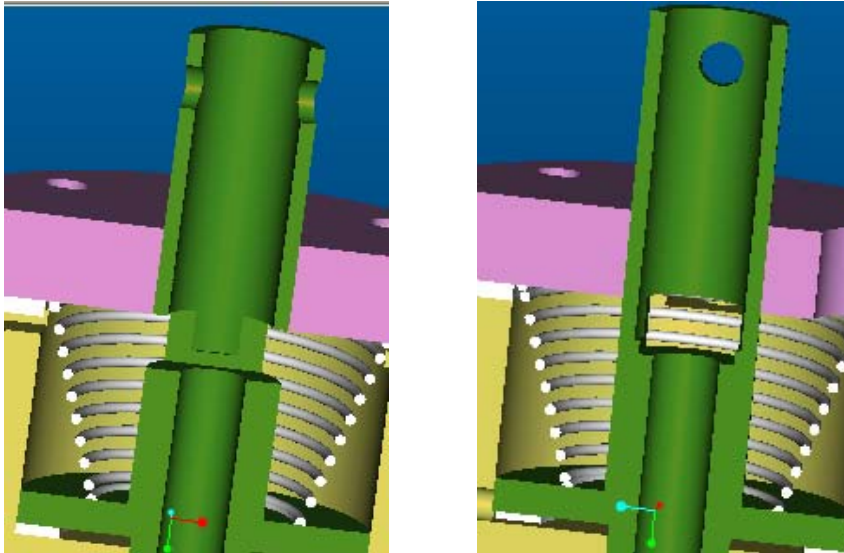
Figure 110: Piston inlet ports.

13.4 FEM analysis

A fatigue simulation was carried out in order to verify whether the combustion chamber had infinite life. The analysis was computed approximating the cylinder pressure as sinusoidal with an amplitude of 15 [bar] and a mean value of 15 [bar]. The temperature differential between the inner and outer parts of the combustion chamber walls was set to 40 [K]. The steel used was AISI 416. Taking into account the roughness of the material, its fatigue limit was 275 [Mpa] at $2e^6$ cycles. The ratio between this value and the maximum stress obtained from the simulations was 1.41 [-], indicating that the component had infinite life.
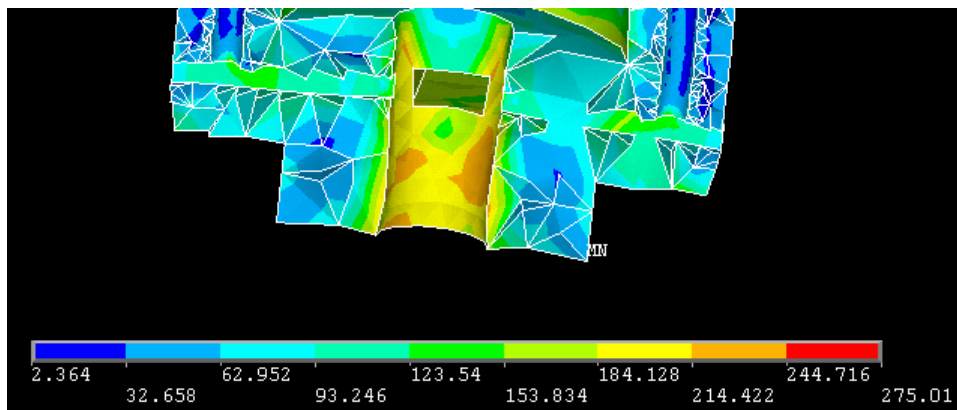
Figure 111: Combustion chamber FEM analysis.

14. Summary and conclusions

The combustion in a small volume at high rotational speed has been investigated both for a glow plug engine and a HCCI one. The study demonstrated that glow plug combustion relied on propagating autoignition reactions, where the mixture was partially ignited by the energy coming from the compression stroke and the remaining part by the heat supplied by the glow element. With this engine, the operating range for speed was found between 10000 and 17500 [rpm] while it was between 1 and 3 [bar] for IMEP.

By using only the compression energy, HCCI combustion could be achieved in the centi-scale and its viability was proven. The working range with respect to speed was between 3000 and 20000 [rpm] whereas it was between 1 and 3.5 [bar] for IMEP.

With both combustion modes, the limitations in maximum speed were due solely to structural reasons; high levels of vibrations always led to mechanical failures. With the exception of the maximum cylinder pressure, HCCI combustion was not limited in minimum speed. On the other hand, the glow plug engine could not run slower than 10000 [rpm] as a result of the glow plug cooling down and there not being enough energy to ignite the mixture. For both engines, the IMEP values were limited by the low combustion efficiency and the large heat losses.

Despite the modality of triggering the reactions (glow plug or autoignition), the present research has underlined that when the combustion takes place in a small volume there are two main deficiencies: very low combustion efficiencies and high emission levels. The parameters responsible for this were quenching phenomena and the boundary layer. Quenching mainly limited the amount of fuel that could be transformed into usable energy while the boundary layer led to incomplete reactions and thus higher emission levels coupled with lower indicated work. Optical diagnostics demonstrated that for both engines, when the piston was at TDC, the boundary layer in the radial direction was 15% while it was 100% in the axial one. By heating up the inlet mixture, changing the combustion chamber geometry or coating the combustion chamber walls, attempts were made to improve the combustion efficiency and to lower the emission levels. However, these improvements were not very significant and unfortunately, in many cases, the performances were penalized.

The goal of understanding how combustion works in a small volume at high engine speed was set in order to design a vibrating microengine for power generation and microsystems actuation, VIMPA, with the aim of replacing electrochemical batteries. This would require a minimum overall efficiency of 3% for the device. The present study has shown that it was possible to meet this target both with glow plug and HCCI combustion. The knowledge gained from HCCI combustion experiments in the centi-scale and the broad background in solid mechanics was sufficient for the author to single-handedly design a VIMPA: including the combustion chamber, injection system, body and the test cell. This thesis does not present any results on this new engine since the tests will not start until October 2007. The challenge of developing a reliable and hopefully marketable VIMPA engine has just begun.

15. References

1. Deluga G. A., Salge J. R., Schnidt L. D., "Renewable Hydrogen from Ethanol by Autothermal Reforming", Science, 303, 2004.
2. Service R. F., "Shrinking Fuel Cells Promise Power in Your Pocket", Science, 296, 2002, 1222-1224.
3. Epstein A. H., Jacobson S. A., Protz J. M., Frechette L. G., „Shirtbutton-sized Gas Turbine: the Engineering Challenge of Micro High Speed Rotating Machinery", Proceeding of the 8th International Symposium on Transport Phenomena and Dynamic of Rotating Machinery, Honolulu, Hawaii, January 2000.
4. Fernadez-Pello A. C., "Micropower Generation Using Combustion: Issues and Approaches", 29th International symposium on Combustion, Saporro, Japan, 2002.
5. Kang S., "Fabrication of Functional Mesoscopic Ceramic Parts for Micro Gas Turbine Engines", PhD thesis, Stanford University, 2001.
6. Isomoura K., Murayama M., Yamaguchi H., Ijichi N., Asakura H., Saji N., Shiga O., Takahashi K., Kawakubo T., Watanabe T., Yamagata A., Tange H., Tanaka S., Genda T., Hesashi M., "Disgn Study of a Micromachined Gas Turbine with 3-D Impeller", 9th International Symposium on Transport Phenomena and Dynamic of Rotating Machinery, Honolulu, Hawaii, January 2002.
7. Peirs J., Reynaerts D., Verplaetsen F., "Development of an Axial Microturbine for a Portable Gas Turbine Generator", Journal of Micromechanical and Microengineering, 13, 2003, S190-S195.
8. Sitzki L., Borer K., Schuster E., Ronney P. D., "Combustion in Microscale Heat Recirculating Burners", 3rd Asia Pacific Conference on Combustion, Korea, 2001.
9. Spadaccini C., Zhangb X., Cadouc C. P., Mikia N., Waitza I. A., "Preliminary Development of a Hydrocarbon Fuel Catalytic Micro Combustor", Sensors and Actuators, A 103, 2003, 219-224.
10. H. T. Aichlmayr, D. B. Kittelson, M. R. Zachariah, "Micro-HCCI combustion: experimental characterization and development of a detailed chemical kinetic model with coupled piston motion", Combustion and Flame, 135, 2003, 227–248.
11. H. T. Aichlmayr, D. B. Kittelson, M. R. Zachariah, "Miniature Free Piston Homogeneous Charge Compression Ignition Compressor Concept – Part 1: Performance Estimation and Design Considerations Unique to Small Dimensions", Chemical Engineering Science 57 (2002) 4161-4171.
12. H. T. Aichlmayr, D. B. Kittelson, M. R. Zachariah, "Miniature Free Piston Homogeneous Charge Compression Ignition Compressor Concept – Part 2: Modeling HCCI Combustion in a Small Scales with Detailed Homogeneous Gas Phase Chemical Kinetics", Chemical Engineering Science, 57, 2002, 4173-4186.
13. Onishi S., Jo S. H., Shoda K., Jo P. D., Kato S., "Active Thermo-Atmosphere Combustion, ATAC, a New Combustion Process for Internal Combustion Engine", SAE 790501.
14. Noguchi M., Tanaka Y., Tanaka T., Takeuchi Y., "A Study of Gasoline Engine Combustion by Observation of Intermediate Reactive Products during Combustion", SAE 790840.
15. Najt P., Foster D. E., "Compression-Ignited Homogeneous Charge Combustion", SAE 830264.

16. Thring R. H., "Homogeneous-Charge Compression-Ignition (HCCI) Engines", SAE 892068.
17. Aceves S. M., Flowers D. L., Westbrook C. K., Smith J. R., Pitz W., Dibble R., Christensen M., Johansson B., "A Multi-Zone Model for Prediction of HCCI Combustion and Emissions", SAE 2000-01-0327
18. Sohm V., Kong S.-C., Foster D. E., Morikawa T., Iida M., "A Computational Investigation into the Cool Flame Region in HCCI Combustion", SAE 2004-01-0552.
19. Shibata G., Oyama K., Urushihara T., Nakano T., "The Effect of Fuel Properties on Low and High Temperature Heat Release and Resulting Performance of an HCCI Engine", SAE 2004-01-0553.
20. Shibata G., Oyama K., Urushihara T., Nakano T., "Correlation of Low Temperature Heat Release With Fuel Composition and HCCI Engine Combustion", SAE 2005-01-0138.
21. Haraldsson G., "Closed-Loop Combustion Control of a Multi Cylinder HCCI Engine using Variable Compression Ratio and Fast Thermal Management", Doctoral Thesis, ISBN 91-628-6300-2, Lund Institute of Technology, 2005.
22. Kamimoto T., Bae M., "High Combustion Temperature for the Reduction of Particulate in Diesel Engines", SAE 880423.
23. Asai M., Kurosaki T., Okada K., "Analysis of Fuel Economy Improvement and Exhaust Emission Reduction in a Two-Stroke Engine by Using an Exhaust Valve", SAE 951764.
24. Ishibashi Y., Asai M., "Improving the Exhaust Emissions of Two-Stroke Engines by Applying the Activated Radical Combustion", SAE960742.
25. Christensen M., Hultqvist A., Johansson B., "Demonstrating the Multi Fuel Capability for a Homogeneous Charge Compression ignition Engine with Variable Compression Ratio", SAE 1999-01-3679.
26. Milovanovic N., Blundell D., Gedge S., Turner J., "SI-HCCI-SI Mode Transition at Different Engine Operating Conditions", SAE 2005-01-0156.
27. Christensen M., Hultqvist A., Johansson B., "Demonstrating the Multi Fuel Capability for a Homogeneous Charge Compression ignition Engine with Variable Compression Ratio", SAE 1999-01-3679.
28. Yang J., Culp T., Kenney T., "Development of a Gasoline Engine System Using HCCI Technology – The Concept and the Test Results", SAE 2002-01-2832.
29. Olsson J-O., Tunestål P., Johansson B., "Closed-Loop Control of an HCCI Engine", SAE 2001-01-1031.
30. Hasegawa R., Yanagihara H., "HCCI Combustion in DI Diesel Engine", SAE 2003-01-0745.
31. Turns S. R., " An Introduction to Combustion" p 559-560.
32. Manente V., Tunestål P. and Johansson B., "A Study of a Glow Plug Ignition Engine by Chemiluminescence Images", JSAE 20077042.
33. Manente V., Tunestål P. and Johansson B.," Mini High Speed HCCI Engine Fueled with Ether: Load Range, Emission Characteristics and Optical Analysis", SAE 07APAC-124.
34. Heywood J. B., "Internal Combustion Engine Fundamentals", McGraw-Hill, New York, 1989.
35. Junseok C., Orgun G., Zoran F., Dennis A., Tang-Wei K., Paul N., Rod R.," New Heat Transfer Correlation for an HCCI Engine Derived from Measurements of Instantaneous Surface Heat Flux", SAE 2004-01-2996.
36. Tunestal, P., Self Tuning Cylinder Pressure Based Heat Release Computation,
Proceedings of the IFAC Symposium on Advances in Automotive Control, Monterey Coast, California, August 2007.

37. Hultqvist A. et al. "A Study of the Homogeneous Charge Compression Ignition Combustion Process by Chemiluminescence Imaging", SAE 1999-01-3680.
38. Lyford-Pike E. J., Heywood J. B., "Thermal Boundary Layer Thickness in the Cylinder of a Spark Ignition Engine", International Journal Heat and Mass Transfer, 27, 1984, 1873-1878.
39. Raine R., Thorwarth H., "Performance and Combustion Characteristics of a Glow-Ignition Two-Stroke Engine". Paper obtained from the author.
40. Manente V., Tunestål P., Johansson B.," Mini High Speed HCCI Engine Fueled with Ether: Load Range, Emission Characteristics and Optical Analysis", 07APAC-124, Asia Pacific Conference, 2007.
41. N. Iida, "Combustion Analysis of Methanol-Fueled Active Thermo-Atmosphere Combustion (ATAC) Engine Using a Spectroscopic Observation", SAE 940684.
42. Hildingsson L., "Laser Diagnostics of HCCI and Partially Premixed Combustion" PhD thesis, Division of Combustion Engine, Lund Institute of Technology, Sweden 2006.
43. Christensen M., "HCCI combustion, load range and emission characteristic", Licentiate thesis, Division of Combustion Engine, Lund Institute of Technology, Sweden 1999.

44. Manente V., Tunestål P., Johansson B.," Influence of the Wall Temperature and Combustion Chamber Geometry on the Performance and Emissions of a Mini HCCI Engine Fuelled with Diethyl Ether", to be presented at the SAE World Congress 2008.
45. Hopkinson B., "The Charging of a Two Cycle Internal Combustion Engines", Trans. NE Coast Inst. Engnrs. Shipbuilders, 30, 1914, 433.
46. Benson R.S., Prandham P.J., "A Method for Obtaining a Quantitative Assessment of the Influence of Charge Efficiency on Two Stroke Engine Performance", Int. J. Mech. Sci., 11, 1969, 303
47. Blair G. P., "Design and Simulation of Two-Stroke Engines (R161)", SAE International, 1996.
48. Sammons H., "A Single Cycle Test Apparatus for Studying Loop Scavenging in a Two Stroke Engine", Proc. I. Mech. E., 160, 1949, 233
49. Sanborn D.S., Blair G.P., Kenny R.G., Kingbury A.H., "Experimental Assessment of Scavenging Efficiency of Two Stroke Cycle Engine", SAE Intnl. Off-High Way Vehicle Meeting, Milwaukee, Wisconsin, September, 1980, SAE 800975.
50. Sher E., "Investigating the Gas Exchange Process of a two Stroke Cycle Engine with a Flow Visualization Test Rig", Israel J. Technol. 20, 1982, 127-136.
51. Manente V., Tunestål P., Johansson B.," Influence of the compression ratio on the performance and emissions of a mini HCCI engine fuelled with DME", 07FFL-40, Fuel and lubricant meeting, Chicago, 2007.
52. Roelle M. J., Shaver G. M., Gerdes J. C., "Tackling the Transition: A Multi Mode Combustion Model of SI and HCCI for Mode Transition Control", IMECE 2004-62118, International Mechanical Engineering Conference and Exposition, California 2004.
53. Tallio K. V., Tobis B. J., Selamet A., "The Application of Steady Flow Loss Correlation to Intake Manifold Design", SAE 930608, SAE World Congress, Detroit 2006.
54. Aoyama T., Hattori Y., Mizuta J., "An Experimental Study on Premixed Charge Compression Ignition Gasoline Engine", SAE 960081, SAE World Congress, Detroit 2006.

55. Schwartz F., Spicher U., "Determination of Residual Gas Fraction in IC Engines", SAE 2003-01-3148.
56. Bhave A., Kraft M., Mauss F., "Evaluating HCCI EGR-AFR Operating Range of a HCCI Engine", SAE 2005-01-0161, SAE World Congress, Detroit 2005.
57. Persson H., Hildginsson L., Hultquist A., Johansson B., "Investigation of Boundary Layer Behavior in HCCI Combustion Using Chemiluminescence Imaging", SAE 2005-01-3729.
58. Mohammadi A., Kee S., Ishiyama T., Kakuta T., Matsumoto T., "Implementation of Ethanol-Diesel Blend Fuels in PCCI Combustion", SAE 2005-01-3712.
59. Jarosinski J., Lapucha R., Mazurkiewicz J., "Combustion System of Lean Burning Piston Engine with Catalytic Prechamber", SAE 2001-01-1186, SAE World Congress, Detroit 2001.
60. Lijima A., Watanabe T., Yoshida K., Shoji H., "A Study of HCCI Combustion Using a 2 Stroke Gasoline Engine with High Compression Ratio", SAE 2006-32-0043.
61. Trajicovic S., Miljiosavleic A., Tunestal P., Johansson B., "FPGA Controlled Pneumatic Variable Valve Actuation", SAE 06P-93.
62. Chang J., Guralp O., Filipi Z., Assanis D., "New Heat Transfer Correlation for HCCI Engine Derived from Measurements of Instantaneous Surface Heat Flux", SAE 2004-01-2996, Powertrain and Fluid Systems Conference and Exhibition, California 2004.
63. Cleary D., Farrel P., "Single Surface Flame Quenching Distance Dependence on Wall Temperature, Quenching Geometry and Turbulence", SAE 950162, SAE World Congress, Detroit 1995.
64. Vora K. C., Ghosh B., "Investigating Scavenge Pressure of a Two Stroke Engine with a View to Alleviate Thermal Conditions", SAE 950227, SAE World Congress, Detroit 1995.
65. Smith L. A., Fikensker T., Osborne R. P., "Engine Breathing – Steady State Volumetric Efficiency and its Validity under Transient Engine Operation", SAE 1999-01-0212, SAE World Congress, Detroit 1999.
66. Wang Z., Wang J. X., Shuai S. J., Ma Q. J. "Effects of Spark Ignition and Stratified Charge on Gasoline HCCI Combustion with Direct Injection", SAE 2005-01-0137, SAE World Congress, Detroit 2005.
67. Xie H., Yang L., Qin J., Gao R., Zhu H. G., He B. Q., Zhao H. "The Effects of Spark Ignition on the CAI Combustion Operations", SAE 2005-01-3738.
68. Haraldsson G., Hyvönen J., Tunestål P., Johansson B., "HCCI Closed-Loop Combustion Control Using Fast Thermal Management", SAE 2004-01-0943.
69. Vressner A., Lundin A., Christensen M., Tunestål P. & Johansson B., "Pressure Oscillations during Rapid HCCI Combustion" SAE paper 2003-01-3217 Pittsburgh, USA, 2003.
70. Hyvönen J., Haraldsson G. and Johansson B., "Operating range in a Multi Cylinder HCCI engine using Variable Compression Ratio", JSAE 20030178, SAE 2003-01-1829.
71. Hultqvist, A. "Characterization of the Homogeneous Charge Compression Ignition Combustion Process", Doctoral Thesis, Department of Heat and Power Engineering, Lund Institute of Technology, Lund, Sweden, 2002.
72. Olsson, J.-O., "Performance and Control of the Homogeneous Charge Compression Ignition (HCCI) Engine", Thesis for the degree of Licentiate of Engineering, Lund Institute of Technology, Lund, Sweden, 2002.
73. Christensen, M., Hultqvist, A. and Johansson, B., "The Effect of Combustion Chamber Geometry on HCCI Operation" SAE 2002 Transactions, Journal of Engines SAE Technical Paper 2002-01-0425, 2002.

74. Olsson, J.-O, Tunestål, P., Haraldsson, G. and Johansson, B. "A Turbo Charged Dual Fuel HCCI Engine", SAE Technical Paper 2001-01-1896, 2001.
75. Hultqvist, A., Christensen, M. and Johansson, B., "The Application of Ceramic and Catalytic Coatings to Reduce the Unburned Hydrocarbon Emissions from a Homogeneous Charge Compression Ignition Engine", SAE Technical Paper 2000-01-1833, 2000.

16. Summary of papers

Paper 1

Influence of inlet temperature and hot residual gases on the performances of a mini high speed glow plug engine

By Vittorio Manente, Per Tunestål, Bengt Johansson

06SETC-55, presented by the author at the Small Engine Technology Conference, San Antonio, Texas, 2006.

The aim of the paper was to characterize the combustion process of a small glow plug engine. The manuscript is divided into two sections. The first part describes measurements carried out between 14500 and 17500 [rpm] and was aimed at understanding the performance and emission levels of the engine. The second section deals with the influence of preheated inlet air and amount of retained burned gases. The research resulted in a sloppy IMEP trace, incredibly high emission levels and very low values of indicated efficiency (5.5 – 8.5 %). Heating the inlet mixture and increasing the amount of residual gases enabled a reduction of the emissions and at the same time a decrease in the output power. No improvements of the indicated efficiency were noted, however, this parameter was lowered as a result of an increase in the pumping work due to the throttling of the exhaust.

Paper 2

A Study of a Glow Plug Ignition Engine by Chemiluminescence Images

By Vittorio Manente, Per Tunestål, Bengt Johansson

JSAE 20077042, presented by the author at the Fuel and Lubricant Meeting, Kyoto, Japan, 2007.

The paper reports on an optical study of the combustion process of a model airplane glow plug engine. Two sets of measurements were performed at 9600 and 13400 [rpm], and for each operative point the total chemiluminescence light was acquired as well as that of formaldehyde and hydroxyl radicals. The study demonstrated that a glow plug engine is a compression ignition engine and that the function of the glow plug was to supply the remaining energy for triggering the reactions. The combustion process was characterized by propagating autoignition reactions rather than a flame front. The radicals were homogenously spread all over the combustion volume as in HCCI combustion and moreover, the sequence formaldehyde – hydroxyl was observed. The analysis of the boundary layer highlighted that, when the piston was at the TDC, its percentage in the radial direction was 13% whereas it was 100% in the axial one.

Paper 3

Mini High Speed HCCI Engine Fueled with Ether: Load Range, Emission Characteristics and Optical Analysis

By Vittorio Manente, Per Tunestål, Bengt Johansson

07APAC-124, presented by the author at Asia – Pacific Conference, Hollywood, California, 2007.

The intent of this investigation was to characterize the HCCI combustion process in a small volume at a high engine speed. The paper is divided into three parts: performance and emissions analysis, optical diagnostic, and a comparison between the optical and metal engine. The first section showed that IMEP steadily increased with increasing engine speed because of the improvement of the thermal management. As for the glow plug engine, the emissions in a small HCCI engine were very high and the indicated efficiency was rather low (between 2 and 5 %). This was basically due to quenching phenomena and the volume of the boundary layer. Optical diagnostic showed that the fuel/air distribution was rather uneven, especially at low speed, thus resulting in soot formation, high emissions of unburned hydrocarbons and a low fuel conversion efficiency. The increase in turbulence level demonstrated the possibility of improving the degree of homogeneity with positive consequences on the performance. The comparison between the optical and metal engines underlined the extent of sensitivity of HCCI combustion to the boundary conditions. The behavior of the two engines was totally different in terms of combustion phasing and performances, and the gap between them increased with engine speed.

Paper 4

Influence of the compression ratio on the performance and emissions of a mini HCCI engine fueled with diethyl ether

By Vittorio Manente, Per Tunestål, Bengt Johansson

07FFL-40, accepted for publication at the Fuel and Lubricant Meeting, Chicago, Illinois, 2007.

By using 5 different spacers, the squish distance and hence the compression ratio, was changed and its influence on the performance of a small HCCI engine was analyzed. The research showed that the performances were not directly proportional to the compression ratio as expected from the equation $\eta = 1 - \dfrac{1}{r_c^{\gamma-1}}$. As a result of decreasing the squish distance down to 0.25 [mm], the quenching phenomena started to play a fundamental role and consequently IMEP, efficiencies and emissions were improved to an optimum point for a decreasing compression ratio.

After this optimum, they started to decrease as predicted from the equation previously mentioned.

This paper played an important role in the life of the VIMPA project. The knowledge of the optimum compression ratio and the fact that quenching did not occur for a squish distance of 0.25 [mm] when DEE was used as fuel was valuable information for the design of the VIMPA engine.

Paper 5

Influence of the Wall Temperature and Combustion Chamber Geometry on the Performance and Emissions of a Mini HCCI Engine Fueled with Diethyl Ether

By Vittorio Manente, Per Tunestål, Bengt Johansson

The abstract has been submitted to the SAE World Congress, Detroit, Massachusetts, 2008.

HCCI combustion was achieved in a small volume at a high engine speed. The objective of this research was to understand the role of the wall temperature and the combustion chamber geometry of the combustion features. The study demonstrated that increasing the temperature of the combustion chamber walls, rendered it possible to increase the temperature of the crankcase as well as that of the inlet mixture. This was due to the small dimensions of the engine. The increase in wall temperature led to a better conversion efficiency, but on the other hand IMEP was lowered since less of the mixture was inserted. The research suggested that the engine could be optimized by using a cold crankcase and hot combustion chamber walls. The use of a pancake combustion chamber was much preferred to a bowl geometry for a such small volume, as quenching on the side of the bowl was significant.

Paper 6

A New Method for a Fast Prediction of the Trapping Efficiency and Residual Gas Fraction in a Small High Speed HCCI Engine Fueled with Diethyl Ether

By Vittorio Manente, Per Tunestål, Bengt Johansson

The abstract will be sent to the Small Engine Technology Conference, 2008.

The paper describes an innovative method for calculating the retained burned gases and the trapping efficiency in a 2-stroke engine. This method consists in a "switch" model, in which the perfect mixing and perfect displacement algorithms have been implemented and the level of turbulence in the combustion chamber is used as a border between them. The validation was carried out by measuring the trapping efficiency (on a mini HCCI engine) and comparing this value with the one predicted by the model. The discrepancy between these values was found to lie between 2.8 and 0.06%.

17. Acronyms and abbreviations

%RES   Residual gas fraction
10%HR 10% of heat release, start of the combustion
50%HR 50% of heat release, combustion phase
90%HR 90% of heat release, end of the combustion
A/D   Analogic/Digital
aBDC   After Bottom Dead Center
ATAC   Active Thermo Atmosphere Combustion
ATDC   After Top Dead Center
aTDC   After Top Dead Center
B   Bore
BDC   Bottom Dead Center
CAI   Compression Auto Ignition
CI   Compression Ignition
CO   Carbon monoxide
CO_2 Carbon dioxide
COV   Coefficient Of Variation
c_p Specific heat at constant volume
c_v Specific heat at constant pressure
DC   Direct current
DEE   Diethyl ether
DME   Dimethyl ether
d_q Quenching distance
EGR   Exhaust Gas Recirculation
EPC   Exhaust Ports Close
EPO   Exhaust Ports Open
EVC   Exhaust Valve Closing
f   Flame
GACI   Glow plug Assisted Compression Ignition
GP   Glow Plug
GPE   Glow Plug Engine
H2   Hydrogen
HCCI   Homogeneous Charge Compression Ignition
HTR   High Temperature Reactions
I   Input
ICE   Internal combustion engine
IMEP   Indicated Mean Effective Pressure
IPC   Intake Ports Close
IPO   Intake Ports Open
IVC   Intake Valve Closing
IVO   Intake Valve Opening
k   Thermal conductivity
L   Diameter of the largest eddy
LTR   Low Temperature Reactions
m   Cylinder mass
m_{BG} Mass of burned gases
MEMS Micro Electro Mechanical Systems

m_{FM}	Mass of fresh mixture
m_{FM_out}	Mass of fresh mixture flushed from the cylinder
m_{FT}	Mass of fresh mixture trapped in the cylinder
m_{in}	Intake mass flow
m_{out}	Exhaust mass flow
m_{res}	Mass of residual gases
N	Engine rotational speed
NO	Nitrogen monoxide
NO_2	Nitrogen dioxide
NO_x	Nitrogen dioxide and monoxide
Nu	Nusselt number
NVO	Negative Valve Overlap
O	Output
O_2	Oxygen
P	Pressure
Pe	Peclet number
Pex	Exhaust pressure
PM	Particulate matter
ppm	Parts Per Million
Pr	Prandtl number
PRF	Primary Reference Fuels
Q	Heat release
$Q_{Crevice}$	Crevice mass flow
Q_{HT}	Heat transfer
R	Universal gas constant
Re	Reynolds number
RPM	Revolutions Per Minute
SF	Safety Factor
SI	Spark Ignition
S_L	Laminar flame speed
SO_2	Sulfur dioxide
SOI	Start Of Injection
SO_x	Sulfur dioxide and monoxide
Sq	Squish distance
St	Stroke
T	Temperature
t	Time scale of the largest eddy
T_{AVG_BD}	Average temperature during the blow-down
T_{AVG_EX}	Average temperature during the exhaust
T_{AVG_IN}	Average temperature of the crankcase during the intake
TDC	Top Dead Center
Tin	Inlet temperature
u	Unburned
U	Internal energy
UHC	Unburned Hydrocarbon
V	Volume
v	Velocity of the largest eddy

V_c Clearance volume

V_d Displacement volume

V_{max} Maximum volume

V_{min} Minimum volume

VVT   Variable Valves Timing

W   Work

Greek Symbols

ϕ Equivalence ratio

γ Ratio of Specific Heats

η_{trap} Trapping Efficiency

Θ CAD scale of the largest eddy

θ Crank Angle

Appendix A1: Glow plug combustion features

Certain combustion features of glow plug combustion are shown.
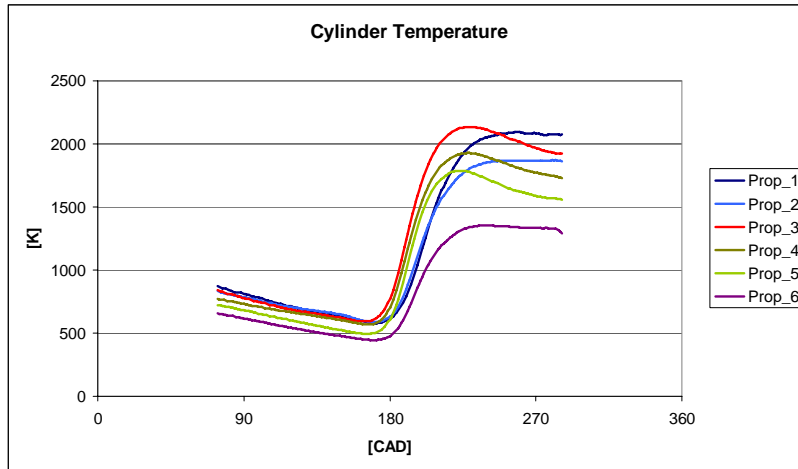
Figure A1-1: The in-cylinder combustion temperature computed between 14500 and 17500 [rpm]. Propeller 1 is the fastest and propeller 6 the slowest.

Figure A1-2: The indicated power measured between 14500 and 17500 [rpm].
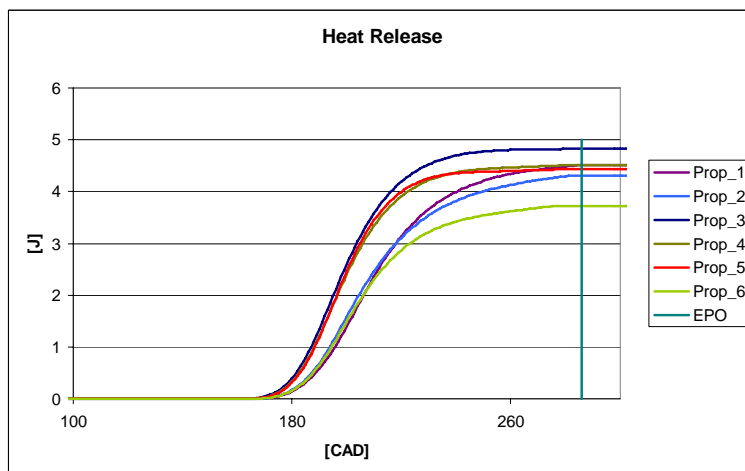
Figure A1-3: The cumulated heat release computed between 14500 and 17500 [rpm]. Propeller 1 is the fastest and propeller 6 the slowest.
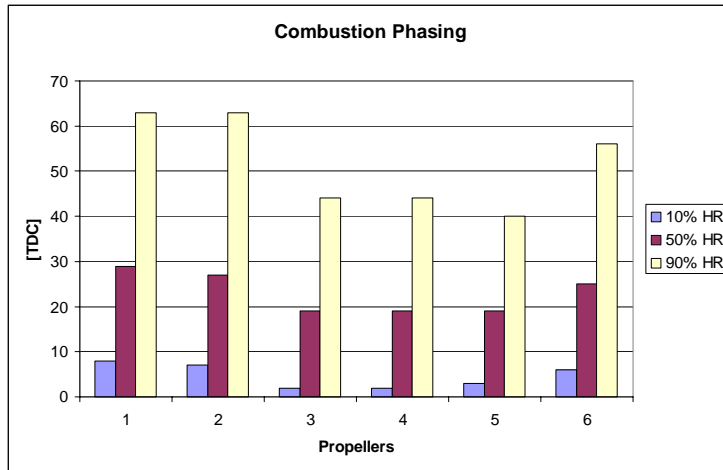
Figure A1-4: The combustion phasing computed between 14500 and 17500 [rpm]. Propeller 1 is the fastest and propeller 6 the slowest.
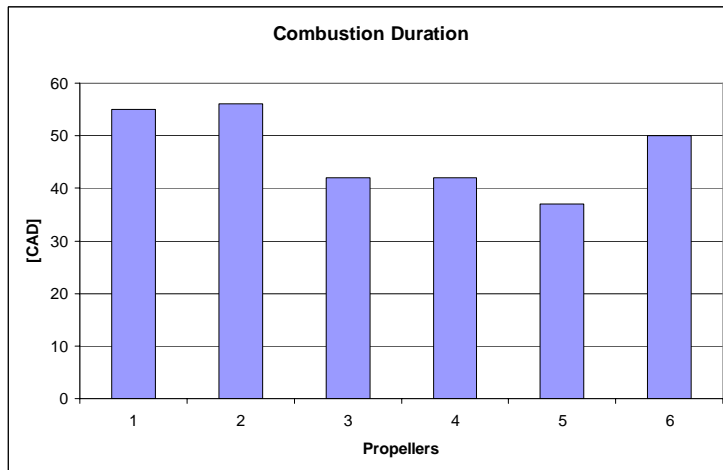
Figure A1-5: The combustion duration, 90%HR – 10%HR, in the CAD domain computed between 14500 and 17500 [rpm]. Propeller 1 is the fastest and propeller 6 the slowest.
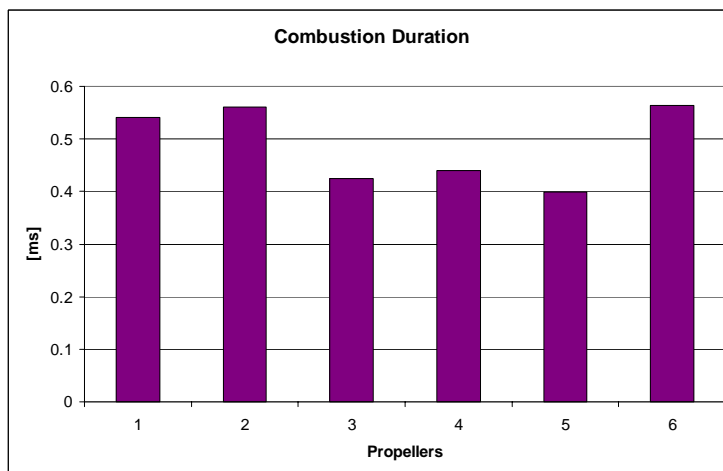
Figure A1-6: The combustion duration, 90%HR – 10%HR, in the time domain computed between 14500 and 17500 [rpm]. Propeller 1 is the fastest and propeller 6 the slowest.
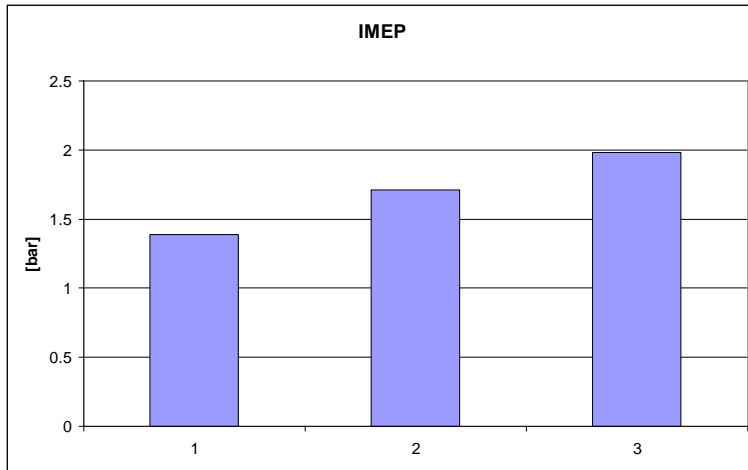
Figure A1-7: The IMEP variation when heating the inlet mixture and increasing the amount of retained burned gases. 1 ➔ Tin = 431 [K] & Pex = 1.12 [bar], 2 ➔ Tin = 298 [K] & Pex = 1.15 [bar], 3 ➔Tin = 298 [K] & Pex = 1.02 [bar].
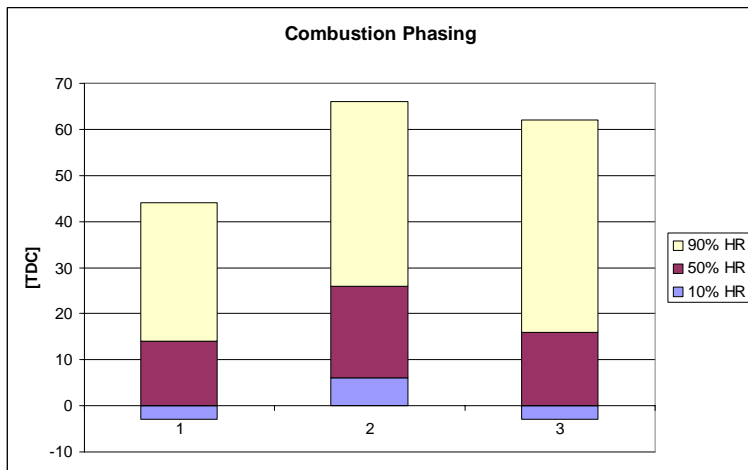
Figure A1-8: The combustion phasing variation when heating the inlet mixture and increasing the amount of retained burned gases. 1 ➔ Tin = 431 [K] & Pex = 1.12 [bar], 2 ➔ Tin = 298 [K] & Pex = 1.15 [bar], 3 ➔Tin = 298 [K] & Pex = 1.02 [bar].

115
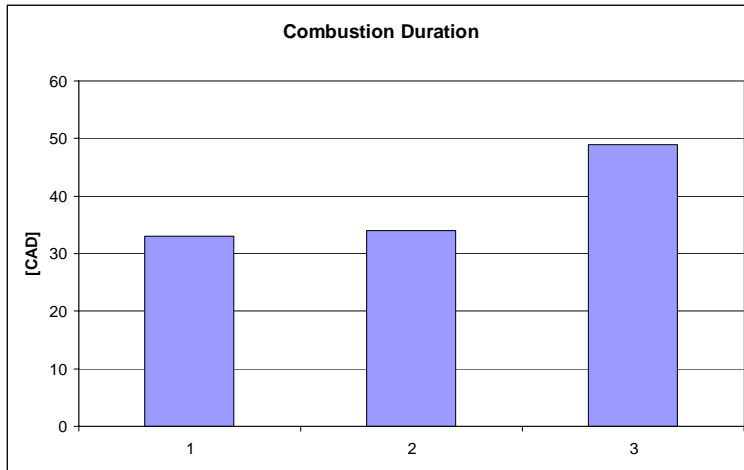
Figure A1-9: The variation in combustion duration, 90%HR – 10%HR, when heating the inlet mixture and increasing the amount of retained burned gases. 1 ➔ Tin = 431 [K] & Pex = 1.12 [bar], 2 ➔ Tin = 298 [K] & Pex = 1.15 [bar], 3 ➔Tin = 298 [K] & Pex = 1.02 [bar].

Table A1-1: A summary of the average performance of the glow plug optical engine at 9600 [rpm].

Pex	1.0239	[bar]
Tex	352	[K]
X10	164	[ABDC]
X50	190	[ABDC]
CD	74	[CAD]
Res	16	[%]
IMEP	2.23	[bar]
Power	141	[W]
N	9592	[rpm]

Table A1-2: A summary of the average performance of the glow plug optical engine at 13400 [rpm].

Pex	1.0342	[bar]
Tex	371	[K]
X10	177	[ABDC]
X50	195	[ABDC]
CD	46	[CAD]
Res	30	[%]
IMEP	3.54	[bar]
Power	351	[W]
N	13383	[rpm]

Appendix A2: HCCI combustion features

Certain combustion features of HCCI combustion are shown.

Combustion Temperature
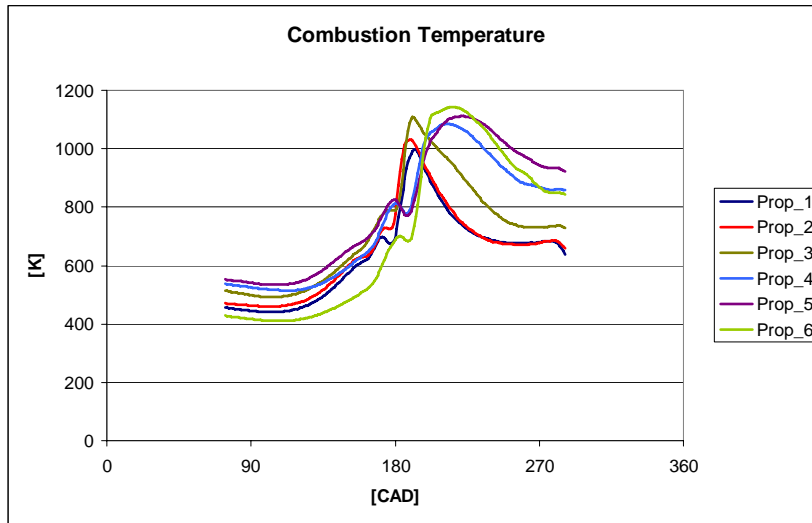
Figure A2-1: The in-cylinder combustion temperature computed between 7500 and 17500 [rpm]. Propeller 1 is the slowest and propeller 6 the fastest.
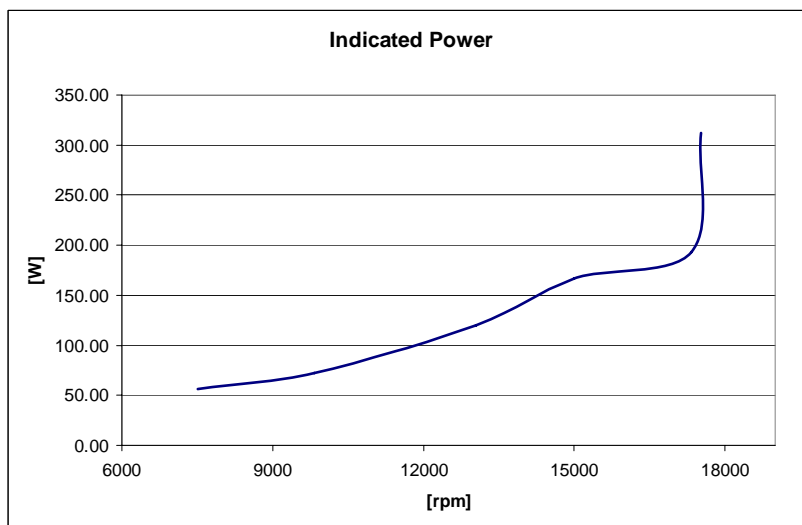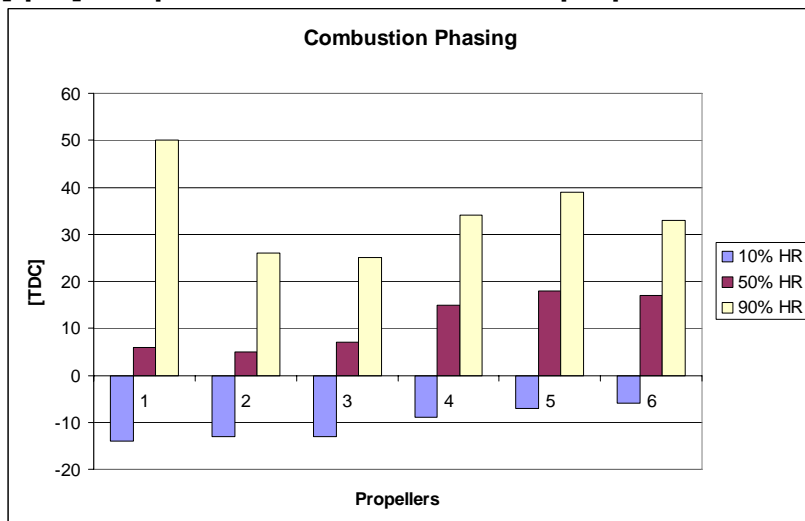
Indicated Power

**Figure A2-2: The indicated power computed between 7500 and 17500 [rpm].**
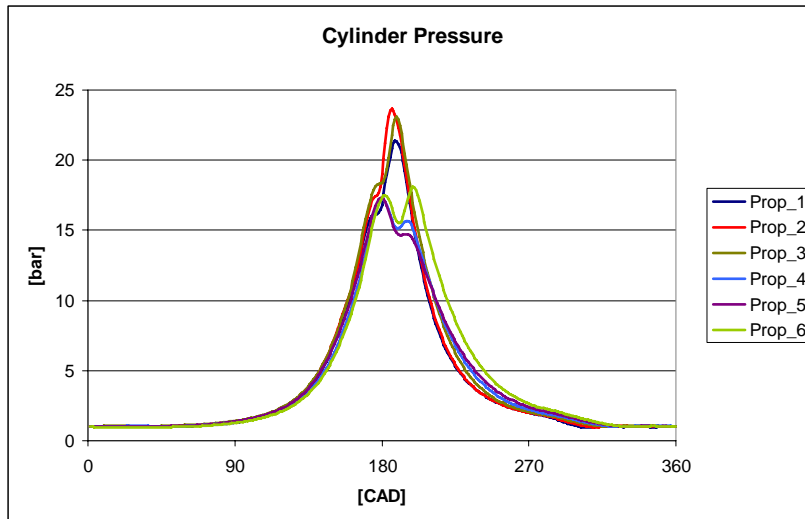
Figure A2-3: In-cylinder pressure traces acquired between 7500 and 17500 [rpm]. Propeller 1 is the slowest and propeller 6 the fastest.
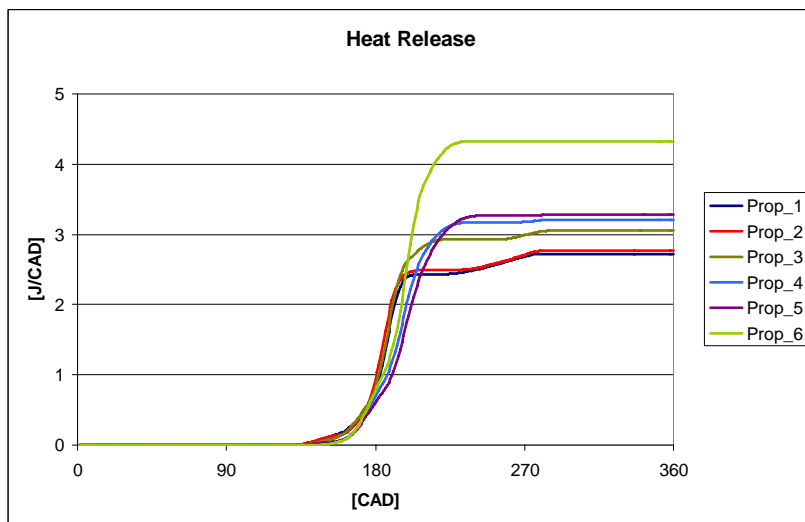
Figure A2-4: The cumulated heat release computed between 7500 and 17500 [rpm]. Propeller 1 is the slowest and propeller 6 the fastest.
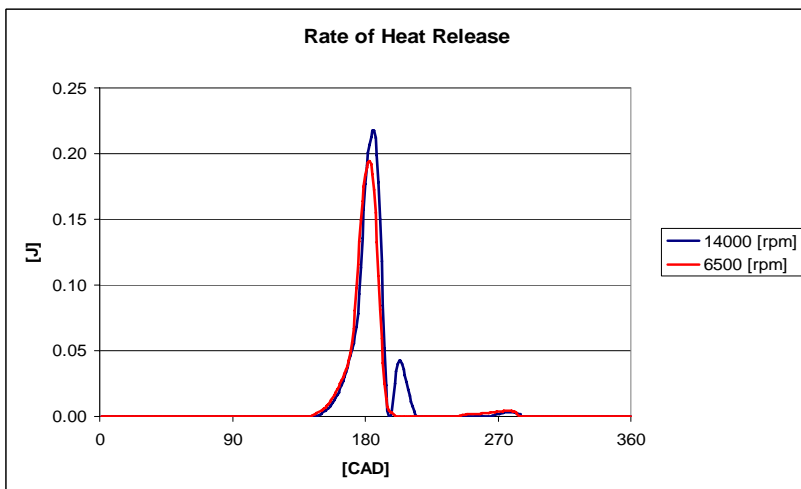

Figure A2-5: The combustion phasing computed between 7500 and 17500 [rpm]. Propeller 1 is the slowest and propeller 6 the fastest.
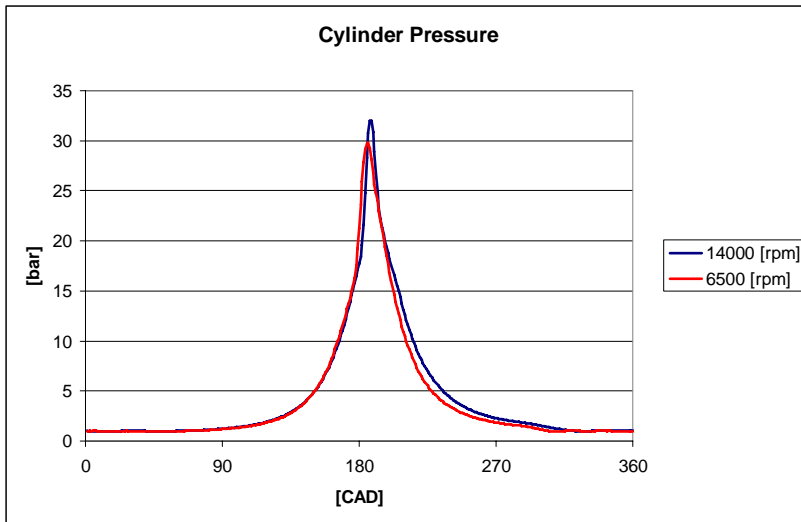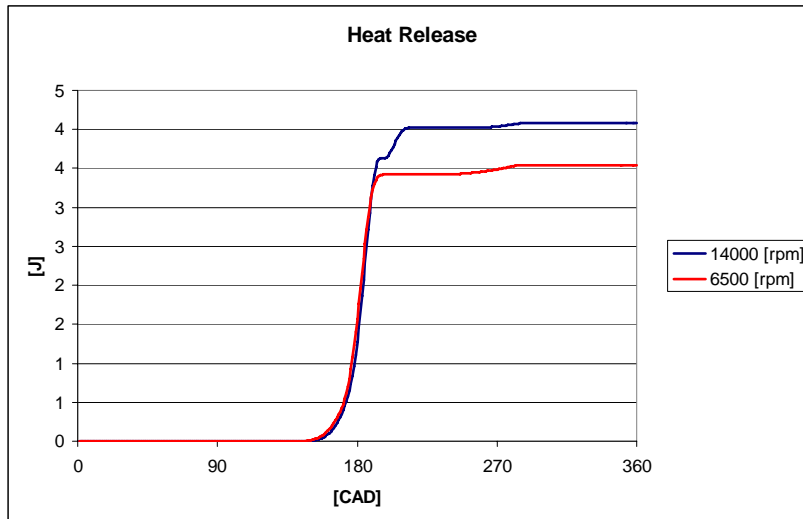
Figure A2-6: Cylinder pressure traces acquired during the optical experiments at 14000 and 6500 [rpm].
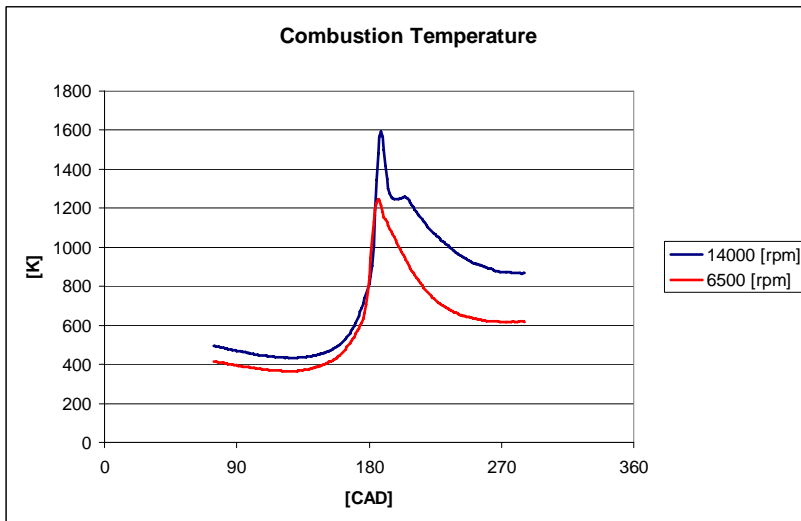
Figure A2-7: In-cylinder temperature traces computed for the optical engine at 14000 and 6500 [rpm].

**Figure A2-8: Rate of heat release traces computed for the optical engine at 14000 and 6500 [rpm].**

Figure A2-9: Cumulated heat release traces computed for the optical engine at 14000 and 6500 [rpm].

Table A2-1: A summary of the performances of the optical engine at 6500 and 13400 [rpm].

	Prop_4	Prop_1
Pex [bar]	1.0169	1.011
Tex [K]	344	312
N [rpm]	14069	6646
x10 [ABDC]	172	169
x50 [ABDC]	184	182
CD [CAD]	29	21
Res [%]	50.83	38.91
IMEP [bar]	2.48	1.78
Power [W]	240.96	81.82

Appendix A3: VIMPA CAD
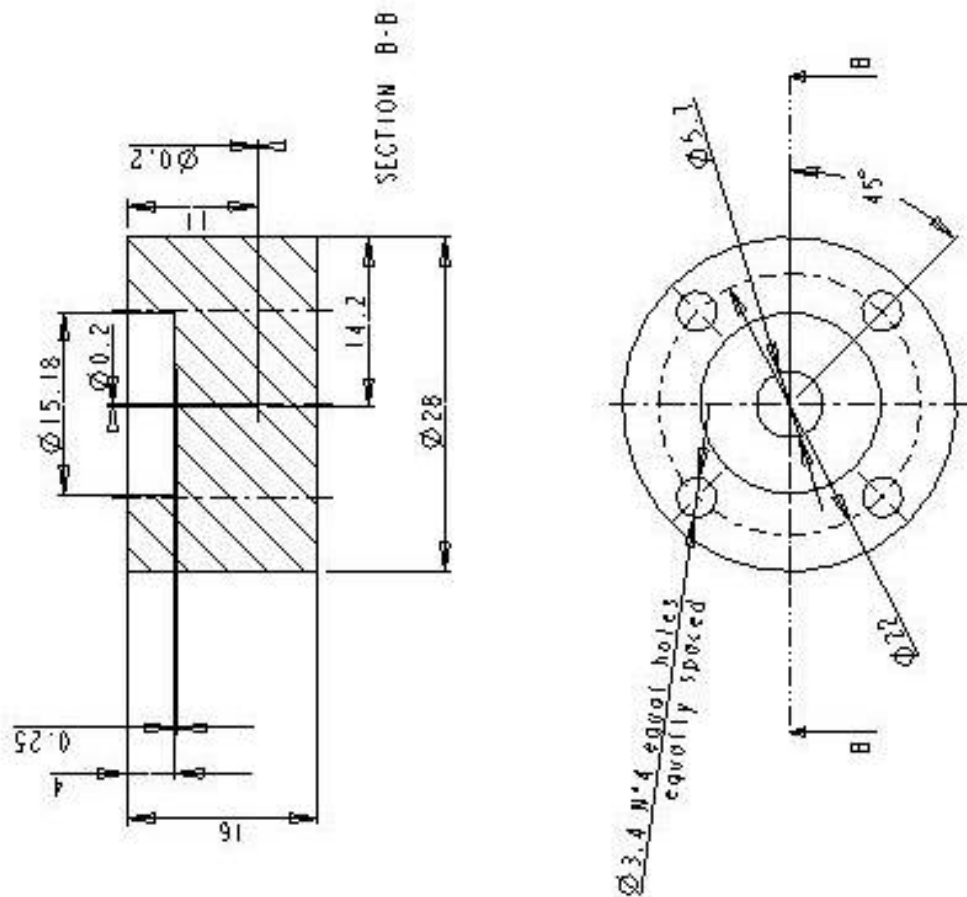
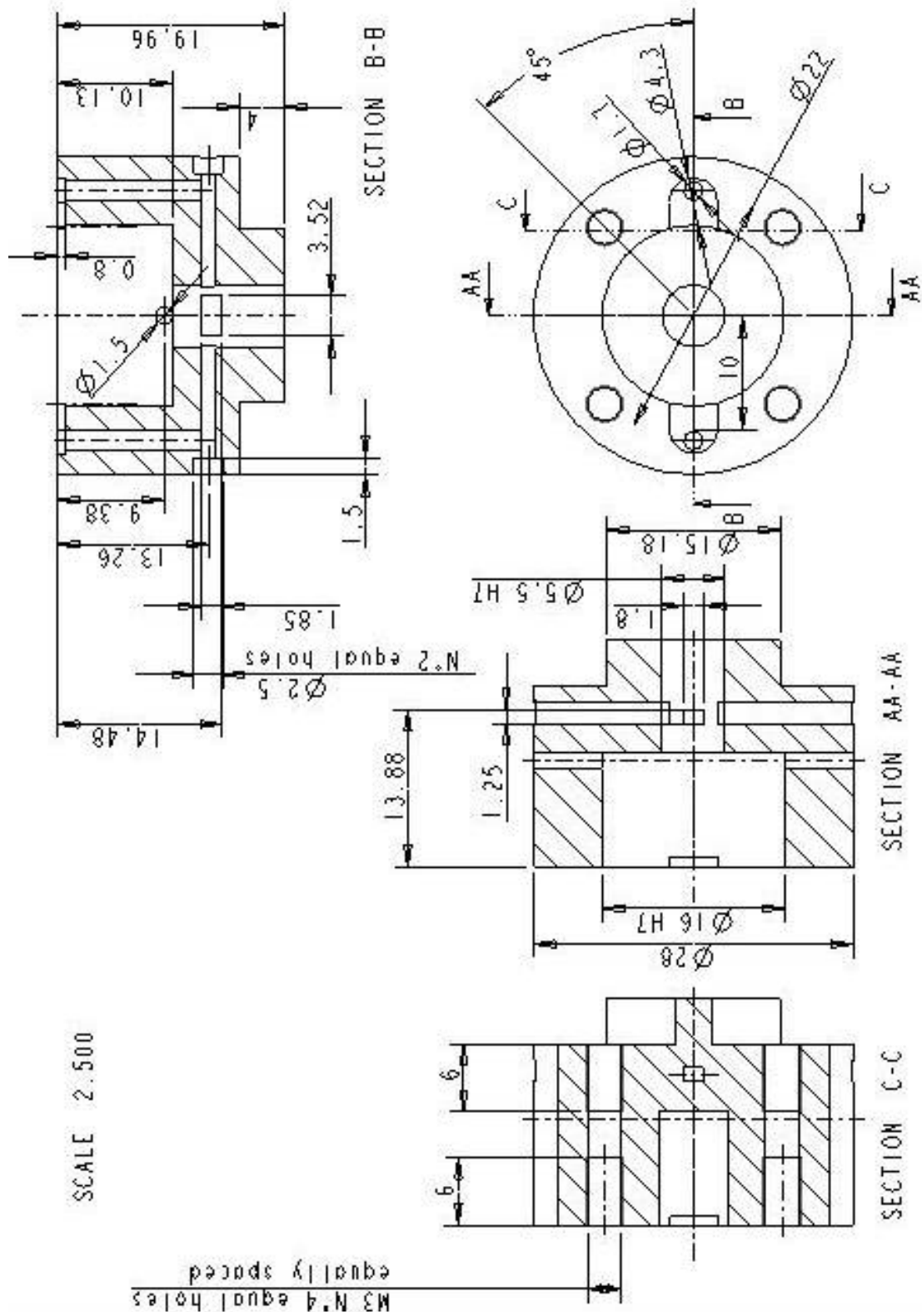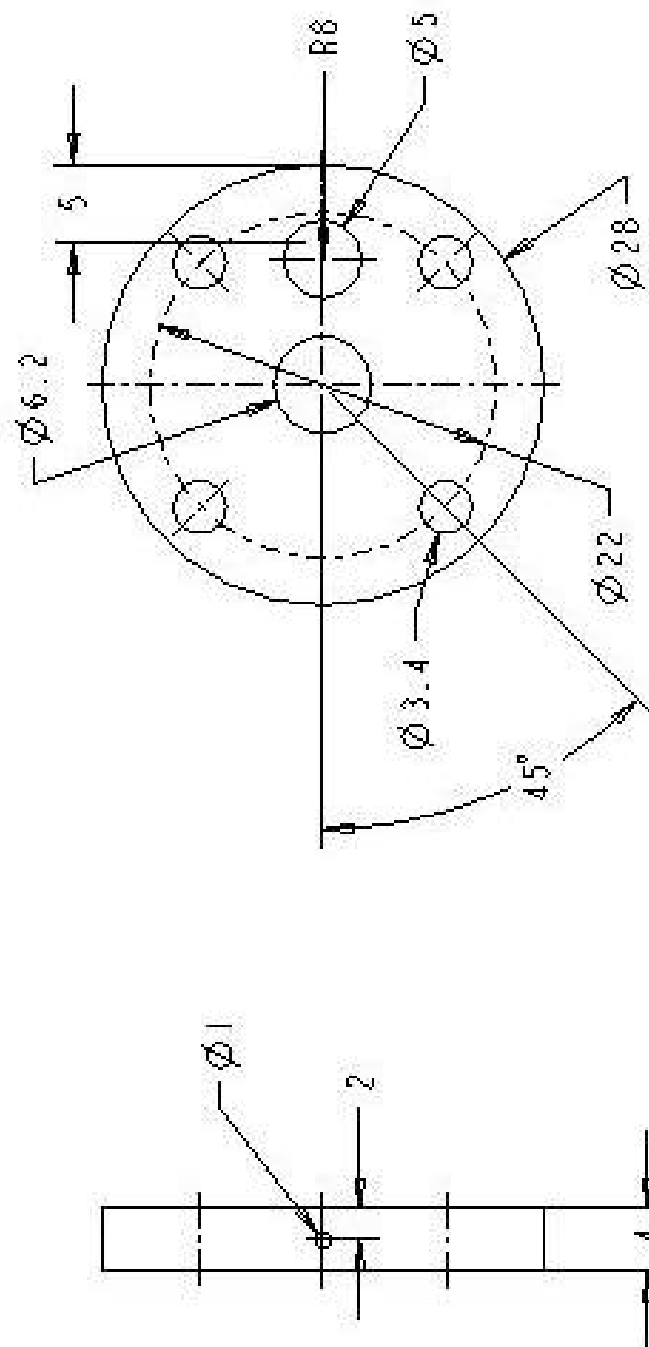**Figure A3-1: The VIMPA base.**

Figure A3-2: The VIMPA crankcase and combustion chamber.

SCALE 2.500

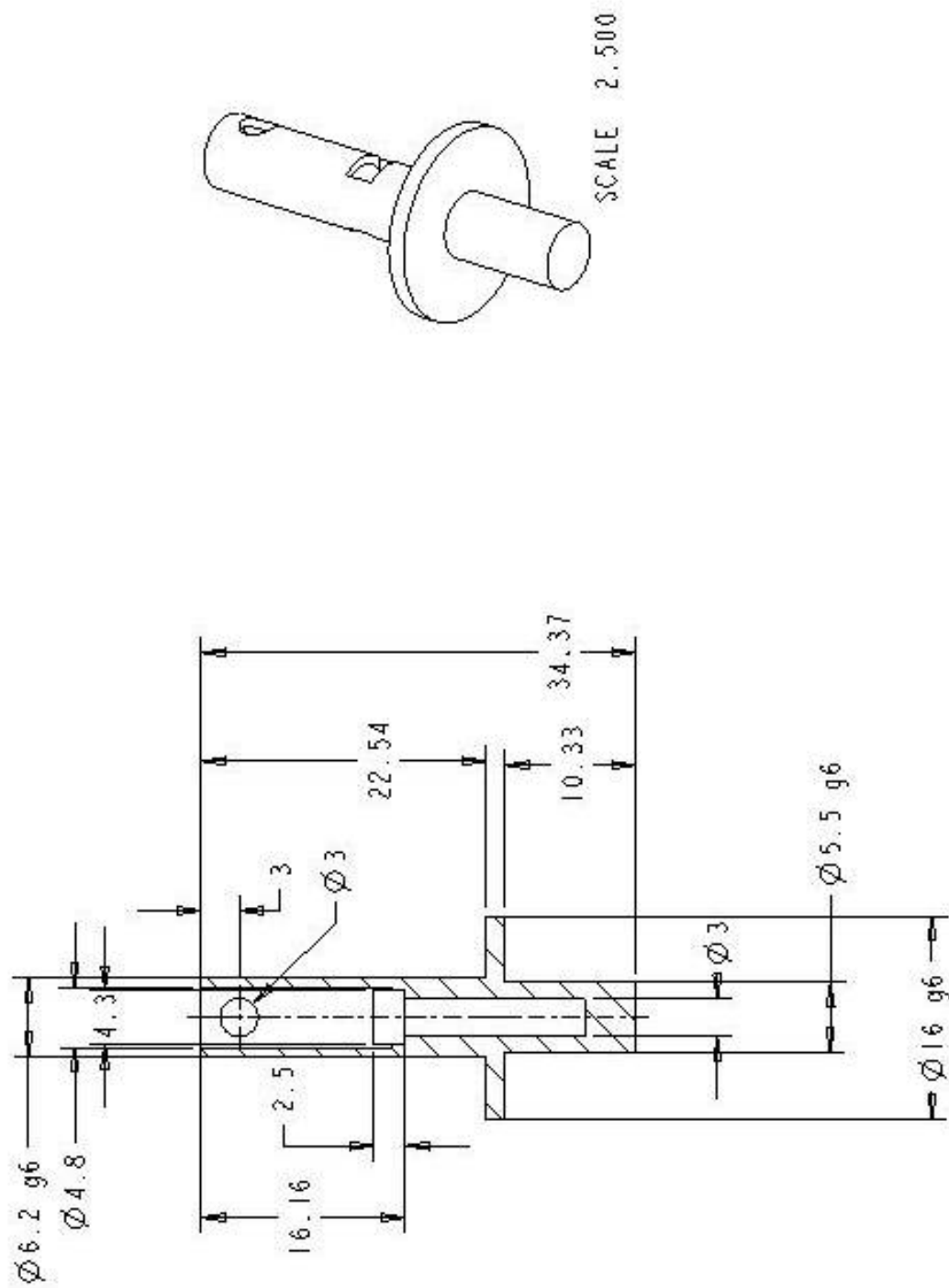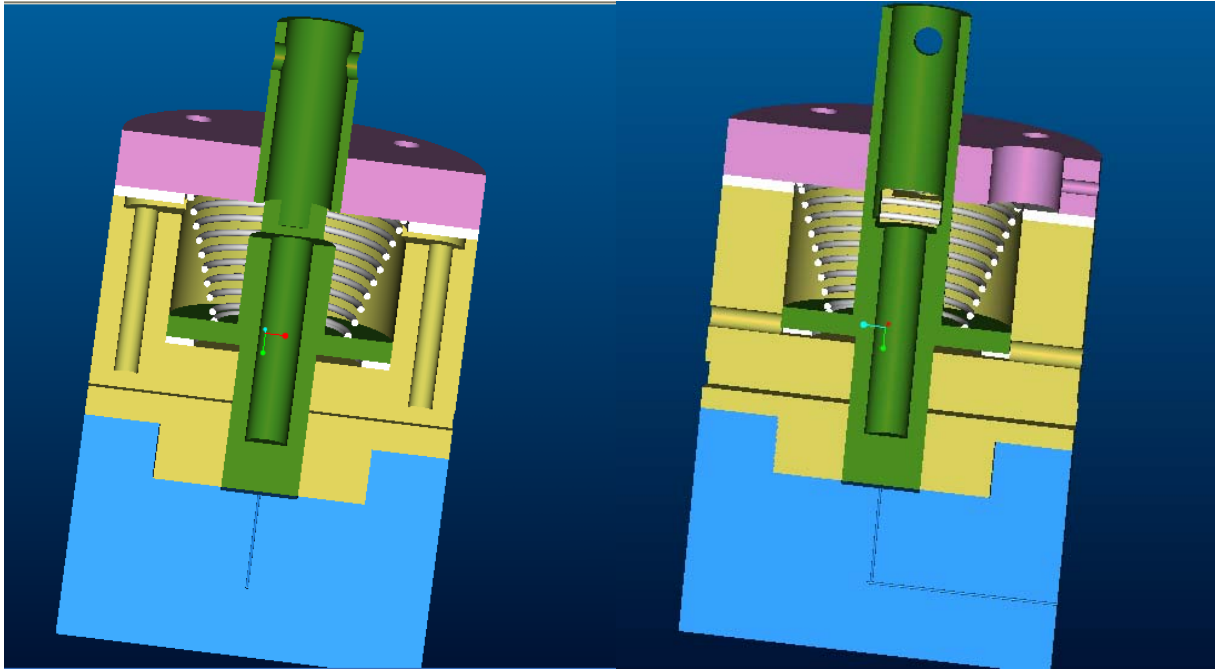**Figure A3-3: The cap for sealing the crankcase.**

Figure A3-4: The VIMPA free piston.

Figure A3-5: The VIMPA engine assembly.